Controlled spontaneous emission in erbium-doped microphotonic materials

Controlled spontaneous emission in erbium-doped microphotonic materials
Jeroen Kalkman

ISBN 90-393-0295-2

A digital version of this thesis can be downloaded from http://www.amolf.nl

Controlled spontaneous emission in erbium-doped microphotonic materials

Gecontroleerde spontane emissie in met erbium gedoteerde microfotonische materialen.

(met een samenvatting in het Nederlands)

Proefschrift

ter verkrijging van de graad van doctor aan de Universiteit Utrecht
op gezag van de Rector Magnificus, Prof. Dr. W. H. Gispen,
ingevolge het besluit van het College voor Promoties
in het openbaar te verdedigen
op woensdag 9 maart 2005 des middags te 14.30 uur

door

Jeroen Kalkman

geboren op 26 mei 1975 te Velsen

Promotor: Prof. Dr. A. Polman
Faculteit der Natuur- en Sterrenkunde, Universiteit Utrecht
FOM Instituut voor Atoom- en Molecuulfysica, Amsterdam

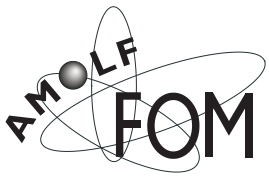

The work described in this thesis was performed at the FOM Institute for Atomic and Molecular Physics, Kruislaan 407, 1098 SJ Amsterdam, The Netherlands. It is part of the research program of the 'Stichting voor Fundamenteel Onderzoek der Materie' (FOM), and was made possible by financial support from the 'Nederlandse Organisatie voor Wetenschappelijk Onderzoek' (NWO) and NanoNed, a technology program of the Dutch Ministry of Economic affairs.

Contents

Chapter 1

General introduction

We cannot imagine a world without artificial light. Not only did it make man independent of the day/night rhythm imposed on us by nature, but applications in telecommunication, data storage, geodesy, medicine, and displays have influenced our lives on an unimaginable scale. The development of new applications has been largely driven by the ability to control the flow and emission of light in photonic structures. Current day telecommunication for example, is based on control of light with lasers and optical glass fibers. Erbium-doped fiber amplifiers that amplify light at 1.5 μm have enabled long-distance glass-fiber telecommunication that is key to the rapid growth of the internet.

Today we are on the brink of a new revolution in the use of light. Scaling down the dimensions of photonic structures provides us with new opportunities to control the emission and guiding of light. Si-based electronic integrated circuits for example, may benefit from bringing photons on a chip. Due to the high optical carrier frequency, lack of cross talk, low power dissipation and potential for wavelength division multiplexing, problems caused by downscaling the size of electrical circuits on a Si chip may be overcome.[1] The introduction of microscale and nanoscale photonics on a Si-integrated circuit can also lead to a natural integration of fiber-based optical telecommunication and electronic processing on a chip. In today's society with its increasing demand for larger bandwidth, this would allow for optical data processing and a corresponding increase in data bandwidth and computational power. Although still in its infancy, the advent of quantum computing and its integration with microelectronics may also require nanoscale photonic circuits.[2] Quantum computation promises great increases in computational performance for complex calculations. Microphotonics also offers new possibilities for enhancing the out-coupling efficiency of light emitting diodes and increasing the conversion efficiency in solar cells. Finally, scaling down the dimensions of photonic structures may lead to interesting new physical phenomena as we enter new regimes of strong electromagnetic fields that enhances non-linear processes. It is the precise control of light in novel microstructured photonic materials that is necessary to open up these new possibilities.

1.1 Modified spontaneous emission

The emissive properties of atoms can be manipulated by controlling their photonic environment on a length scale comparable to the emission wavelength. From first order time-dependent perturbation theory, Fermi's golden rule can be derived.[3] Considering the interaction of the atom with the electromagnetic field as a perturbation and assuming that the dipole interaction is dominant (taking the electric field parallel to the dipole moment), the spontaneous emission rate can be calculated using quantization of both the field and the atom. The result is given by [4]

$$W_{i\to f} = \frac{\pi\omega_{i,f}}{\hbar\epsilon(\mathbf{r})}|\langle f|\hat{\mu}|i\rangle|^2\rho(\omega_{i,f},\mathbf{r}) \qquad , \tag{1.1}$$

with $\omega_{i,f}$ the transition frequency corresponding to the energy gap between the initial and final state, $\epsilon(\mathbf{r})$ the position dependent dielectric constant, $\rho(\omega_{i,f},\mathbf{r})$ the frequency and position dependent local photonic density of states, $|f\rangle$ and $|i\rangle$ the final and initial state of the atom, and $\hat{\mu}$ the dipole operator. Equation 1.1 states that the radiative decay rate of an emitter is the product of two terms. The first term describes the dipole's intrinsic decay probability (determined by the electronic wavefunctions $|f\rangle$ and $|i\rangle$ of the atom). The second term $\rho(\omega_{i,f},\mathbf{r})$, the local photonic density of states (DOS), describes the number of states per unit volume that the atom can decay into.

For optical emitters embedded in a solid the term $|\langle f|\hat{\mu}|i\rangle|^2$ in Eq. 1.1 depends on the electronic environment with a length scale on the order of the electron wavefunctions of the atom. While this term cannot be arbitrarily influenced, large differences can be observed for the same dipole embedded in different hosts. The DOS term $\rho(\omega_{i,f},\mathbf{r})$, depends on the photonic microstructure around the atom with a length scale given by the wavelength of the emitted light. It can be modified by controlling the microstructure around the atom leading to large effects on the spontaneous emission as we will show further on.

The simplest photonic microstructure is a one-dimensional dielectric interface placed close to an optical emitter. Figure 1.1 shows the decay rate for a randomly oriented dipole in SiO_2 and air emitting at a wavelength of 1535 nm as a function of distance from an air/SiO_2 interface. The decay rate is normalized to the decay rate in air. The decay rate shows oscillations as a function of distance to the interface due to interference of emitted waves with the oscillating dipole, leading to an increase or decrease of the decay rate depending on the distance from the interface. Initially, calculations such as in Fig. 1.1 were made using a rigorous plane-wave expansion method.[4] Later, a Green's function method was introduced that is mathematically somewhat more elegant and is also faster to evaluate.[5] A disadvantage of these methods is that they cannot take absorption into account. Here, we use a classical dipole oscillator model that is fast and does not suffer from this disadvantage.[6] If a point dipole is embedded in a non-absorbing dielectric the general relation for the power radiated from the dipole can be derived from Poynting's theorem,

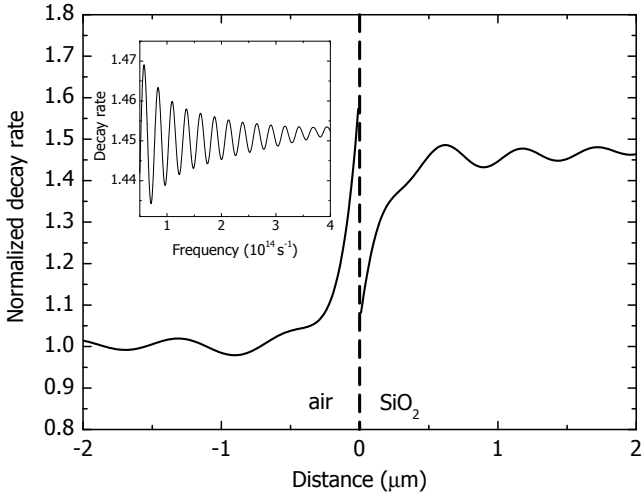

Figure 1.1: Normalized decay rate for a randomly oriented dipole emitting at a wavelength of 1535 nm as a function of distance from a SiO_2/air interface, calculated with the classical dipole oscillator model. Modulation of the spontaneous emission rate occurs due to interference of emitted waves with the oscillating dipole. Inset shows the relative decay rate variation as a function of emission frequency for a dipole in SiO_2 at 4 μm from the interface.

and is given by the surface integral over the Poynting vector:

$$\frac{1}{2} Re \int_S (\mathbf{E} \times \mathbf{B}^*)\, dS = \frac{\omega}{2} Im \left[\mathbf{p} \cdot \mathbf{E}(\mathbf{r_0})\right] \qquad , \tag{1.2}$$

with $\mathbf{E}$ and $\mathbf{B}$ the electric and magnetic fields respectively, and $\mathbf{p}$ the dipole moment. Equation 1.2 shows that the radiated power is proportional to the inner-product of the electric field at the position of the dipole and the dipole moment. By calculating all reflected and transmitted electric fields originating from the dipole, the total electric field at the position of the dipole ($\mathbf{E}(\mathbf{r}_0)$) can be obtained. The decay rate is then determined by calculating the right side of Eq. 1.2 and dividing by $\hbar\omega$. The inset of Fig. 1.1 shows the relative decay rate modulation due to variations in DOS of a randomly oriented dipole in SiO_2 at a distance of 4 μm from the air/SiO_2 interface plotted as a function of emission frequency in a range corresponding to free space wavelengths of 500 nm to 10 μm. Again, due to interference, the decay rate is modulated. However, the relative change in decay rate is very small. This is a consequence of the fact that only in a small emission solid angle reflected waves have an effect on the dipole and that for these waves only single interference effects take place. Clearly, when materials are used that have a high refractive index contrast, waves reflected from the interfaces will have a large amplitude, resulting in larger variations in the decay rate.

Metal interfaces placed close to an optical emitter provide a large refractive index contrast, but also introduce additional decay mechanisms. At small distances to a metal interface the optical emitter decays predominantly by direct coupling to electronic states in the metal. At somewhat larger distances a large fraction of the decay goes into the excitation of surface plasmons (SPs). Surface plasmons are electromagnetic waves bound at the interface between a metal and a dielectric that have a distinct dispersion characteristic and provide a unique way to change the optical emission in a way that is not possible with purely photonic modes. When an optical emitter is placed within the SP's evanescent field it can excite a SP by a near field interaction. If subsequently, these SPs can be coupled out (e.g. by using a grating) the initially non-radiative decay (into a bound SP) is turned into useful far-field radiation again. In this way the emission spectrum and decay rate of the emitter can be significantly changed.

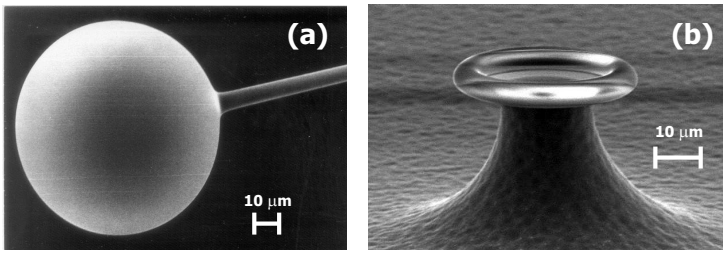

Figure 1.2: Two different dielectric optical microcavities studied in this thesis: (a) microsphere resonator, (b) microtoroid resonator. Typical dimension are of the order of ten to hundred optical wavelengths.

The optical emission also can be strongly modified in optical microcavities. In this thesis we focus on whispering gallery optical microcavities that typically have length scales of the order of ten to hundred optical wavelengths. In these cavities light propagates along closed optical paths, leading to circulation of optical power. Two typical examples of optical microcavities studied in this thesis are shown in Fig. 1.2: silica microsphere resonators (a) and silica microtoroid resonators (b). Despite the small refractive index contrast of these silica microcavities, they present a way to achieve large modification in the optical emission. Due to multiple interference of the circulating light only a limited number of frequencies are allowed within the microcavity. As a consequence, the DOS can be strongly enhanced for the allowed cavity resonances. Figure 1.3 shows a schematic of the DOS as a function of frequency for a closed cavity. In such a cavity, only modes at frequencies resonant with the cavity are present and there is no contribution from the free space DOS. The resulting enhancement in spontaneous emission rate has been described by Purcell [7] for an emitter with a emission linewidth smaller than the cavity resonance. The

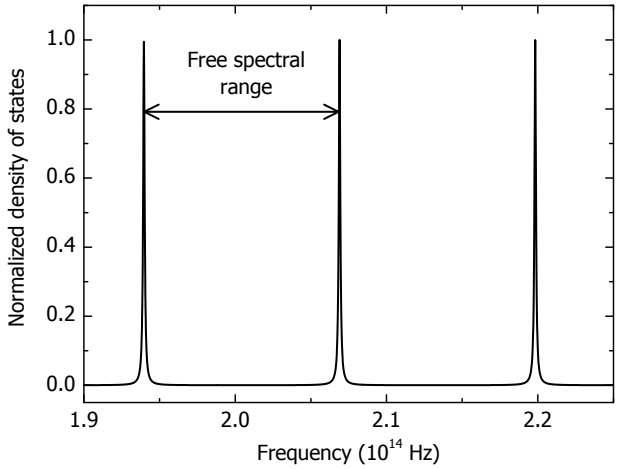

Figure 1.3: Density of states as a function of frequency inside a closed microcavity. Enhancements in decay rate, described by Eq. 1.3, can occur at frequencies resonant with the cavity that are separated by the free spectral range.

spontaneous emission rate enhancement is given by

$$F = \frac{3Q}{4\pi^2 V}\left(\frac{\lambda}{n}\right)^3 \quad , \tag{1.3}$$

where $Q{=}\omega\tau$ is the cavity's quality factor, which is directly proportional to the the time τ that light is confined in the cavity, and V the volume in which the light is confined. As can be seen from Eq. 1.3, large cavity Q and small mode volume V are essential to achieve large Purcell enhancements. In general, enhancements in spontaneous emission rates are smaller than expected from the Purcell factor due to the fact that optical microcavities are open, instead of closed cavities.[8] This leads to an additional decay into free space modes that reduces the observed spontaneous emission rate enhancement.[9]

A direct consequence of the mode structure in the microcavity is that stimulated emission can be achieved more easily than in an unconfined geometry. At high Q, laser light that is used for pumping the optical emitters into inversion is recycled in the cavity, and high field intensities can be built up at the resonant cavity modes. This leads to population inversion at low input powers, and low-threshold lasing can be obtained.

Three-dimensional photonic crystals can provide the ultimate control over spontaneous emission. When properly designed such a photonic crystal can have a complete photonic bandgap, i.e. a range of frequencies where no photonic modes exist, the DOS is zero. Figure 1.4(a) shows the photonic bandstructure for an fcc Si inverse opal photonic crystal, calculated with a plane-wave expansion method.[11] It describes the energy of photonic states for states with

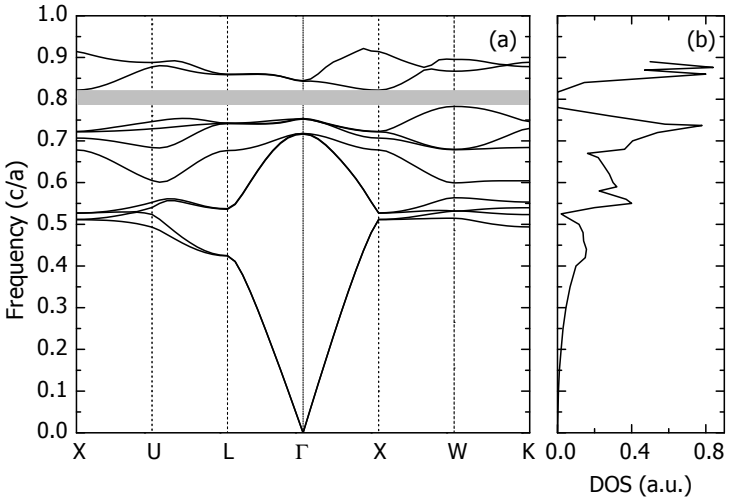

Figure 1.4: Bandstructure calculation for an fcc Si-inverted opal photonic crystal (a). On the vertical axis is the frequency (in units of speed of light (c) normalized to the fcc unit cell size (a)) and on the horizontal axis the normalized wavevector in various reciprocal lattice vector directions of the reciprocal unit cell. In the normalized frequency range of 0.78 to 0.82 no photon states are present. Density of states for the same structure as in (a) integrated over the complete reciprocal unit cell (taken from [10]).

different propagation direction and wavevector. Figure 1.4(b) shows the DOS calculated by integrating over the reciprocal unit cell of the same structure as in Figure 1.4(a).[10] It can be clearly observed from Fig. 1.4(a) and (b) that there is a frequency range where no photonic states are available, the photonic bandgap. For a dipole, whose emission frequency is within this frequency range, spontaneous emission is fully inhibited since there are no photon states available. For frequencies near the bandgap the bands are flat, leading to an enhancement in the DOS; for a dipole emitting at these frequencies the spontaneous emission rate is increased. From the $\mathbf{r}$ dependence of ρ in Eq. 1.1 we can observe that the DOS is a local parameter that depends on the exact position of the dipole within the photonic microstructure. By spatially-selective probing of optical emitters in a photonic crystal, this local DOS can be probed. This can lead to large variations in the spontaneous emission rate, even for photonic crystals without a photonic bandgap.

1.2 Contents of this thesis

In this thesis we demonstrate the control of spontaneous emission of optically active erbium ions in three different types of microphotonic materials. Erbium is a rare-earth ion that, if embedded in a solid, takes on a trivalent state. It shows room-temperature emission from the $^4I_{13/2} \rightarrow ^4I_{15/2}$ intra-4f transition

at 1.5 μm. This wavelength is a standard in telecommunication technology, and therefore, modification of the Er spontaneous emission is of great technological interest.

Part I describes controlled spontaneous emission of Er near a metallo-dielectric interface.

- Chapter 2 describes how the spectral shape of the emission spectrum of Er can be modified by coupling to SPs at a SiO_2/Ag interface. Large angle-dependent changes in emission spectra and emission polarization are observed. The spectral dependence of these changes is compared to calculations based on the SP dispersion relation obtained from the dielectric constants of SiO_2 and Ag. Good qualitative agreement is observed.

- Chapter 3 describes how the decay rate of Er ions can be modified by coupling to SPs. The effect of concentration quenching is taken into account to obtain the radiative decay rate for Er ions near SiO_2/air and SiO_2/Ag interfaces. Large enhancements of the radiative decay rate are observed for Er ions near the SiO_2/Ag interface, largely due to coupling to SPs. The results are compared to calculations based on a classical dipole oscillator model and good quantitative agreement between the calculations and the observed decay rate changes is observed.

- In Chapter 4 we investigate the effect of SP coupling on the decay rate of optically excited Si nanocrystals in SiO_2 near a Ag surface. Using an inverse Laplace transform technique, decay rate distributions are derived from measured stretched-exponential decay curve. The increase in average decay rate for Si nanocrystals near the Ag interface is mainly due to SP excitation and is in good agreement with calculations. From a comparison of the calculations and the experimental results we derive for the first time the internal emission quantum efficiency of Si nanocrystals: 77 %.

- In Chapter 5 we calculate dispersion relations for SPs at various dielectric/Ag interfaces. We present the optimum coupling distance for Er ions in Si to SPs on a Si/Ag interface, as well as the total decay rate for varying dipole emission wavelengths. Using the classical dipole oscillator model we derive, from the power dissipation spectra, the SP dispersion for thin metal films. An array of applications of SPs in microphotonic devices is proposed, including: a SP optical interconnect, a SP light-emitting diode with enhanced quantum efficiency and a SP optical switch.

In Part II we demonstrate controlled emission of Er ions in microcavities.

- Chapter 6 describes the fabrication of a silica microsphere laser using high-energy Er ion-implantation. We show that ion-implantation is compatible with the fabrication high-Q microcavities. By optimizing the Er doping profiles the lasing threshold can be minimized.

- In Chapter 7 we describe the fabrication of toroidally-shaped Er-doped microcavity lasers made using ion-implantation at two different stages in the fabrication process. The spatially resolved spontaneous emission from Er inside the microcavity is measured by confocal photoluminescence spectroscopy, and we demonstrate a modified Er PL spectrum by coupling of Er to cavity modes. Microprobe Rutherford backscattering spectrometry measurements are presented that give detailed information on the effect of the fabrication process on the Er distribution in the microtoroid. The intrinsic microtoroid quality factors and lasing characteristics are investigated. Erbium lasing is observed at thresholds as low as 4.5 μW.

Part III describes controlled spontaneous emission of Er in Si-infiltrated silica colloidal photonic crystals.

- Chapter 8 describes the fabrication of an erbium-doped fcc silicon-infiltrated silica colloidal photonic crystal. Material properties are investigated leading to design criteria for a Si inverse-opal photonic crystal that can strongly inhibit the Er spontaneous emission. It is shown that Er ions can be selectively excited in both the SiO_2 and Si components of this material. Distinctly different lifetimes of Er are observed for the SiO_2 and Si sections of the photonic crystal, partly due to the difference in the electronic transition probability of the intra-4f transition in Er^{3+}.

Part I

Controlled spontaneous emission near a metallo-dielectric interface

Chapter 2

Surface plasmon modified spontaneous emission of erbium in a metallo-dielectric grating

The spectral shape and bandwidth of the emission of Er^{3+} ions in silica glass around 1.5 μm is strongly modified by the presence of a silver grating. The metallo-dielectric grating was made by a sequence of ion implantation in silica glass, dry etching and silver sputter deposition. Spectral enhancements are observed that are attributed to near-field coupling of Er^{3+} ions to surface plasmons that subsequently re-radiate at well-defined resonance conditions. Qualitative agreement is observed between these resonance conditions and calculations based on the surface plasmon dispersion relation. Applications of the Er surface plasmon coupling are discussed.

2.1 Introduction

Erbium ions play a key role in optical communication systems operating at 1.53 μm. The 1.53 μm emission is due to radiative intra-4f transitions that occur between the $^4I_{13/2}$ and $^4I_{15/2}$ manifolds of Er^{3+}. These manifolds are composed of a multitude of Stark levels, the number of which is determined by the site symmetry of the Er ion in the host. The absorption and emission spectra of Er are thus determined by Boltzmann distributions over the ground and excited manifolds and hence, at a certain temperature the Er emission spectrum is fixed for a given material. Many applications of Er-doped materials depend critically on the exact line shape of the emission. For example, in wavelength-division multiplexing systems, the systems bandwidth is determined by the width of the spectrum. Hence, it would be extremely interesting if the Er emission spectrum could be externally modified.

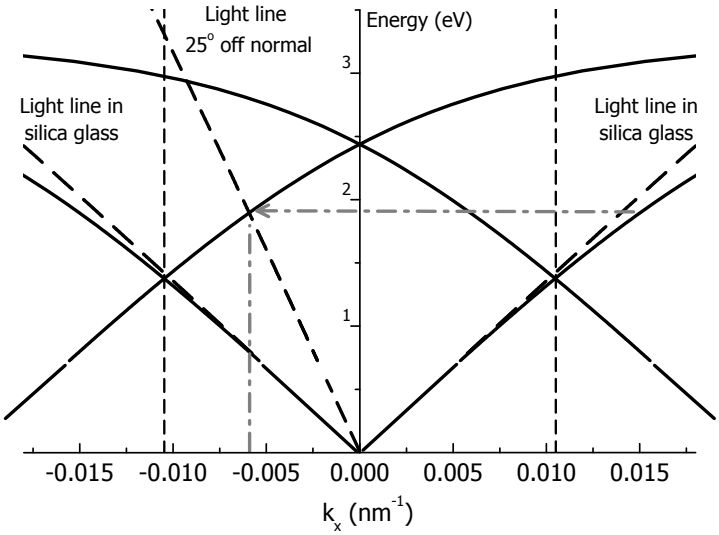

Figure 2.1: Surface plasmon dispersion relation in the presence of a surface grating. The dashed vertical lines indicate the boundaries of the reduced Brillouin zone. The grating vector **G** is indicated.

A surface plasmon (SP) is an electromagnetic wave propagating at the interface between a metal (ϵ_m) and a dielectric (ϵ_d) coupled to surface charge oscillations.[12] The SP is bounded mode if the real part of the dielectric constant of the metal is negative (ϵ_m<1), with its absolute value larger than ϵ of the dielectric ($|\epsilon'_m|>\epsilon_d$). At a particular frequency the momentum of a SP, given by $k_{SP} = (\omega/c)\sqrt{\epsilon_d\epsilon_m/(\epsilon_d + \epsilon_m)}$, is always larger than that of a plane wave travelling parallel to the interface ($k_{pw} = (\omega/c)\sqrt{\epsilon_d}$). Therefore it cannot couple directly to a plane wave (or vice versa) and, as a result, its energy is lost due to Joule heating of the metal. However, if the interface has a periodic corrugation (i.e. a grating), the momentum of the SP can be decreased by

diffraction on the periodic corrugation at the interface and re-radiate into a photon. The grating allows to add or subtract multiples of the grating vector from the SP wavevector. This is shown in Fig. 2.1 where the SP dispersion relation is shifted with a multiple of the grating vector (indicated by **G**). Due to the grating vector periodicity, the complete dispersion behavior can be understood from the dispersion in the reduced Brillouin zone (area bounded by dashed vertical lines). At a fixed energy, and for the particular grating vector **G** plotted in Fig. 2.1, the SP dispersion line crosses a dispersion line within the reduced Brillouin zone for light travelling at an angle of 25^o relative to the normal. At this angle the SP can be coupled out as a plane wave into the far-field (or vice versa).

In this chapter we show that a large change in the emission spectrum of Er-doped silica glass can be achieved by coupling Er ions to SPs in a metallo-dielectric grating by means of a near-field interaction. The SPs are coupled out using the above described technique of grating coupling.

2.2 Experimental

To investigate the Er-SP coupling, an Er-doped metallo-dielectric grating was made in the following way. Heraeus silica glass slides (Herasil 1) of 500 μm thickness were cooled to 77 K and implanted with $1.2{\cdot}10^{15}$ Er/cm^2 at an energy of 350 keV. The ion range and straggle are 120 nm and 35 nm respectively, as measured by Rutherford backscattering spectrometry. An optical grating was then fabricated in the implanted side of the silica glass by electron beam lithography and dry-etching. The samples were first spin-coated with a photoresist and then baked at 200 ^{o}C. A 30 nm Ge layer was sputter-deposited, followed by spin-coating of a layer of positive resist (4 % PMMA in Cl-benzene). A grating pattern with a pitch of 1070 and a width of 530 nm was written in the PMMA using an electron beam pattern generator. The total grating area was 1 mm^2. After development of the PMMA the exposed Ge was etched with a Cl plasma. Subsequently, the photoresist was etched with an O_2 plasma. The final etching step into the silica glass was done with a CHF_3/O_2 plasma (100/2 sccm, respectively). Subsequently, the remaining resist layer was removed with HNO_3. The samples were then annealed at a temperature of 800 ^{o}C for one hour in vacuum to increase the luminescence yield of the implanted Er.[13] Next, a Ag layer was sputter-deposited onto the grating. From optical diffraction as well as reflectivity measurements and accompanying calculations based on the numerical method of exact eigenvalues and eigenfunctions [14] the structural parameters of the Ag grating were determined: depth 230 $\pm$ 10 nm, pitch 1070 $\pm$ 1 nm and width of the silver grating bars 500 $\pm$ 10 nm.

Figure 2.2(a) shows a scanning electron microscopy image of the cross section of the silica grating with the deposited Ag layer on top. The Ag film shows good conformity with the silica grating, but has somewhat lost adhesion to the substrate at the cleft. Further away from the cleft the Ag film is in contact with the silica throughout the entire cross-section of the grating. The Ag layer

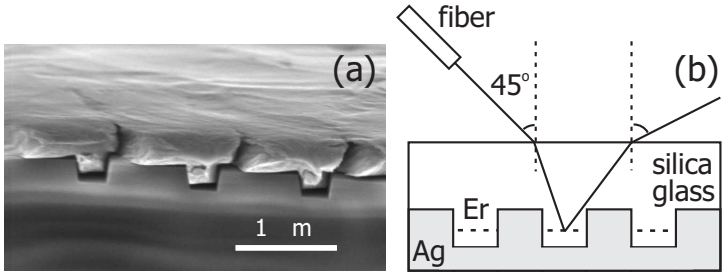

Figure 2.2: (a) Scanning electron microscopy image of a cross section through the grating; (b) Schematic of the experimental set-up.

thickness was 300 nm, i.e. thicker than the depth of the grating. In this way a metallic grating with a dielectric top layer was made, where the dielectric acts as a host and a spacer for the Er^{3+} ions above the grating (see schematic in Fig. 2.2(b)).

Photoluminescence (PL) spectroscopy measurements were performed at room temperature. An argon-ion laser operating at λ_{exc}=488 nm was used to excite the Er^{3+} ions into the $^4F_{7/2}$ manifold. The laser intensity was time modulated with an acousto-optical modulator and fed into a polarization maintaining fiber. The fiber axis was aligned with the polarization direction of the laser light such that light at the output of the fiber was polarized with an s over p intensity ratio of at least 30. The output of the fiber was focused from the silica side onto the grating (see schematic Fig. 2.2(b)) using a microscope objective (spot diameter $\sim$700 μm). The fiber was mounted at an angle of 45^o relative to the surface normal onto the rotating sample stage, thereby keeping the excitation angle fixed during rotation (the corresponding internal angle in the silica glass is 29^o). The excitation power at the sample was measured at the exit of the pump fiber with a Si photodiode. PL was collected with an f=10 cm lens and filtered by a long-pass filter (λ>846 nm) to remove any intensity left from the pump. The in-plane collection angle was 16^o. PL was analyzed with an infrared polarizer and dispersed with a 480 mm focal-length monochromator. The spectral resolution was 6 nm. The collected PL was detected by a liquid-nitrogen cooled Ge diode in combination with a standard lock-in technique.

2.3 Results

Figure 2.3 shows normalized PL spectra taken at various angles relative to the surface normal (angle θ in the schematic and insets). Data are shown for two orientations of the grating as shown by the schematics under the figure. In Fig. 2.3(a) the grating vector $\mathbf{G}$ is in the plane of measurement ($\mathbf{G}_{||}$) and only data for p-polarized emission is plotted. At θ=40^o an emission spectrum

characteristic for Er^{3+} in bulk silica glass is observed. At θ=20^o only a slightly different spectral shape is observed. However at θ=0^o, a strongly increased spectral contribution compared to that of Er^{3+} in bulk silica glass is observed for the long wavelength part of the spectrum (λ>1530 nm). In Fig. 2.3(b), **G** is perpendicular to the plane of measurement ($\mathbf{G}_\perp$) and only data for *s*-polarized emission are plotted. Here for all angles well-defined peaks are observed, superimposed on the spectrum for Er^{3+} in bulk silica glass. The peak wavelength decreases with increasing angle. An example of the contribution of such a peak is shown by the dashed line for θ=25^o that was obtained by a division and rescaling of the measurement with a reference spectrum.

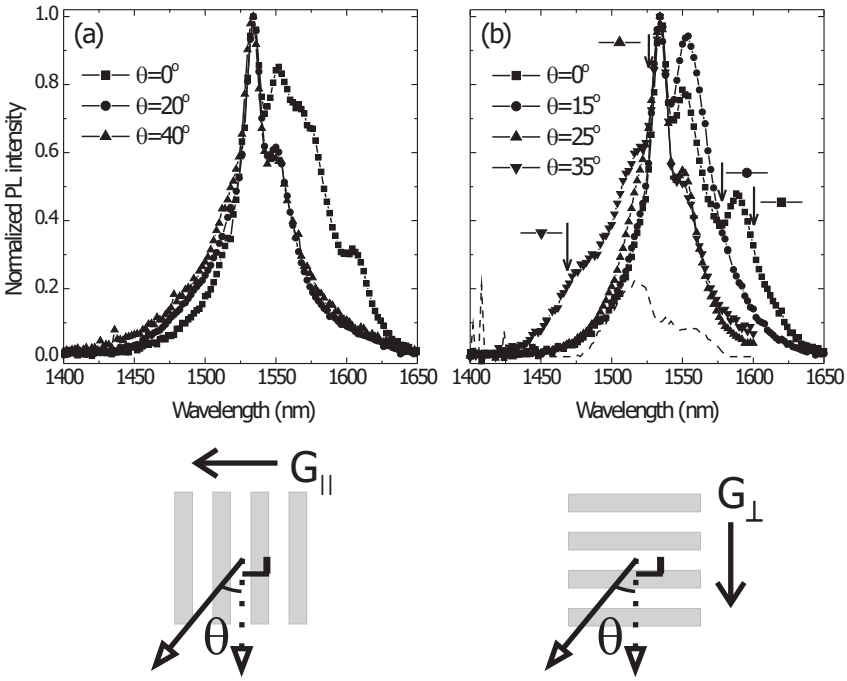

Figure 2.3: Photoluminescence of Er-doped metallo-dielectric gratings (λ_{exc}=488 nm, resolution 6 nm) measured at various angles θ (see schematic of measurement geometry under (a) and (b) and in Fig. 2.2(b)). (a) Grating vector in the plane of measurement ($\mathbf{G}_{||}$); data for *p*-polarized emission; (b) grating vector perpendicular to the plane of measurement ($\mathbf{G}_\perp$); data for *s*-polarized emission. In both cases the spectra are composed of a spectrum characteristic for Er^{3+} in bulk silica glass, with superimposed a contribution from re-radiated SPs. The arrows in (b) indicate the measured peak wavelength of the contribution of the re-radiated SPs for each angle. For θ=25^o the dashed line shows a spectrum that was obtained by a division and rescaling of the measurement with a reference spectrum, showing the enhancement in PL at the position of the arrow.

Figure 2.4 shows the PL intensity at a fixed wavelength of 1534 nm as a function of angle for s and p polarization. Figure 2.4(a) shows data for $\mathbf{G}_{||}$. A clear PL enhancement is observed around θ=10^o for p-polarized emission. No enhancement is observed for s-polarized PL. In Fig. 2.4(b) the opposite is observed. It shows data for $\mathbf{G}_{\perp}$ where an enhancement is observed around θ=25^o for s-polarized PL. No enhancement is observed for p-polarized PL.

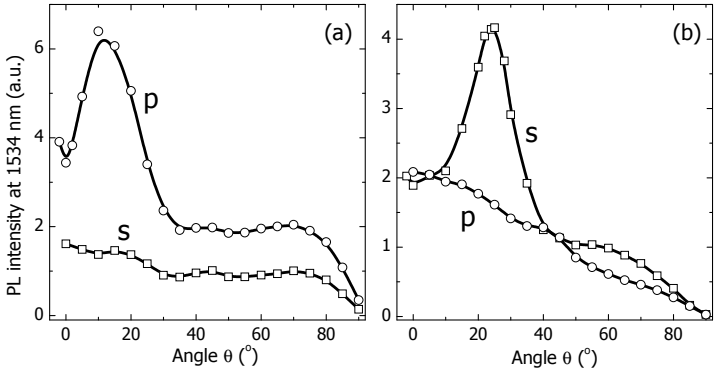

Figure 2.4: Photoluminescence intensity of Er-doped metallo-dielectric gratings at 1534 nm as a function of emission angle θ for both s and p polarization. (a) Data for the grating vector in the plane of measurement ($\mathbf{G}_{||}$); (b) data for the grating vector perpendicular to the plane of measurement ($\mathbf{G}_{\perp}$).

The enhancements observed in Fig. 2.3 and Fig. 2.4 are attributed to re-radiating SPs that couple out at well-defined resonance conditions. The SPs are excited by the near field of the Er^{3+} ions and propagate in all directions along the interface. The observed spectrum in Fig. 2.3 is then a linear superposition of the spontaneous emission spectrum for Er^{3+} in bulk silica glass and the re-radiated SPs collected at the measurement angle. The enhancements in Fig. 2.4 show the angles at which a re-radiated SP occurs if it is excited at an energy corresponding to a wavelength of 1534 nm. Since the damping distance of the propagating SP is estimated to be of the order of 100 μm (calculated at 1.5 μm for a planar interface), i.e. many grating periods, the peaks in Fig. 2.4 are expected to be very sharp. The fact that in Fig. 2.4 a relatively broad width is observed is due to the relatively large collection angle that was used in these measurements. Reference measurements were performed on samples from the same Er^{3+} doped silica glass slide either covered with a planar Ag mirror or not covered (air). These only show a gradual decrease of PL with angle comparable to that for s-polarized light in Fig. 2.4(a) and p-polarized light in Fig. 2.4(b). This gradual decrease in PL for increasing emission angle is due to the increasing internal reflection coefficient of the air/silica glass interface as well as the decreasing internal collection angle. Note also that due to refraction at the air/silica glass interface the maximum internal angle at which light from the grating is detected is 44^o, the angle of total internal

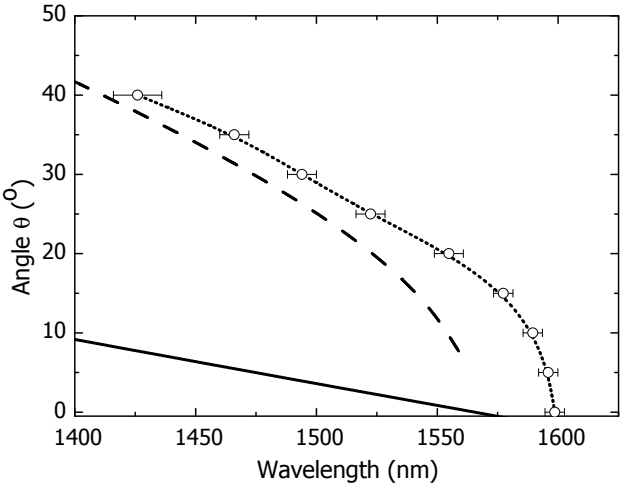

Figure 2.5: Resonance angles for SP re-radiation for the two grating orientations calculated from the dispersion relation, Snell's law and Eq. 2.1; $\mathbf{G}_{||}$ (solid line) and $\mathbf{G}_{\perp}$ (dashed line). For $\mathbf{G}_{\perp}$ the measured peak wavelengths, among others derived from the data in Fig. 2.3(b), are shown (open circles). The dotted line is a guide to the eye.

reflection at the air/silica glass interface.

To quantitatively analyze the data, the optical constants of both the Ag film and silica glass substrate were measured with spectroscopic ellipsometry. We found ϵ_{silica}=2.1 and ϵ_{Ag}=-98.07+i6.95 at 1.5 μm. Using these data the dispersion relation for a SP propagating along a planar Ag/silica glass interface was calculated. For arbitrary grating orientation conservation of the tangential component of the wavevector leads to the resonance condition

$$\mathbf{k}_{0||} = \mathbf{k}_{SP} \pm m\mathbf{G} \qquad , \tag{2.1}$$

where $\mathbf{k}_{0||}$ is the projection of the photon wave vector in the silica glass onto the interface ($|\mathbf{k}_{0||}|=|\mathbf{k}_0|\sin\theta_{int}$, θ_{int} being the internal angle of the photon wavevector), $\mathbf{k}_{SP}$ the SP wave vector, $\mathbf{G}$ the grating vector and m an integer. Since $|\mathbf{k}_{SP}|>|\mathbf{k}_{0||}|$ one or more grating vectors must be added or subtracted from the SP wave vector to obey the resonance condition, leading to the enhanced PL. For the sample geometry studied only the resonance for m=1 is observed as the higher order resonances occur at $\theta_{int}>44^o$, for which external collection is obscured by total internal reflection at the air/silica glass interface. With Eq. 2.1, the SP dispersion relation, and Snell's law the external angle θ_{ext} was calculated at which a re-radiated SP occurs in the PL spectrum if it was excited at frequency ω. To facilitate qualitative comparison with the data these angles are plotted versus vacuum wavelength in Fig. 2.5. The calculated angles are shown in Fig. 2.5 by the dashed line for the $\mathbf{G}_{\perp}$ case.

We can now compare these data with the peak wavelengths observed in Fig. 2.3(b). Exact values for the peak wavelengths were determined by dividing the PL spectra in Fig. 2.3(b) by the PL spectra measured for Er^{3+} in silica glass above a planar Ag mirror. These are indicated by arrows in Fig. 2.3(b) and are also plotted as a function of angle in Fig. 2.5 (open circles). Clearly the same gradual trend of decreasing angle with increasing wavelength is observed in both the experimental data and calculations. The error in the determination of the peak wavelength becomes larger for smaller wavelengths due to a decrease in intensity and an increase of the width of the enhancement. Experimentally, for all wavelengths the coupling occurs at a larger angle than found in the calculation. This can be understood from the fact that the calculation is done for a planar interface, rather than the actual structure, a corrugated interface. Indeed surface corrugation changes the SP dispersion relation in a way that leads to an increased SP wave vector,[15] and thus to an increased resonance angle for a particular wavelength, as is observed.

Fig. 2.5 also shows a calculation for $\mathbf{G}_{||}$ (solid line) that shows much less change of the angle at which the SP re-radiates versus wavelength. From these calculations we only expect enhancements in the Er^{3+} emission spectrum for angles between 0^o and 10^o. As here too, surface corrugation leads to an increased resonance angle compared to the case for a planar film, the calculation is in qualitatively agreement with the data in Fig. 2.3(a) and 2.4(a). The polarization dependence observed in Fig. 2.4 is in agreement with data by Kitson et al.,[16] who have measured the polarization-dependent emission of a dye above a sinusoidal Ag grating. Also, photo-acoustic measurements by Inagaki et al.,[17] showed similar polarization dependence in reflection.

These data demonstrate the use of Er ions as a source for infrared SPs at the important 1.5 μm telecommunication wavelength. Because SPs in the infrared have large propagation lengths, they could be used in 2D-plasmon optics experiments.[18] In contrast to what is typically observed with dyes [16] and rare earth complexes,[19] Er ions in silica glass show no photo bleaching. The long lifetime of Er in silica glass (and hence a high internal quantum efficiency) enables the study of radiative and non-radiative components in the Er-SP coupling. As an interesting implication of this work we suggest that a proper design of the Er-SP coupling can significantly enhance the emission efficiency of Er-doped materials with low QE (e.g. Er-doped silicon, Er-doped polymers). If the excited Er^{3+} couples to SPs at a rate comparable to the intrinsic non-radiative decay rate and if the SPs can subsequently be coupled out to photons with high efficiency (which is possible [20]), the overall efficiency can dramatically increase.

2.4 Conclusions

In summary we have shown a significant modification of the photoluminescence spectrum of Er^{3+} in silica glass by coupling to surface plasmon polaritons in a metallo-dielectric grating, which subsequently re-radiate at well-defined

resonance conditions. The spectral enhancements are in qualitative agreement with a model based on the SP dispersion relation that was calculated using experimentally determined dielectric constants. The data have implications for infrared plasmon optics and engineering of the quantum efficiency of optical emitters.

Chapter 3

Surface plasmon modified spontaneous emission rate of erbium near a metallo-dielectric interface

Er^{3+} ions located 100 nm beneath the surface of silica glass show an enhanced photoluminescence decay rate when the glass is covered with Ag. Correcting for concentration quenching effects, the decay rate is enhanced by 70 %, compared to the case without Ag. The data are in agreement with a model that takes into account variations in local density of states and excitation of surface plasmons and lossy surface waves, resulting in direct evidence for the efficient generation of surface plasmons by excited Er^{3+} ions. Using the model, optimum conditions for coupling to surface plasmons are derived, which can be used to enhance the emission rate and quantum efficiency of a wide range of Er-doped materials.

3.1 Introduction

Trivalent erbium ions, with their characteristic $^4I_{13/2} \rightarrow ^4I_{15/2}$ intra-4f transition at 1.53 μm, play a key role in a wide variety of optical and opto-electronic devices. They provide the gain medium in optical telecommunication amplifiers and lasers, and provide a source of electroluminescence in a range of Si-based opto-electronic devices. However, due to the parity forbidden character of the intra-4f transition, the radiative emission rate of Er^{3+} is very low, typically in the range 50-1000 s^{-1}. Consequently, the output power and modulation speed of Er-doped light-emitting diodes or lasers is limited. Moreover, the low radiative rate makes the Er emission sensitive to non-radiative decay processes, such as Auger recombination [21] and energy backtransfer in Si,[22] or upconversion and concentration quenching in silica glass.[23] Several key limitations in Er-based photonic materials technology could be resolved if the radiative emission rate of Er could be artificially enhanced. We propose to enhance the Er radiative decay rate by coupling to surface plasmons (SPs). Surface plasmons are electromagnetic waves bounded at, and propagating along, the interface between a metal and a dielectric, coupled to surface charge oscillations.[12] An electric dipole, positioned close to such an interface can decay by the excitation of a SP. As was recently demonstrated for Eu and Er ions,[19][24] the propagating SP can be coupled out into the far field using a grating that relaxes the momentum mismatch between SP and photon. This process thus contributes to the far-field emission of the emitter, effectively increasing its radiative emission rate.

In this chapter, we focus on the details of the coupling of an excited Er ion to a metal. We experimentally demonstrate that the photoluminescence decay rate of Er ions in silica glass is enhanced near a Ag interface. The increase of the decay rate (corrected for concentration quenching effects) is consistent with a model that describes the combined effect of variations in local density of states and excitation of SPs and lossy surface waves. The model is then used to predict optimum conditions for radiative rate and quantum efficiency (QE) enhancements for infrared emission of Er.

3.2 Experimental

The surface region of sodalime-silicate glass samples was doped with Er by 500 keV Er^+ ion implantation. Ion fluences ranged from (1-6)$\cdot 10^{15}$ Er/cm^2, resulting in peak concentrations ranging from 0.12-0.71 at.%. To avoid charging during the ion implantation the samples were covered with a 40 nm thick Al layer, which was removed after ion implantation with a KOH etch. The samples were annealed in vacuum for one hour at 512 ^{o}C, a procedure known to remove all implantation related defects.[23] The Er depth profile as measured by Rutherford backscattering spectrometry is described by a Gaussian distribution that is centered at 103 nm with a straggle of σ=43 nm. Finally, one section of each sample was covered with an optically thick (225 nm) Ag film using sputter

deposition. The dielectric constant of the Ag film, measured at λ=1538 nm using ellipsometry, was ϵ_{Ag}= -41.8+ i4.6.

Photoluminescence (PL) measurements were performed at room temperature on either air or Ag covered sections of the Er-implanted samples. An argon-ion laser operating at 488 nm was used to excite the Er^{3+} ions into the $^4F_{7/2}$ manifold. The laser intensity, modulated at 6 Hz with an acousto-optical modulator, was incident though the transparent back side of the sample. PL was collected from the back using an f=10 cm lens and dispersed using a 480-mm focal-length monochromator, set to a spectral resolution of 6 nm. The collected and dispersed PL intensity was recorded by a liquid-nitrogen cooled Ge diode with a response time of 30 μs. PL decay traces were taken using a digitizing oscilloscope, integrating a large number of decays.

3.3 Results

The inset of Fig. 3.1 shows a PL spectrum for Er-implanted sodalime-silicate glass covered with Ag. An identical spectrum is observed for the section of the sample without Ag, indicating that the presence of the metal does not affect the crystal field around the Er^{3+} ions and the atomic dipole transition matrix element is identical for the two cases. Two PL decay traces are shown,

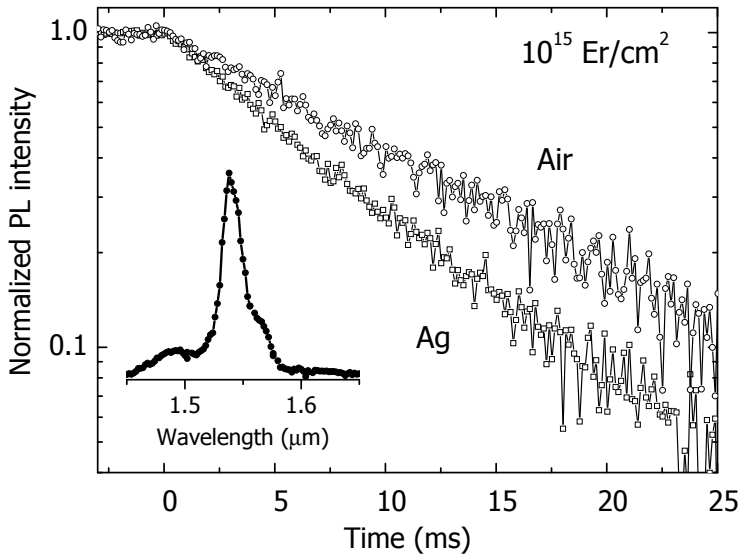

Figure 3.1: PL decay curves measured at λ=1538 nm for a sample doped with $1{\cdot}10^{15}$ Er/cm^2. The 488 nm laser was switched off at t=0. The decay for the sample in air is slower than for the sample covered with Ag. The inset shows the Er emission spectrum for the sample covered with Ag.

taken at the Er peak emission wavelength of 1538 nm, for the sample implanted with $1{\cdot}10^{15}$ Er/cm^2, for the air and Ag covered sections of the sample. The decays are single-exponential, and the PL decay rate for the Ag-covered section (131 s^{-1}) is enhanced compared to the PL decay rate for the air-covered section (87 s^{-1}).

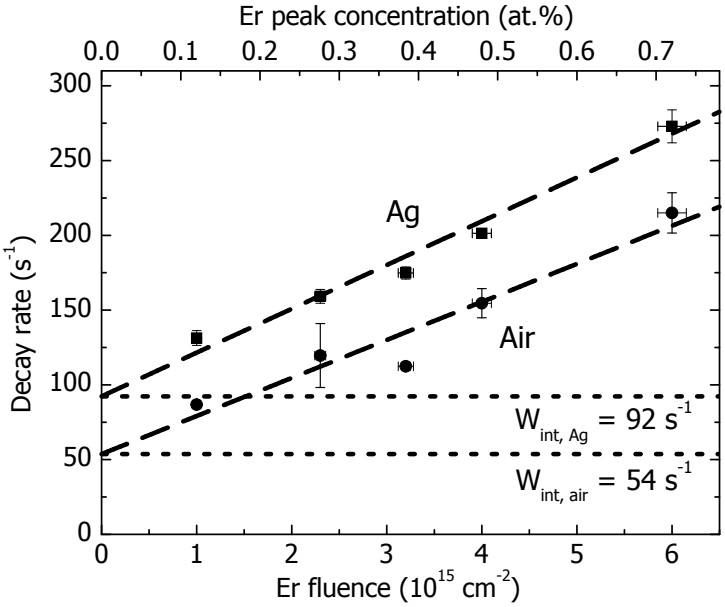

Figure 3.2: PL decay rates measured at λ=1538 nm for samples implanted with different Er fluences, for the sample in air or covered with Ag. The decay rate increases linearly with concentration due to concentration quenching. The dotted horizontal lines indicate the extrapolated decay rates at zero Er concentration.

Figure 3.2 shows the PL decay rates measured at a wavelength of 1538 nm for the air and Ag covered sections of samples with different Er content. The PL decay rate increases with increasing Er concentration, a well-known effect that is attributed to concentration quenching (a process due to Förster energy transfer between Er ions, followed by quenching).[23] It has been shown that the main quencher in these glasses are OH impurities,[23] whose first stretch-vibration overtone is resonant with the 1.5 μm transition of Er^{3+}. If the concentration of quenchers is much smaller than the concentration of Er^{3+} ions, as is the case for our samples, the PL decay rate is described by [25][26]

$$W_{PL} = W_{int} + 4\pi C_{Er-Er} N_Q N_{Er} \quad , \tag{3.1}$$

with W_{int} the Er^{3+} intrinsic decay rate in absence of concentration quenching, C_{Er-Er} an Er-Er interaction constant, N_Q the concentration of quenchers, and N_{Er} the Er^{3+} concentration. Fitting Eq. 3.1 to the two data sets in Fig. 3.2 we find the extrapolated Er decay rate in absence of concentration quenching:

$W_{int,air}$=54 ± 7 s^{-1} for the air section and $W_{int,Ag}$=92 ± 4 s^{-1} for the Ag section. Adding the Ag film onto the glass thus enhances the intrinsic Er decay rate by (70 ± 25) %. From the slopes in Fig. 3.2, and using an OH (quencher) concentration of $8{\cdot}10^{18}$ OH/cm^3 [23] we find C_{Er-Er}= (2.7-3.1)$\cdot 10^{-39}$ cm^6/s, which is a typical value for sodalime silicate glass.[23]

We describe the interaction between an oscillating dipole and a metal interface with a model developed by Ford and Weber.[6] In this one-dimensional model, a harmonic oscillator dipole is driven at constant power and placed in a dielectric layer (ϵ_d), which is embedded in a stack of layers with arbitrary dielectric constants. The power dissipation of the dipole is determined by calculating the imaginary part of the dipole moment times the electric field at the position of the dipole (see Eq. 1.2). The electric field is due to contributions from the dipole, and the fields reflected by the dielectric surrounding the dipole. After a spatial Fourier transform of the dipolar field into plane waves, the reflected fields can be calculated using the Fresnel reflection and transmission coefficients for all interfaces. The total power dissipation is then calculated for all in-plane wave vectors ($k_{||}$). If the dipole is embedded in an infinitely thick dielectric layer, power is dissipated only for in-plane wave vectors that are smaller than the dipole's far-field wave vector in its embedding dielectric medium ($k_{||} \leq k_d = (\omega/c)\sqrt{\epsilon_d}$), i.e. evanescent waves do not transport energy. However, if an absorbing medium with a smaller real part of the dielectric constant is located within the near-field of the dipole, power is also dissipated for wave vectors $k_{||} > k_d$. Using Ford and Weber's model, we calculated the power dissipation of a dipole emitting at λ_{vac}=1538 nm (the Er^{3+} peak emission wavelength) in sodalime silicate glass (ϵ_d=2.25) both for an air (ϵ_{air}=1) and Ag covered section (ϵ_{Ag}=-41.8+i4.6).

Figure 3.3(a) shows the power dissipation spectrum at λ_{vac}=1538 nm calculated for a randomly oriented dipole at a distance d=103 nm (the peak depth of the Er distribution in the experiments) for the case of the glass in air. As can be seen, power is dissipated for wave vectors $k_{||}/k_d \leq 1$. The cut-off at $k_{||}/k_d$=1 (dashed vertical line) shows that all power is dissipated into the far field, and that there is no absorption for larger wave vectors. Figure 3.3(b) shows the dissipated power spectrum for the corresponding case for the glass covered with Ag. The power dissipation shows the spontaneous emission contribution for $k_{||}/k_d \leq 1$. A large peak is observed at $k_{||}/k_d$=1.027 (see inset), which corresponds to the wave vector of a SP at the silica glass/Ag interface. Power dissipation for even larger wavevectors is due to the excitation of lossy surface waves: energy transfer to the metal owing to the imaginary part of the dielectric constant (i.e. electron scattering).[6][27]

The total decay rate is calculated by dividing the power dissipation, integrated over the complete wave vector range, by the energy of the dipole field. The decay rates are averaged over parallel and perpendicular orientations relative to the interface, and normalized relative to the bulk value. Calculations were performed for distances from the interface in the range of 1-1500 nm, and convergence to within 1 % was achieved for all distances larger than 5 nm. To partition the total decay rate of the dipole ions near the Ag/glass interface into

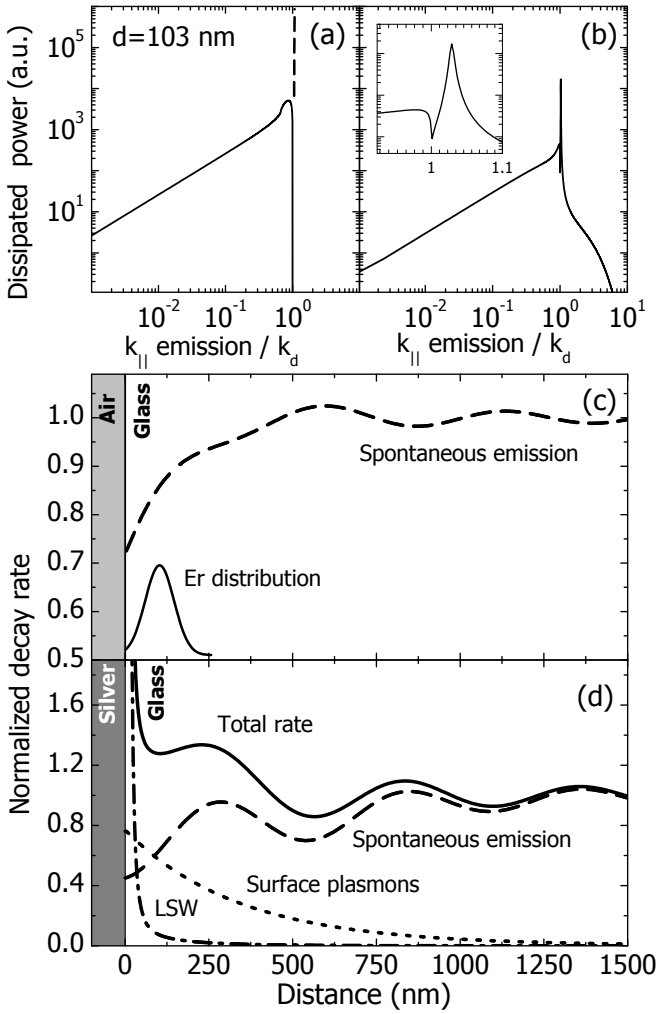

Figure 3.3: Power dissipation as a function of normalized in-plane wavevector, calculated for a randomly oriented dipole emitting at λ_{vac}=1538 nm and positioned at d=103 nm for (a) a glass/air interface, and (b) a glass/Ag interface. The large peak in (b) is due to coupling to surface plasmons, a feature that is more clearly illustrated in the inset. Calculated normalized decay rate as a function of distance from (c) the glass/air interface, and (d) the glass/Ag interface. For (d) the total decay rate is split up into three decay channels, including lossy surface wave excitation (LSW).

the three decay channels, the spectra in Fig. 3.3(b) were integrated over the corresponding wave vector ranges (spontaneous emission: $k_{||}/k_d < 1$, SP excitation: $1 \leq k_{||}/k_d < 2k_{SP}\text{-}1 = 1.056$,[28] lossy surface waves: $1.056 \leq k_{||}/k_d \leq 200$).

Figure 3.3(c) shows the normalized spontaneous emission rate (in this case equal to the total decay rate) of the dipole for the case of the glas in air, as a function of distance from the surface. The decay rate shows an oscillation with depth due to the reflection of emitted waves that, by either constructive or destructive interference, decrease or increase the dipole's decay rate. The oscillations represent variations in the local density of states, an effect that previously has been probed experimentally by placing Eu or Er ions at different distances from the interface.[29][4][30] Figure 3.3(d) shows the depth dependent normalized decay rates for the glass covered with Ag. The spontaneous emission rate shows oscillatory behavior as in Fig. 3.3(c), though with a larger decrease near the surface, due to the higher reflectivity of the interface. Figure 3.3(d) also shows a clear SP excitation component that exponentially decreases with depth as the dipolar near field moves further away from the Ag. The figure shows that for very small distances (d<20 nm) the decay is dominated by the generation of lossy surface waves. At d=90 nm the SP excitation rate is roughly equal to the spontaneous emission rate.

The effect of the various decay processes on the experimentally prepared Er-doped samples can be evaluated by integrating the depth-dependent rates for each of the decay channels over the Er depth distribution (shown in Fig. 3.3(c)). From this analysis it follows that the total decay rate on the Ag/glass interface is enhanced by a factor of 1.52, relative to the total decay rate for the air/glass interface. This is close to the experimentally determined ratio of intrinsic decay rates of 1.7 $\pm$ 0.25 derived from Fig. 3.2.

The correlation between experiment and theory presented here demonstrates that Er^{3+} ions can couple efficiently to SPs at the Ag/silica glass interface. This provides direct support for the results shown in Chapter 2 that showed large modifications in the spontaneous emission spectrum of Er ions embedded in a metallodielectric grating that were interpreted in terms of the near-field generation of SPs by excited Er^{3+} ions.[24] To illustrate how coupling to SPs may eventually serve to enhance the Er emission quantum efficiency (QE) we evaluate data for the sample with the highest Er concentration in Fig. 3.2. The Er ions for the air-covered sample have an internal QE of 26 %, due to concentration quenching. The Er ions in the sample covered with Ag show a further enhanced decay rate due to coupling to SPs. If the latter can be coupled out into the far field at an efficiency of 100 %, the external QE would increase to 35 %. Note that extraction efficiencies for SPs as high as 80 % have already been demonstrated.[20]

Although the emission rate and QE enhancements presented here are relatively small, they clearly demonstrate the concept of coupling to SPs in the near-infrared. As the experiments are in agreement with theory, we can now use the latter to search for more effective ways to enhance emission rates and QEs by coupling to SPs. The relatively weak coupling of Er to SPs at the Ag/silica glass interface is caused by the large difference between the Er emission fre-

quency and the Ag plasma frequency.[31] There are several ways to increase the coupling to SPs (and thereby the decay rate and QE enhancement): 1) using a dielectric with higher dielectric constant (e.g. Si), 2) using a different metal (e.g. Au), or 3) by coupling to a thin metal film rather than an optically thick layer.[30] Calculations based on the previously described model show that the SP excitation rate for a dipole in Si (ϵ_d=11.9) emitting at λ_{vac}=1538 nm and positioned at a distance of 20 nm from a 10 nm thin Ag film is 12 times larger than the bulk spontaneous emission rate.

3.4 Conclusions

In conclusion, the decay rate of optically excited Er^{3+} ions near a glass surface is enhanced by 70 % if the glass is covered with Ag. The enhancement is in good agreement with a model that takes into account variations in the local density of states, excitation of surface plasmons and lossy surface waves, with the majority of the decay rate enhancement due to SP excitation. Much larger enhancements are expected for an optimized metallo-dielectric geometry. If these SPs can be efficiently coupled out, the emission rate and QE of excited Er ions can be enhanced. In this way, fundamental quenching processes of Er in Si and silica glass may be avoided. The next challenge is to experimentally demonstrate this.

Chapter 4

Excitation of surface plasmons at a SiO_2/Ag interface by silicon nanocrystals

Silicon nanocrystals, located near a Ag interface, excite surface plasmons at the SiO_2/Ag interface. Si nanocrystals are formed in the near-surface region of glass by Si ion implantation and thermal annealing. Photoluminescence (PL) measurements show stretched-exponential PL decay. Using an inverse Laplace transform of the measured decay curves, the decay rate distributions are derived. An average decay rate is obtained from the decay rate distribution for Si nanocrystals near a SiO_2/air and a SiO_2/Ag interface. For Si nanocrystals spaced 44 nm from the interface the average decay rate is enhanced by a factor 1.8 due to the proximity of the Ag interface. Calculations based on a classical dipole oscillator model show that the observed decay rate enhancement is mainly due to the excitation of surface plasmons. From a comparison of the experimental and theoretical results the Si nanocrystal internal quantum efficiency was estimated to be (77 ± 17) %. Using thin metal films the excitation of surface plasmons by Si nanocrystals can be further enhanced. Si nanocrystals can preferentially excite symmetric thin-film surface plasmons. This work provides design criteria for an electrically pumped Si nanocrystal-based mode selective surface plasmon source.

4.1 Introduction

Silicon nanocrystals are crystalline clusters [32] of 100-10000 Si atoms that show quantum-confined luminescence at wavelengths in the visible or near infrared. Several micro and nano opto-electronic technologies based on Si nanocrystals have been developed. Si nanocrystal-based light-emitting diodes have been demonstrated,[33][34] as well as non-volatile memory devices based on charge storage in Si nanocrystals.[35] Also it has been suggested that optical gain from Si nanocrystals may lead to the fabrication of an all-Si laser [36] (i.e. fully compatible with Si integrated-circuit manufacturing). The use of Si nanocrystals in many of these opto-electronic devices requires precise control over their luminescence properties in often quite complex optical geometries. As first suggested by Purcell in 1946,[7] the spontaneous emission rate of an emitter not only depends on the electronic transition probability, but also on its dielectric surrounding. In dielectrics this is described by the local photonic density of states,[37] that determines the spontaneous emission rate. This has been demonstrated for rare-earth ions in glass or Cr ions in Al_2O_3 near a dielectric interface.[4][38] Also in photonic crystals modified spontaneous emission has been demonstrated.[39][40][41] For an optical emitter near a metal, additional decay processes can occur, such as surface plasmon (SP) and lossy surface wave excitation, that modify the spontaneous emission.[29][27][24]

In this chapter we study the interaction between Si nanocrystals embedded in SiO_2 and a Ag film. By varying the distance between the Si nanocrystals and the Ag we demonstrate that Si nanocrystals show an increased decay rate that is mainly due to the excitation of SPs. As we will discuss, excitation of SPs that are subsequently coupled out into the far field, can lead to an increased radiative decay rate and greater emission efficiency of Si nanocrystals. We describe various possible ways to optimize the coupling of Si nanocrystals to SPs to enhance these effects. From the data we also derive the internal quantum efficiency (QE) of Si nanocrystals.

4.2 Experimental

We create optically active Si nanocrystals in SiO_2 near a Ag surface in the following way. The near-surface region of suprasil quartz slides (Heraeus) is implanted with Si^+ ions at energies of 28, 130, 267 or 400 keV. Monte-Carlo calculations using the TRIM program [42] were performed to determine the projected range (R_p) and straggle (σ) of the Gaussian depth distribution of the implanted ions for the four implantation energies; see Table 4.1. The implanted ion fluences, also listed in Table 4.1, were chosen such that the peak Si concentration was approximately 5 at.%. After implantation, the samples were annealed for 10 minutes at 1100 ^{o}C, under an Ar flow to nucleate the nanocrystals. Subsequently, the samples were annealed for 30 minutes at 800 ^{o}C under a flow of forming gas (H_2:N_2=1:9), a process that is known to increase the luminescence yield of the Si nanocrystals, due to passivation of quench

Energy (keV)	R_p (nm)	σ (nm)	fluence (Si/cm^2)
28	44	18	$1.4 \cdot 10^{16}$
130	193	59	$3.7 \cdot 10^{16}$
267	401	99	$7.2 \cdot 10^{16}$
400	593	132	$9.3 \cdot 10^{16}$

Table 4.1: Implantation conditions for the four Si-implanted samples, the projected range (R_p) and straggle (σ) were calculated.

sites.[32] Finally, an optically thick (225 nm) Ag layer was deposited on one part of the sample using sputtering of a pure Ag target in an Ar ambient at a pressure of 5 μbar. The deposition rate was 2.5 nm/s. The dielectric constant of the Ag was measured by spectroscopic ellipsometry in the wavelength range of 300 to 1700 nm.

Photoluminescence (PL) spectroscopy was performed at room temperature using an Ar-ion laser operating in the linear pump regime at 488 nm. The laser intensity, modulated at 667 Hz with an acousto-optical modulator, was incident though the transparent back side of the sample. The PL was collected from the back using an f=10 cm lens; guided through a long-pass filter (λ >524 nm) and dispersed using a 480-mm focal-length monochromator, set to a resolution of 3 nm. A AgOCs photo multiplier recorded the collected and dispersed PL intensity. PL decay measurements were taken with a multi-channel photon counting system. The system time resolution was 100 ns. To determine the influence of the metal on the emission of the Si nanocrystals, PL spectra and decay rates were always compared for two sections of the same sample: one part covered with Ag, one part not covered.

4.3 Results and discussion

4.3.1 Quantitative analysis of stretched-exponential decay

For a quantitative comparison of Si nanocrystal PL decay rate measurements it is important to realize that the time decay of the Si nanocrystal emission at a given detection wavelength is not described by a single decay rate, but rather a distribution of decay rates.[43][44][45] This distribution reflects a variation in the Si nanocrystal emission characteristics, which is caused by several factors.

1. Identical Si nanocrystals located at different positions in their photonic environment experience a different decay rate due to the combined effect of local density of states and non-radiative processes, as will be discussed in this chapter.

2. The large linewidth of the individual Si nanocrystal emission,[46] which results from the fact that the decay is phonon assisted, leads to a distribution of decay rates at a given emission wavelength.

3. Interaction between Si nanocrystals, which can lead to quenching, is sensitive to variations in the nearest neighbor distance. The distribution of nearest-neighbor distances is determined by small-scale inhomogeneities due to the nature of the nucleation and growth process of the Si nanocrystals, and large-scale variations in Si concentration (as for the Gaussian implantation depth profiles used here).

4. Si nanocrystals with identical emission wavelengths may have slightly different geometrical shapes, and thus a different decay rate.

5. Si nanocrystals with identical emission wavelengths may have varying degrees of surface passivation and thus different non-radiative decay rates.

6. Charge trapping at defect states causes intermittent Si nanocrystal emission (blinking) and thus leads to a variation in decay rate.[34]

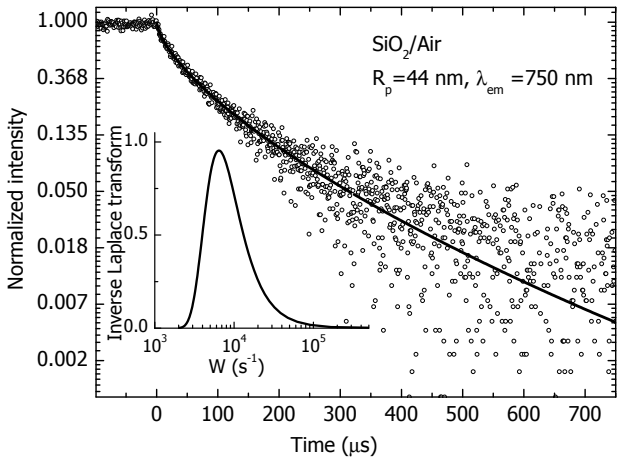

Figure 4.1: PL decay measured at λ=750 nm for the shallowest Si implant (R_p=44 nm) on a part of the sample not covered with Ag. At t=0 the laser is switched off and a stretched exponential PL decay can be observed. The solid line shows a stretched exponential fit of the data, which corresponds to the decay rate distribution shown in the inset.

As an example of the non single-exponential Si nanocrystal decay, Fig. 4.1 shows a Si nanocrystal PL decay trace measured at λ=750 nm for the 400 keV Si implant. The decay trace was fitted with a four-parameter equation for a stretched-exponential decay: $I = I_0 + I_1 \exp(-(t/\tau_{exp})^{\beta})$, with offset ($I_0$), amplitude ($I_1$), lifetime ($\tau_{exp}$), and β. An excellent agreement with the data was obtained as can be seen by the fit overlaying the data in Fig. 4.1. In the

past, several methods have been applied to determine the distribution of decay rates underlying the stretched exponential function.[47][48] Here we will use the method outlined by Lindsey and Patterson.[49] The stretched exponential decay can be described as the Laplace transform of $\rho(\tau)$, a lifetime distribution, in the following way

$$e^{-(\frac{t}{\tau_{exp}})^{\beta}} = \int_0^{\infty} e^{-\frac{t}{\tau}} \rho(\tau) d\tau \qquad . \tag{4.1}$$

Using the following substitutions: $s{=}t/\tau_{exp}$, $x{=}\tau_{exp}/\tau = W/W_{exp}$ (W the decay rate), and $\lambda(x,\beta){=}(\tau_{exp}/x^2)\rho(\tau_{exp}/x)$, the integral can be rewritten into a standard Laplace integral

$$e^{-s^{\beta}} = \int_0^{\infty} e^{-sx} \lambda(x,\beta) dx \qquad , \tag{4.2}$$

with $\lambda(x,\beta)$ the rate distribution. The function $\lambda(x,\beta)$ can be written analytically as a series solution [50]

$$\lambda(x,\beta) = -\frac{1}{\pi} \sum_{k=0}^{\infty} \frac{(-1)^k}{k!} \sin(\pi\beta k) \frac{\Gamma(\beta k+1)}{x^{\beta k+1}} \qquad , \tag{4.3}$$

with Γ the gamma function. With τ_{exp} and β obtained from the fit to the experimental data, $\lambda(x,\beta)$ was calculated over a range of x values centered at 1. The range of x values was chosen such that $\lambda(x,\beta)$ was sufficiently small for both the largest and smallest x in the domain. We choose the lower boundary x of the domain as the smallest x where convergence of Eq. 4.3 could still be reached. Outside the domain the function was assumed to be zero. The distribution $\lambda(x,\beta)$ obtained from the stretched-exponential fit of the PL decay trace in Fig. 4.1 is plotted in the inset. To verify the correctness of our procedure, the obtained distribution was then Laplace-transformed to recalculate the decay trace. Perfect agreement with the stretched-exponential decay fit was obtained (identical drawn curves in Fig. 4.1). Since the first moment of the decay rate distribution is divergent,[49] an average decay rate cannot be calculated. However, since the average lifetime $\langle\tau\rangle$ can be calculated, we approximate the average decay rate by

$$\langle W \rangle \approx \frac{1}{\langle\tau\rangle} = \frac{\beta}{\tau_{exp}} \Gamma^{-1}(\beta^{-1}) \qquad . \tag{4.4}$$

In the remainder of this chapter, the thus defined average decay rate will be used to compare the decay rates of different samples.

To further explore the relation between the parameters of the stretched exponential function and the corresponding decay-rate distribution, we examine a characteristic Si nanocrystal emission spectrum for the sample with the deepest Si implant and not covered with Ag. Figure 4.2(a) shows the Si nanocrystal PL emission spectrum for the sample implanted with 400 keV Si. At various emission wavelengths (dotted horizontal lines) the PL decay was measured and fitted using a stretched-exponential decay. The rate distributions, obtained

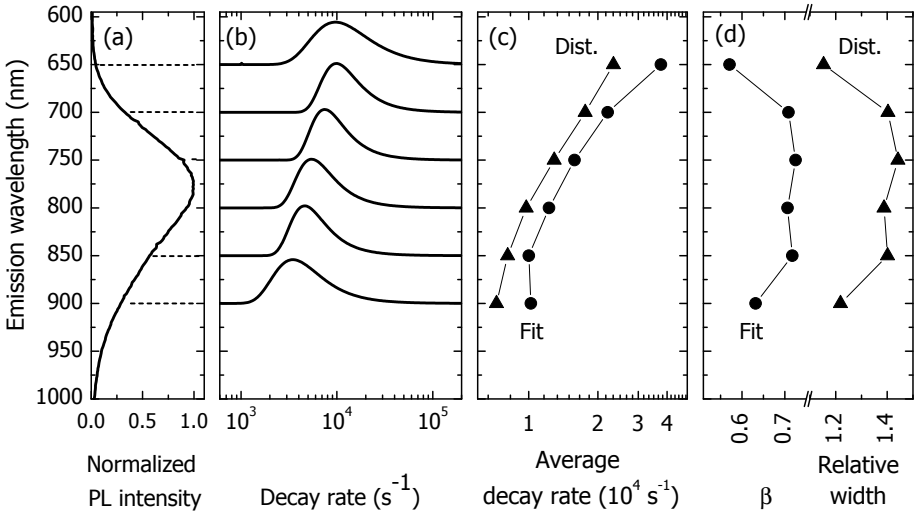

Figure 4.2: (a) PL emission spectrum for the deepest Si implant (R_p=593 nm), measured on the part of the sample not covered with Ag. (b) Decay rate distributions obtained from PL decay measurements are shifted vertically to the indicated wavelengths (dashed lines in (a)). (c) Average decay rate obtained from the decay-rate distribution (triangles) and decay rate obtained from the stretched-exponential fit (circles). (d) Inverse of the relative FWHM obtained from the decay-rate distribution (triangles) and stretched-exponential fit parameter β (circles).

from the fits, are plotted in Fig. 4.2(b) for six different emission wavelengths. The rate distributions are shifted vertically to match with the dashed lines in Fig. 4.2(a) to indicate the emission wavelengths at which the PL decay was measured. It can be clearly seen that the rate distribution shifts to lower rates as the emission wavelength increases. This is attributed to a decreasing exciton recombination probability with increasing nanocrystal size.[51] From the rate distributions two quantities were calculated: the average decay rate and the inverse of the full width at half maximum (FWHM) normalized to the average decay rate ($1/(\langle\tau\rangle$FWHM)). Figure 4.2(c) shows the average decay rates (triangles), again showing the decreasing trend with increasing emission wavelength. For comparison, the decay rates obtained from the stretched-exponential fit ($1/\tau_{exp}$) are also plotted (circles). Both parameters follow a similar trend, although at slightly different absolute values, which is due to the way the width of the distribution affects the average decay rate. The decay rates are in the range of (1-4)$\cdot 10^4$ s^{-1}, typical values for Si nanocrystals made by ion-implantation.[44][52] Figure 4.2(d) shows the inverse of the relative width of the distributions (triangles), derived from the data in Fig. 4.2(b). For comparison, β values from the corresponding stretched-exponential fit are also shown (circles). The parameter β is in the range of 0.55 to 0.7, which are typical

values for Si nanocrystals made by ion implantation.[44] Both parameters in Fig. 4.2(d) show the same trend with wavelength, reflecting that a small value of β corresponds to a large distribution width, the typical characteristic of a stretched-exponential function.

4.3.2 Optical characterization

With the decay-rate distributions determined in a systematic way, as in Fig. 4.2, we can study the influence of the Ag layer on the PL emission and decay of Si nanocrystals in SiO_2. Figure 4.3 shows the normalized PL spectra for the samples with Si nanocrystals located at four different depths from the interface for the sample in air (a) and covered with Ag (b). The spectra are shifted vertically to facilitate their comparison. The emission spectra are typical of quantum-confined emission from Si nanocrystals. For large implantation depths the emission peaks at 775 nm (1.6 eV), which corresponds to a Si nanocrystal diameter of 3.8 nm.[53] The width of the emission spectrum is 290 meV (FWHM). Measurements on single Si nanocrystals show a linewidth of 120-210 meV,[46] implying that the observed linewidth is due to both the intrinsic Si nanocrystal emission spectrum width and inhomogenous effects. While the spectra for the three deepest implants peak at a similar wavelength, the spectrum from the Si nanocrystals closest to the interface is significantly blue shifted. We attribute this shift, which reflects a smaller Si nanocrystal size, to a different Si nanocrystal nucleation and growth mechanism caused by the small width of the distribution or the proximity of the interface, which may lead to a different nanocrystal size distribution and/or a different nanocrystal non-radiative decay rate. PL spectra for the sample covered with Ag (Fig. 4.3(b)) show the same trend as for the sample in air, with a blue shift observed for the shallowest Si implant.

Figure 4.4 shows the decay rate distributions for the four samples with different Si implantation depths. The rate distributions are calculated from the PL decay traces measured at a PL emission wavelength of 750 nm, both for the sample in air (a) and covered with Ag (b). The arrows indicate the average decay rates determined as described in Section 4.3.1. For the air-covered sections of the sample, the decay rate distributions have an average of (1.2-1.4)$\cdot 10^4$ s^{-1}, and show no dependence on the depth. The same samples covered with Ag show a similar average decay rate for the three deepest Si implantations. However, for the shallowest Si implant the average decay rate near the Ag film is significantly larger ($2.2 \cdot 10^4$ s^{-1}). Note that on the logarithmic scale in Fig. 4.4 the effect of the Ag layer may appear relatively small, but with the analysis introduced above we can now clearly conclude that that the presence of the Ag enhances the average PL decay rate of Si nanocrystals for the shallowest implant. For this sample the decay rate increases from $(1.25 \pm 0.05) \cdot 10^4$ s^{-1} for the air-covered section to $(2.2 \pm 0.2) \cdot 10^4$ s^{-1} for the Ag-covered section, an enhancement by a factor 1.8 ± 0.2. It is also clear from Fig. 4.4(b) that for the shallowest Si implant the presence of Ag increases the width of the decay rate distribution.

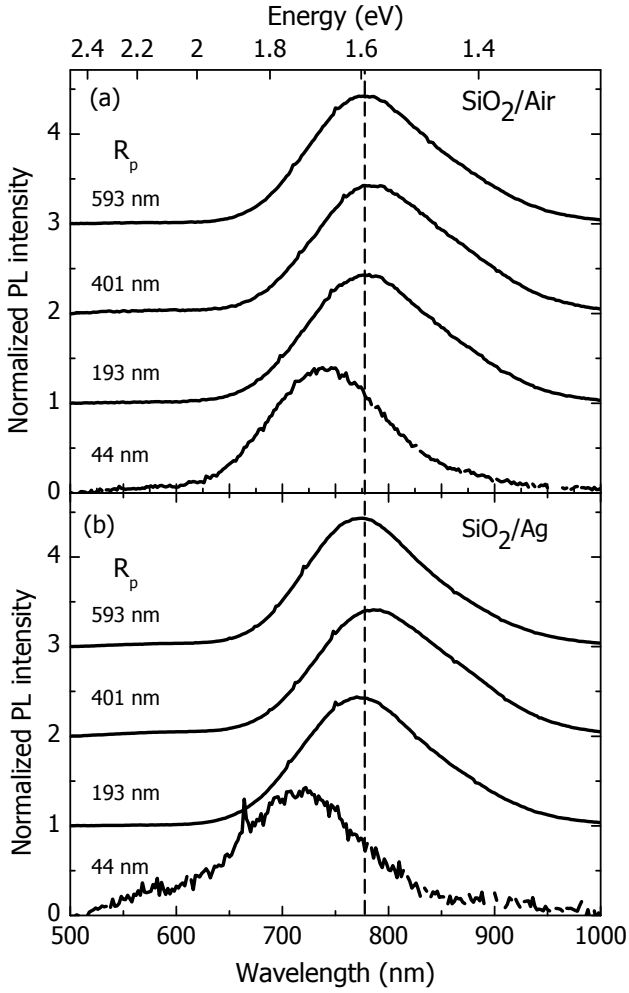

Figure 4.3: Normalized Si nanocrystal emission spectra measured on the four Si implanted samples either in air (a) or covered with Ag (b). Spectra are shifted vertically for clarity. The peak depths (R_p) of the four Si-implants are indicated. In all samples Si nanocrystals are excited with λ=488 nm laser light.

4.3.3 Modelling the Si nanocrystal decay

The decay rate of an oscillating dipole in a (metallo-) dielectric environment can be calculated using a classical model as developed by Ford and Weber.[6] In brief, the model calculates the decay rate of a dipole by determining the electric field at its position. The total field at the position of the dipole is the result of the dipolar field and the fields reflected from the dielectric surrounding

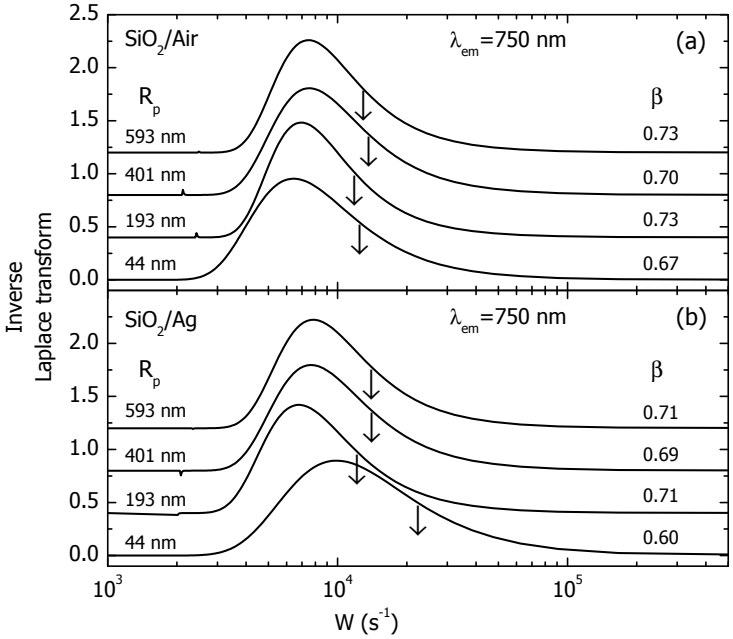

Figure 4.4: PL decay rate distributions obtained from stretched-exponential PL decay traces measured at λ=750 nm for the four Si implants (depths R_p indicated). Data are shown for the sample in air (a) and covered with Ag (b) and are shifted vertically for clarity. Vertical arrows indicate the average decay rate, and the β parameters of the corresponding stretched-exponential fit are also indicated. For the Si nanocrystal distribution closest to the Ag interface the decay rate is significantly increased.

of the dipole. To calculate these fields, the dipolar electric field is Fourier transformed into its spatial wavevector components. The field at the position of the dipole, resulting from reflections at the interfaces, is then calculated for each wavevector using the Fresnel reflection and transmission coefficients of the interfaces, which are determined using the dielectric constants as input parameters. After integration over the out-of-plane wavevectors the electric field at the position of the dipole is a function of normalized in-plane wavevector only ($k_{||}/k_d$, with k_d the wavevector of a plane wave in the dielectric). By taking the imaginary part of the product of the electric field at the position of the dipole and the dipole moment (see Eq. 1.2), the power dissipation can be calculated at any normalized in-plane wavevector. Integrating the power dissipation over all in-plane wavevectors divided by the photon energy $\hbar\omega$ then yields the total decay rate of the dipole. In this analysis the parallel and perpendicular dipole orientations relative to the interface are treated separately. They are averaged to obtain the decay rate for a randomly oriented dipole, as is the case in the amorphous SiO_2 host.

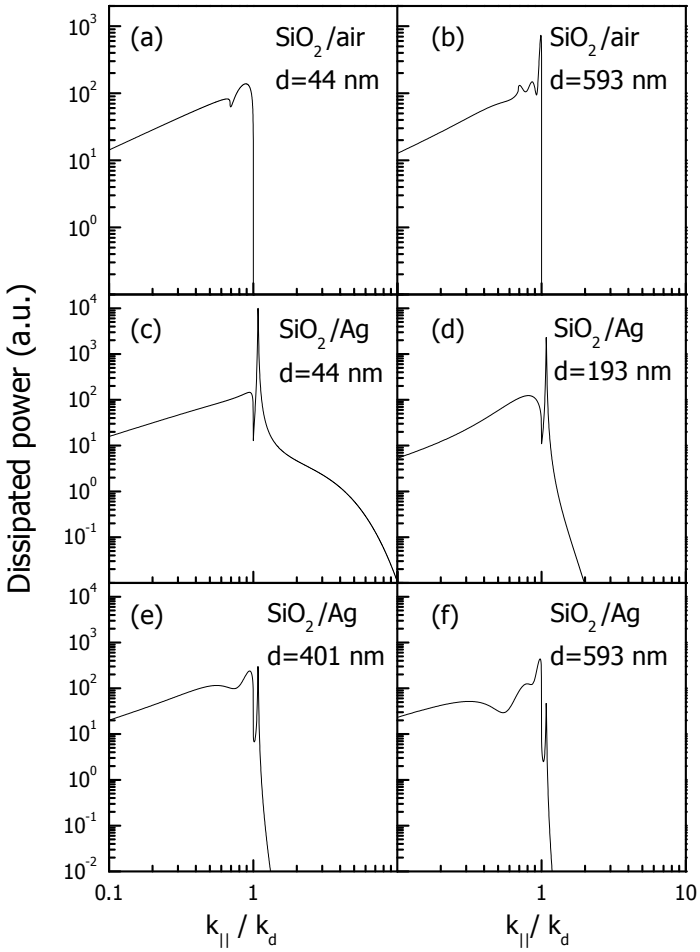

Figure 4.5: Power dissipation as a function of in-plane wavevector for a randomly oriented dipole located near a SiO_2/air interface, emitting at λ=750 nm, for a distance of 44 nm (a) and 593 nm (b) to the interface. (c)-(f) The same calculation, but for a SiO_2/Ag interface and distances of 44, 193, 401, and 593 nm to the interface. The wavevector region $k_{||}/k_d \leq 1$ corresponds to spontaneous emission, $1 < k_{||}/k_d \leq 1.158$ to SP excitation and $k_{||}/k_d > 1.158$ to lossy surface wave excitation.

In our analysis we use the dielectric constants of silver ($\epsilon_{Ag}=\epsilon'_{Ag}+i\epsilon''_{Ag}=$ -15+i0.86) and SiO_2 (ϵ_{SiO_2}=2.1) at λ=750 nm to calculate the power dissipation of a randomly oriented dipole as a function of normalized in-plane wavevector for a given distance from the interface. Figure 4.5(a) shows the result for a dipole at 44 nm from an SiO_2/air interface. This distance corresponds to the peak position of the shallowest Si implant. Power is dissipated for $k_{||}/k_d \leq 1$ corresponding to spontaneous emission in the SiO_2 and air regions.

The small dip at $k_{||}/k_d \sim 0.69$ is due to the difference in power dissipation for wavevectors in air and SiO_2. Figure 4.5(b) shows a similar calculation, but now for a dipole at 593 nm from the interface. Due to the larger distance interference wiggle are observed that are due to constructive or destructive interference of the reflected dipolar field, which either increases of decreases the dipoles power dissipation for a particular wavevector. The total power dissipation for the two depths, i.e. the integral over the power dissipation spectra in Fig. 4.5(a) and (b), is nearly identical. This is due to the relatively small reflection at the SiO_2/air interface. Figure 4.5(c) shows a similar calculation as for Fig. 4.5(a) (dipole located at 44 nm), but for the SiO_2/Ag interface. Again, power is dissipated for $k_{||}/k_d \leq 1$, corresponding to spontaneous emission into the far field. However, in contrast to the case for the SiO_2/air interface, power is also dissipated for larger wavevectors ($k_{||}/k_d > 1$). First, a power dissipation resonance is observed for $k_{||}/k_d = 1.078$. This wavevector ratio corresponds to: $\sqrt{\epsilon'_{Ag}/(\epsilon'_{Ag} + \epsilon_{SiO_2})}$, which is the wavevector for a SP propagating along the SiO_2/Ag interface, normalized to the wavevector for a plane wave in SiO_2. The width of the resonance is determined by dissipation in the metal (represented by ϵ''_{Ag}, the imaginary part of the dielectric constant for Ag), which is relatively small at this wavelength ($1/e$ SP intensity propagation length is ~ 8 μm). A considerable amount of power is contained in the SP resonance (note the log scale). At larger wavevectors power is dissipated to lossy surface waves [6]: loss processes such as electron-hole excitation and electron scattering in the Ag. Similar calculations are performed for dipoles spaced 193, 401, and 593 nm from the SiO_2/Ag interface, and are shown in Fig. 4.5(d)-(f). The calculations show that the excitation rate of lossy surface waves decreases very rapidly as the distance increases. Also the excitation rate of SPs decreases, although less rapidly. Indeed, SP excitation is a near-field effect that, for optical wavelengths, is know to occur for distances up to $\sim$100 nm, while the dissipation into lossy surface waves typically occurs on a 10 nm length scale. Note that the wiggles observed for $k_{||}/k_d \leq 1$ are more pronounced in the Ag-covered sample than for the sample in air (Fig. 4.5(a) and (b)), due to the larger reflectivity of the interface. The minima and maxima occur at different wavevectors than for the SiO_2/air interface, owing to the different phase shifts that occurs upon reflection from either the SiO_2/Ag or the SiO_2/air interface.

Since the various ranges of normalized in-plane wavevector in Fig. 4.5 represent different decay channels, the power dissipated into these channels can be obtained by integration over the corresponding wavevector range: spontaneous emission: $k_{||}/k_d < 1$, SP excitation: $1 \leq k_{||}/k_d < 2k_{SP}\text{-}1 = 1.158$,[28] and lossy surface wave excitation: $k_{||}/k_d \geq 1.158$. The result of this integration procedure is shown in Fig. 4.6, for a range of dipole distances from the interface. Figure 4.6(a) shows the distance dependent decay rate for a dipole near the SiO_2/air interface. The rate is normalized to unity for large distances from the interface. As can be seen, close to the interface the normalized decay rate is significantly lower than for a dipole in the bulk of the material. The decay rate shows oscillating behavior as a function of distance, due to the interference of

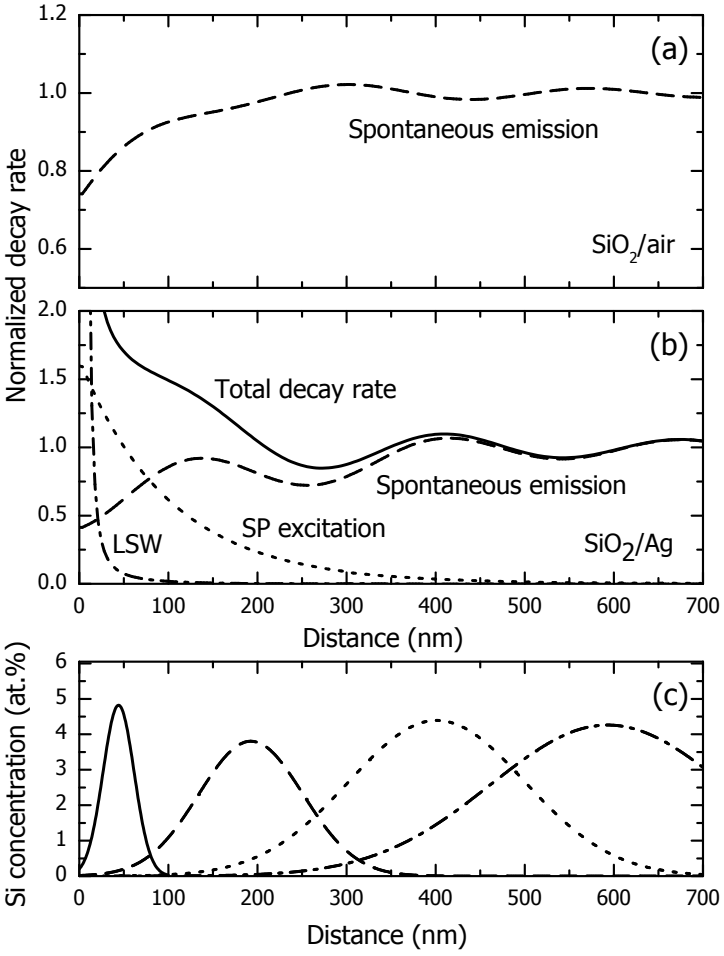

Figure 4.6: Normalized decay rate as a function of distance from a SiO_2/air interface (a) and a SiO_2/Ag interface (b). For the SiO_2/Ag interface the total decay rate is divided into its three constituent parts: spontaneous emission, SP excitation and lossy surface wave (LSW) excitation. In (c) the Si depth distributions are plotted for the four implants.

reflected waves with the direct dipole field that either increases or decreases the dipole's dissipation rate. A similar effect was reported earlier in References [4] and [5], for the case of 1.5 μm emission of Er^{3+} ions near a SiO_2/air interface. Figure 4.6(b) shows the calculated decay rates for the dipole in proximity to the SiO_2/Ag interface. The contributions of spontaneous emission, SP excitation, and lossy surface wave excitation are plotted separately; the total decay rate is also shown. The spontaneous emission rate shows oscillating behavior, but when compared to the data in Fig. 4.6(a), with larger modulation depth, due to the larger reflectivity at the interface. Again the maxima and minima occur

at different depths for the SiO_2/Ag interface than for the SiO_2/air interface, due to a different phase change upon reflection at the SiO_2/Ag interface. The SP excitation rate decreases exponentially as a function of distance as would be expected from the exponentially decreasing field amplitude of the SP in the dielectric.[6] Lossy surface wave excitation occurs only at very short distances (d<50 nm) from the interface and shows a d^{-3} dependence. This is in agreement with the distance dependence expected for an r^{-6} dipole-dipole interaction, integrated over a planar sheet of dipoles.

To compare the various decay processes for the different Si implants, the depth profiles for the four Si implants are shown in Fig. 4.6(c). It is clear that for the three deepest Si implants the decay is dominated by spontaneous emission. The normalized decay rates for the SiO_2/air and SiO_2/Ag interface integrated over the depth distributions for these implants are close to unity. Indeed, these samples with and without Ag show similar PL decay rates, as can be seen in Fig. 4.4(a) and (b). Next, we analyze the decay for the shallowest Si implant that peaks at 44 nm. At the peak the normalized decay rates are 0.848 ± 0.002 and 1.75 ± 0.08 for the SiO_2/air and SiO_2/Ag interface, respectively. The error bars are calculated with the straggle of the Si distribution and assuming a symmetric spread of Si nanocrystals around the center of the distribution.[54] The decay rate enhancement by the Ag is a factor 2.1 ± 0.1, and is for the most part due to the additional SP decay channel (60 % of the total decay rate). Experimentally, the decay rate enhancement derived in Section 4.3.2 is 1.8 ± 0.2. Thus, within the error bars good agreement between experiment and theory is observed.

The above analysis assumes that non-radiative decay processes do not occur in Si nanocrystals. Including such an effect by the addition to the model of a non-radiative decay rate (W_{nr}), which is not influenced by the presence of the Ag, would bias the calculated decay rate ratio for the SiO_2/air and SiO_2/Ag towards unity. Taking into account the error bars in measurement and calculation, agreement between experimental and calculated decay rate ratios is achieved when a small ($W_{nr}=(3 \pm 2)\cdot 10^3$ s^{-1}) non-radiative decay rate is included. Combining the measured total decay rate (radiative rate W_{rad} plus W_{nr}) and the calculated non-radiative decay rate then leads to an internal QE (QE=$W_{rad}/(W_{rad} + W_{nr})$) of Si nanocrystal emitting at λ=750 nm of 77 ± 17 %. This is the first direct determination of this quantity.[46] In our analysis, the change in refractive index by the excess Si implanted into the glass is not taken into account. A multilayer refractive index model based on Maxwell-Garnett effective medium theory showed that this has a relatively small effect on the calculated QE ($\sim$5 %).

Finally, we discuss the large difference in β for the two interfaces, observed in Fig. 4.4 for the shallowest Si implant. Figure 4.6 shows that for the shallowest Si implant the decay rates for the SiO_2/Ag interface depend stronger on the depth than for the SiO_2/air interface: the rate/depth derivatives of the total decay rates differ by a factor five at the Si peak position. This leads to a larger spread of Si nanocrystal decay rates for the SiO_2/Ag interface, and consequently a lower β, as is observed.

4.4 Discussion

The presented results show that optically active Si nanocrystals can efficiently excite SPs on a SiO_2/Ag interface. For most optimal excitation of SPs the Si nanocrystals should be located at ∼40 nm from the SiO_2/Ag interface, where SP coupling is strong and loss processes are relatively small. Coupling to SPs provides a unique way to enhance the effective emission rate and QE of Si nanocrystals. By first exciting SPs at a rate W_{SP} and then coupling the SPs out into the far field, the SP excitation, that initially constitutes a loss process, is turned into a radiative process. In this way the radiative decay rate W_{rad} can be artificially enhanced to W_{rad} plus W_{SP}. Similarly, for Si nanocrystals with internal QE<1, coupling to SPs and subsequent out coupling to the far field, can enhance the internal QE. A significant enhancement is expected when the out-coupling efficiencies are large and if $W_{SP}>W_{nr}$. Optimized geometries have shown out-coupling efficiencies close to unity.[20]

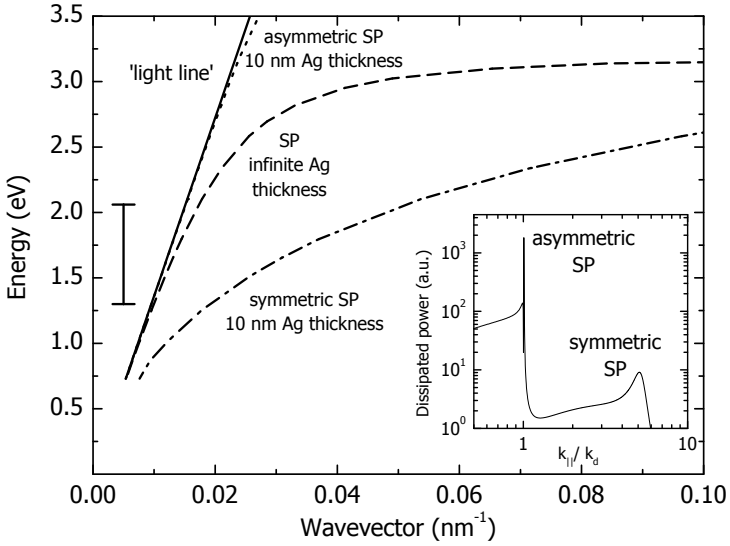

Figure 4.7: Dispersion curves for: plane wave (solid line), SP for an infinite Ag thickness (dashed). For a 10 nm thick Ag film embedded in SiO_2 the SP splits into an asymmetric (dotted line) and symmetric mode (dashed-dotted). The vertical bar indicates the Si nanocrystal emission bandwidth. Inset shows the power dissipation for a randomly oriented dipole embedded in SiO_2, emitting at 480 nm at a distance of 44 nm from the Ag film. Two peaks can be observed: the asymmetric mode at $k_{||}/k_d$=1.008 and the symmetric mode at $k_{||}/k_d$=5.09. Indicated by the vertical bar is the emission energy range of Si nanocrystals.

In the present experiment the SP coupling rate is similar to the spontaneous emission rate, limiting the maximum achievable increase in emission rate and QE. Here we discuss different ways to increase the SP excitation

rate. The largest coupling of a dipole to SPs is achieved when the emission frequency matches the SP resonance frequency, i.e. the frequency for which ϵ'_{metal}=-ϵ_d. In the present case, for an emission wavelength of 750 nm, the large discrepancy between the dielectric constant of the SiO_2 (ϵ_{SiO_2}=2.1) and the Ag (ϵ_{Ag}=-15+i0.86), results in a relatively small SP excitation rate. Using an alternative host for Si nanocrystals that has a higher dielectric constant will increase the coupling. For example, for a dipole at 44 nm from the interface, emitting at 750 nm with Ag as a metal and Si_3N_4 (ϵ=4) as a dielectric matrix, 63 % of the dipole's excitation energy is converted into SPs.

The SP coupling rate can be further enhanced by modifying the SP dispersion relation by changing the thickness of the metal. For a metal layer with a thickness of the same order as the skin depth, SPs propagating at both sides of the metal interact. This results in a splitting of the single SP mode into an asymmetric and symmetric mode.[55] We determined the thin metal film SP dispersion using Ford and Weber's model. Calculations are performed for a multilayer structure with SiO_2 on top of a 10 nm thick Ag layer on top of a SiO_2 substrate, with the dipole at 44 nm distance from the Ag layer. The inset in Fig. 4.7 shows the power dissipation, calculated for a randomly oriented dipole emitting at a wavelength of 480 nm. Clearly two SP modes exist: the asymmetric SP mode at $k_{||}/k_d$=1.0083, and the symmetric SP mode at $k_{||}/k_d$=5.08. Similar calculations were performed over a large range of frequencies (taking the dispersion of ϵ_{Ag} into account) and at each frequency the wavevectors of both SP modes were derived. The result is shown in Fig. 4.7, with the dispersion of a plane wave $\omega = kc/\sqrt{\epsilon_d}$ shown for reference ('light line'). From these data we can observe that, in comparison to the infinite Ag layer, at a given frequency the wavevector for the symmetric SP mode is increased and the wavevector for the asymmetric SP mode is decreased. Since the SP mode density is proportional to $d(k^2)/d\omega$,[56] decreasing the film thickness increases the SP mode density for the symmetric SP mode. For the case calculated in Fig. 4.7 this leads to a ten-fold increase in the SP excitation rate. A full calculation of the thin-film SP excitation rate should also take into account the mode overlap of the SP field and the dipole.

The present work shows that SP modes can be selectively excited by a strongly coupled dipole, with the symmetric mode being more pronounced for thin films compared to the asymmetric mode. Further work will address this in more detail. Given the fact that Si nanocrystals can be electrically excited,[33][34] coupling to SPs provides a new way to electrically generate SPs. Note that in the above analysis we have not extracted SP propagation losses from the calculations. Typically, for conditions of enhanced coupling, propagation losses increase. However, by incorporating Si nanocrystals into a well-engineered grating that enhances the re-radiation and thus requires less propagation length, efficient out coupling of SPs into the far field may be possible. If the generation of SPs itself is the goal, then a tapered waveguide can be used to efficiently excite lossy SPs, which then can be adiabatically transferred to a low-loss long-range propagating SP.

4.5 Conclusions

In summary, we have shown that the average photoluminescence decay rate of Si nanocrystals can be significantly enhanced when they are in close proximity ($\sim$50 nm) to a Ag interface. Calculations performed with a classical dipole oscillator model are in good agreement with the data and show that the increase in decay rate is mainly due to excitation of SPs at the SiO_2/Ag interface. By comparing the observed changes in decay rate at the SiO_2/air and SiO_2/Ag interfaces to the calculations, a Si nanocrystal internal quantum efficiency of (77 $\pm$ 17) % was found. From the model, the dispersion relation of thin-film SPs is derived, and it is shown that for thin metal films the symmetric SP mode is preferentially excited. As Si nanocrystals can be electrically excited, this work provides design criteria for an electrically pumped, mode selective, SP source.

Chapter 5

Applications of surface plasmons

This chapter shows several possible applications of surface plasmons (SPs) in microscale and nanoscale photonic circuits. They are based on materials compatible with standard Si microchip manufacturing, and thus could be incorporated and combined with electrical microstructures on a Si chip. The dielectric constants of materials such as SiO_2, Si and Ag were determined and used as input for the calculation of the dispersion of SPs and their propagation length. Using a classical dipole oscillator model we calculate the effect of a metal/dielectric interface on the decay rate of optical emitters both in the visible and near-infrared part of the electromagnetic spectrum. From these calculations, strategies for using SPs to enhance the emission rate and quantum efficiency of light emitting diodes are derived. An outlook will be given on the possible applications of SPs in optical interconnects, light-emitting diodes, and optical switches.

5.1 Introduction

Surface plasmons propagating on planar metallic structures offer the possibility of two-dimensional optics [18] with a large integration density. Metal deposition and structuring techniques are all compatible with Si integrated circuit manufacturing technology, so that SP optics may be integrated with electronic functions on a single chip. In Section 5.2 of this chapter we derive the dispersion relation for SPs and calculate characteristic propagation lengths as a function of SP frequency. We differentiate between SPs with frequencies corresponding to free space wavelengths in the visible that have well-confined modes and large optical losses, and SPs with frequencies corresponding to near-infrared wavelengths, that are less confined and consequently show longer propagation lengths. In the near-infrared we will focus on plasmon photonics at 1.5 μm, the standard telecommunications wavelength.

Due to the different dispersion of SPs and plane electromagnetic (EM) waves, they cannot be directly converted from one to another. In Chapters 2, 3, and 4 we demonstrated how SPs can be efficiently excited through a near-field interaction. In Section 5.4.1 we present several ways to increase the coupling strength by proper materials engineering. In the subsequent section we then propose a novel optical interconnect scheme based on SPs, a method to enhance the emission rate and efficiency of light-emitting diodes (LEDs), and a SP based optical switch.

5.2 Surface plasmon dispersion and propagation on Ag

SP dispersion calculations are presented for Ag films on various substrates. The dielectric constants were measured with a variable-angle spectroscopic ellipsometer using the materials used in the actual experiments: Herasil fused silica (SiO_2) substrates, and sputter deposited Ag films (see also Chapter 2). The dielectric constants of the SiO_2 were determined by fitting the reflectivity of the SiO_2 to a model based on the dielectric constant of the glass, which is described by a Cauchy function. For the Ag film the two spectroscopic parameters Δ and Ψ were measured at various incident angles. A simultaneous fit to the data taken at three different angles resulted in an accurate determination of the dielectric constants in the wavelength range of 300-1700 nm. Figure 5.1 shows the obtained dielectric constants of SiO_2 and Ag. Data for Si are taken from Ref. [57], are also shown. For Ag, the real (ϵ'_{Ag}) and imaginary part (ϵ''_{Ag}) of the dielectric constant are plotted. For SiO_2 and Si minus the real part of the dielectric constant is plotted.

The measured dielectric constants of Ag in Fig. 5.1 are compared with those derived from a Drude model

$$\epsilon_{Ag} = \epsilon'_{Ag} + i\epsilon''_{Ag} = 1 - \frac{\omega_p^2}{\omega\left(\omega + i\gamma\right)} \quad . \tag{5.1}$$

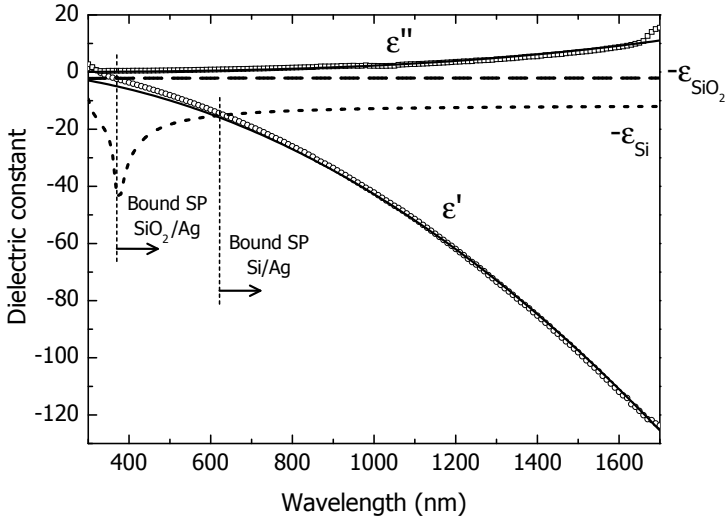

Figure 5.1: Data points show real and imaginary part of the dielectric constant of Ag. The solid lines shows the Drude fit of Eq. 5.1 to the data. The dashed line and dotted lines show minus the dielectric constant of SiO_2 and Si, respectively. The vertical dotted lines shows the cut-off wavelength of bound SPs for an SiO_2/Ag and Si/Ag interface.

with ω the optical frequency, ω_p the plasmon frequency, and γ the electron collision rate. The Drude model was sequentially fitted to the real and imaginary part of the dielectric constant of Ag (see solid lines in Fig. 5.1), resulting in a plasma wavelength of 151 nm, and a lifetime of 64 fs. The corresponding resistivity of $1.1{\cdot}10^{-8}$ Ωm, is in fair agreement with literature values.[58] At near-infrared wavelengths the fit represents the measured data accurately. In this frequency range the Ag behaves more like a pure Drude metal as no bound electron states contribute to the dielectric constant. For wavelengths lower than 500 nm the fit deviates from the data, which is attributed to interband transitions of Ag d-electrons that are not taken into account in the Drude model. The experimentally obtained dielectric constants in Fig. 5.1 were used in all calculations presented in this chapter.

The SP dispersion relation can be derived by inserting a function describing a TM-polarized EM wave into the wave equation for two adjacent media.[12] Solving the wave equation for the two media, requires continuity of the **E** field parallel to the interface. This then results in the SP dispersion relation for the wave in the propagation direction [12]

$$k_x = \frac{\omega}{c}\sqrt{\frac{\epsilon_m \epsilon_d}{\epsilon_m + \epsilon_d}} \qquad , \tag{5.2}$$

with ϵ_m and ϵ_d the dielectric constants of both media at the interface. The

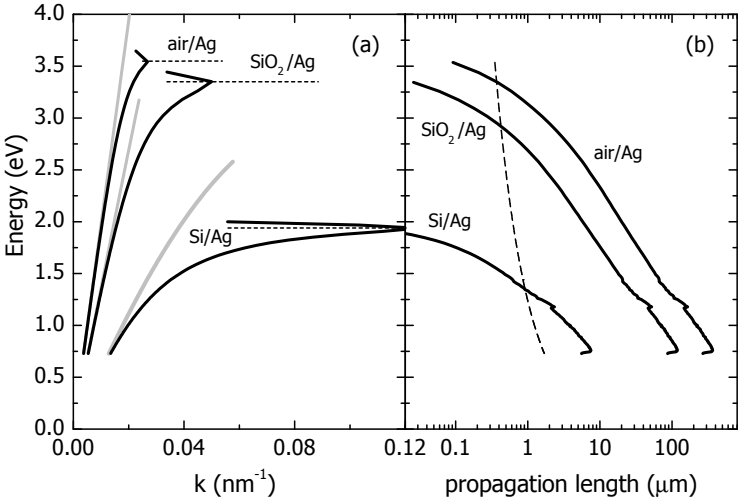

Figure 5.2: (a) Surface plasmon dispersion calculated for three interfaces (solid lines): air/Ag, SiO_2/Ag, and Si/Ag. The horizontal dotted lines show the SP cut-off energy. Dispersion relation for the corresponding plane waves in the dielectric ('light lines') are indicated in gray. (b) SP propagation lengths calculated for the three interfaces presented in (a). The dotted line shows the free space wavelength associated with the energy indicated on the vertical axis.

wavevector in the direction perpendicular to the interface is given by

$$k_z = \frac{\omega}{c}\sqrt{\frac{\epsilon_{m,d}^2}{\epsilon_m + \epsilon_d}} \qquad . \tag{5.3}$$

Consequently, if we have materials with opposite dielectric constant (such as a metal and a dielectric in the visible/infrared) and $|\epsilon_m| > \epsilon_d$ the wavevector defined in Eq. 5.3 is fully imaginary and the fields in both media decay exponentially in the direction perpendicular to the interface; the mode is bounded to the interface. The wavelength ranges corresponding to these bound surface waves are indicated by the dashed vertical lines in Fig. 5.1 for a SiO_2/Ag and a Si/Ag interface.

Using Eq. 5.2, and given the known relation between ϵ and free space wavelength (Fig. 5.1) the SP dispersion relation can be calculated. Results are shown in Fig. 5.2 for a Ag film in contact with air, SiO_2, and Si. Note that both metal and dielectric are assumed to be of semi-infinite thickness. Figure 5.2(a) shows the real part of k_x for the three dielectrics. The light lines, i.e. the dispersion in the bulk dielectrics, are indicated in gray for reference. At low energies (near-infrared wavelengths) the SP dispersion is linear, and wavevector and group velocity ($d\omega/dk$) are almost equal to that of a plane-wave in the dielectric. In this energy range only a small fraction of the EM

field is in the metal, and the interaction between the electron plasma and the EM wave is limited. Consequently, losses due to absorption in the metal are very small and the SP wave behaves like a plane EM wave; the SP is photonic in behavior. For higher energies (visible wavelengths) the EM field is more evenly located in the metal and the dielectric, and, concomitant with the increase of the SP wavevector, absorption losses are increased and the group velocity is decreased. The SP is polaritonic: it has both a photonic and plasmonic character. When the energy becomes equal to the SP resonance energy (the dotted horizontal lines in Fig. 5.2(a) indicating the energy where $\epsilon_{Ag}=-\epsilon_d$ in Fig. 5.1) the group velocity becomes low and the EM wave becomes more like a standing wave charge oscillation: the EM wave is plasmonic in nature. Note that close to this resonance, the SP wavevector increases, and thus the SP wavelength decreases. The maximum SP wavevector that can be achieved is determined by the damping of the Ag (i.e. ϵ''_{Ag}) and can be read from Fig. 5.2(a) at the resonance energy. For a Si/Ag interface the maximum SP wavevector occurs at an energy of 1.94 eV (free space wavelength 640 nm), the corresponding SP wavelength is only 50 nm. These short SP wavelengths enable a large range of applications including nanoscale photonic integrated circuits, nano lithography, etc. For higher energies the SP is no longer bound.[55]

The imaginary part of k_x (Eq. 5.2) describes SP damping. The characteristic 1/e SP propagation length can be calculated from the intensity attenuation coefficient $(2k''_x)^{-1}$, and the result is shown in Fig. 5.2(b). As can be seen, at near-infrared energies (<1 eV) SPs can have very large propagation lengths: for the Ag/Si interface extending to over 10 μm, and for the Ag/air interface extending to over 100 μm. Such long propagation lengths enable a broad range of applications in micro-photonic or opto-electronic integrated circuits.[59] On the high energy side, Fig. 5.2(b) shows much shorter propagation lengths, with the largest damping observed for the Si. This reflects the larger concentration of the SP field inside the metal at these energies. The dotted line shows the free space wavelength corresponding to the SP energy. For data points on the left of this line, the propagation length is smaller than the vacuum wavelength, indicating the standing wave character of these SPs.

5.3 Electrically excitable surface plasmon sources

The dispersion graphs in Fig. 5.2(a) show that there is a significant mismatch in wavevector between SPs and the wavevector of their unbounded counterparts, in particular close to the SP resonance. It is thus not possible to excite SPs directly from the far-field. One solution to this problem that we have addressed in the previous chapters is to use near-field excitation of SPs using a dipole source. The near-field of a dipole is represented by a large wavevector spectrum and can thus lead to the generation of SPs. When these dipoles can be excited electrically, an electrically excitable SP source can thus be made. Here

we calculate the efficiency of such a source in two wavelength ranges. First we address the coupling between Er ions and SPs in the near-infrared (see Chapters 2 and 3), where SPs have long propagation lengths (see Fig. 5.2(b)). As Er-doped LEDs have been demonstrated,[60][61] integration of these devices with metallic films would enable the electrical generation of long-range SPs. Second, we consider Si nanocrystals as a source of SPs (see Chapter 4). Si-nanocrystal-based LEDs emitting in a broad spectral range between 600-900 nm (depending on nanocrystal size) have been demonstrated recently.[34] While SPs excited at these wavelengths have larger losses, their excitation efficiency is larger than in the near-infrared as the dipole emission energy is closer to the SP resonance.

5.3.1 Electrically excitable Er-doped Si surface plasmon source on Ag

We use the classical dipole oscillator model also presented in Chapter 3 and Chapter 4 to calculate the coupling between Er ions in Si and SPs on a Si/Ag interface. Figure 5.3 shows the spontaneous emission rate, the SP excitation rate and the lossy surface wave excitation rate as a function of distance of a randomly oriented dipole emitting at a wavelength of 1535 nm embedded in Si ($\epsilon_{Si} = 11.9$). The solid line in Fig. 5.3 shows the coupling rate to SPs, relative to the total decay rate; it shows that ideally Er ions must be located some 30 nm away from the interface to achieve most efficient SP excitation. At smaller distances from the interface the excitation of lossy surface waves is increased, which causes a reduction of the fraction of the decay coupled to SPs. At larger distances from the interface the SP excitation efficiency is very much decreased due to a decreased overlap of the SP field and the dipole field. As Fig. 5.3 shows, at this optimum distance 60 % of the dipole's excitation energy can be transferred to SPs. Given the fact the Er-doped Si LEDs have been demonstrated with external emission quantum efficiencies (QEs) at room temperature of typically 10^{-3},[60] electrically excited surface plasmon sources at λ=1535 nm with 10^{-3} efficiency are feasible. Most recently, it was demonstrated that silicon-rich oxide, with Si nanocrystals embedded in an oxide matrix, is a better host for Er than bulk Si.[62] In this material, temperature quenching due to phonon-assisted energy backtransfer [22] (the main quenching mechanisms in Er-doped bulk Si) does not occur, and room temperature LEDs based on Er-doped silicon-rich oxide with an external emission QE as high as 10 % have been demonstrated. While silicon-rich oxide has a lower refractive index than bulk Si, and thus a somewhat smaller SP coupling efficiency, this material seems the best candidate as host material of an electrically excitable Er-doped SP source.

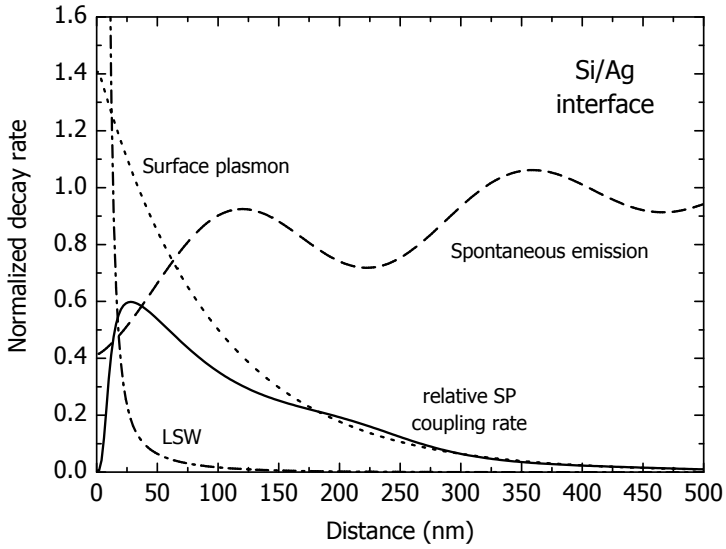

Figure 5.3: Normalized decay rate as a function of distance to the Ag interface for a dipole in Si emitting at 1535 nm. The decay rate is partitioned in spontaneous emission (dashed line), SP excitation (dotted line), and lossy surface wave excitation (dashed-dotted line). The fraction of decay coupled to SPs (solid line) peaks at ∼30 nm from the interface.

5.3.2 Electrically excitable Si-nanocrystal-based surface plasmon source on Ag

Coupling to SPs also can be used to to enhance the emission rate of SP-coupled LEDs, and thus increase the modulation rate of these devices. To achieve this, the SP coupling rate should be increased well above the radiative decay rate. This can be achieved by bringing the dipole emission energy and SP resonance energy closer. Figure 5.4 shows a calculation of the total decay rate for dipoles embedded in SiO_2, as a function of distance to the SiO_2/Ag interface, normalized to the emission wavelength. Calculations are shown for emission wavelengths of 380, 450, 700, 1400 nm. Clearly, large decay rate enhancements, both due to SP coupling and lossy surface wave excitation, are predicted for wavelengths close to the SP resonance that occurs at 360 nm for the SiO_2/Ag interface (see Fig. 5.1). Silicon nanocrystals show emission in the 600-900 nm band, which can be tuned by varying the size. Si nanocrystal electroluminescence has been observed at these wavelengths.[34] To achieve the large decay rate enhancements shown in Fig. 5.4 also for this wavelength range, the SP resonance must be further red shifted (e.g. by using a higher-index Si nanocrystal host or a thin metal film).

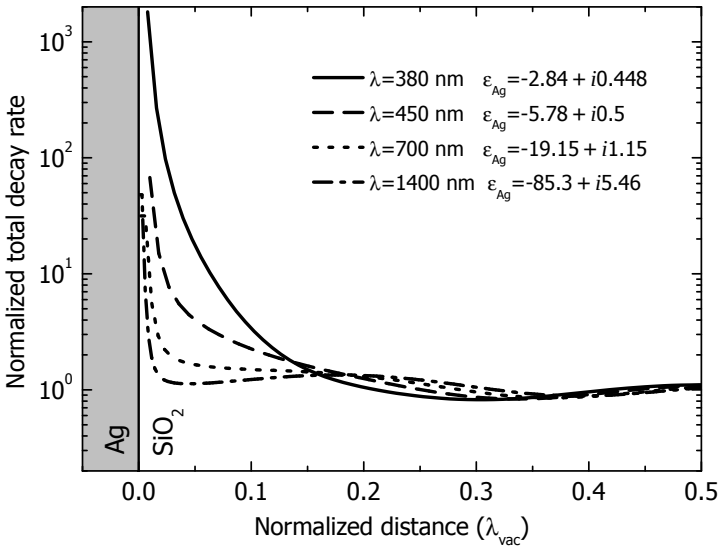

Figure 5.4: Total decay rate of dipoles in SiO_2 as a function of distance to the Ag interface, normalized to the emission wavelength, calculated for various emission wavelengths (indicated). The Ag dielectric constant is indicated at each wavelength.

5.4 Surface-plasmon-based photonic devices

5.4.1 Surface-plasmon-based optical interconnect

Using the design for an electrically excitable SP source given in Section 5.3.1, and the dispersion and propagation length calculations in Section 5.2, it becomes possible to design a prototype SP optical interconnect, in which information can be generated, transported and detected in the form of SPs. A possible design schematic for such a device is shown in Fig. 5.5. A Ag/Si:Er SP source is integrated with an optically thick Ag SP waveguide. To keep propagation losses to a minimum (see Fig. 5.2), the Ag SP waveguide section is kept in air. To reduce reflection losses at the Si-air transition region of the top dielectric the Si should be manufactured into a wedge, creating a graded index profile (see Fig. 5.5). A back reflector is integrated with the Ag/Si:Er source to achieve unidirectional SP propagation.

Given the relatively low power efficiency expected from the Ag/Si:Er SP source, detection at the end of the SP must be made very efficient. Here, we can take advantage of the distinct dispersion behavior of SPs, compared to pure photons. Figure 5.6 shows the SP dispersion relation for the symmetric SP mode at a SiO_2/Ag/SiO_2 multilayer for different Ag thicknesses. These relations are derived from the position of the SP resonance in the power dissipation of the dipole (see Fig. 4.7), calculated for different emission frequencies. As can

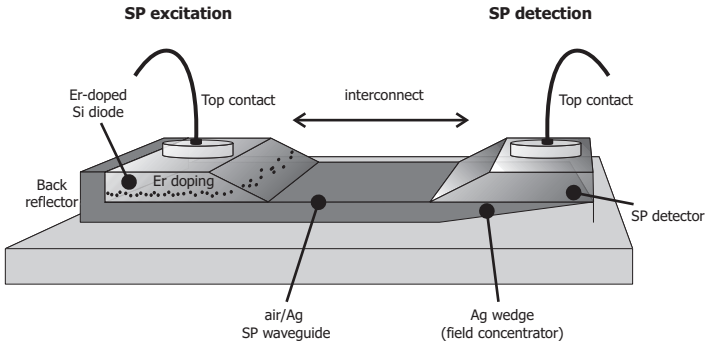

Figure 5.5: Prototype of a SP-based optical interconnect.

be seen, for decreasing Ag thickness, the SP dispersion bends further away from the semi-infinite SP dispersion, leading to an enhancement of the SP wavevector at a given frequency. The change in dispersion is due to the fact that for thin metal films the SP fields on both sides of the Ag film interact.[55][63] As a result of the changing dispersion for thinner metal films, the group velocity of the symmetric SP mode decreases.[64] In the limit of zero Ag thickness the group velocity vanishes and the SP becomes a static surface charge oscillation. Thus, by fabricating a metallic taper with gradually decreasing thickness, the SP field can be concentrated and thus more easily detected. Note that in the SP interconnect scheme presented here the metal is a natural ingredient not only to carry the SPs, but also as an electrical contact in both the excitation and detection part of the device.

Detecting the low power levels associated with SPs propagating over long metallic interconnects is a serious challenge. Efficient Ge-diode infrared detectors are compatible with Si-integrated circuit manufacturing. Although relatively inefficient, backtransfer from excited Er ions to the Si host represents an alternative way to generate a photocurrent when illuminated with infrared light.[22] This represents the detection counterpart of the SP source presented in Section 5.3.1. Finally, we note that propagating SPs represent oscillating electrical currents that may be directly converted into an electrical signal.

5.4.2 Quantum efficiency enhancement by surface-plasmon excitation

SPs can also be used to induce large improvements in the emission rate and quantum efficiency of LEDs, as we will demonstrate next. We distinguish two different concepts. First, Si:Er LEDs have a low internal QE, as the slow radiative decay of Er competes with non-radiative processes.[65][66][22] If the Er excitation can be efficiently coupled to SPs, and the SP subsequently coupled

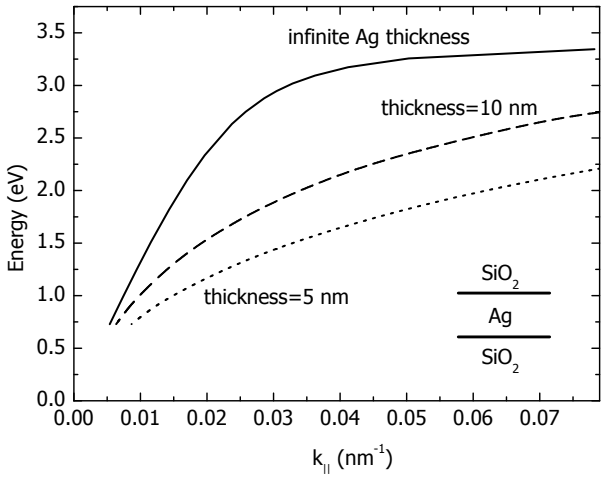

Figure 5.6: SP dispersion for SPs on a semi-infinite Ag layer (solid line), 10 nm thick Ag film (dashed line), and 5 nm thick Ag film (dotted line).

out into the far field, the effect of these non-radiative processes can be reduced. SP out-coupling can be efficiently achieved using a properly engineered grating that relaxes the momentum mismatch between SP and photon, as we have shown in Chapter 2.

Figure 5.7 shows a calculation of the enhanced QE using this concept. Curves are shown for emitters with a radiative emission rate of 1000 s^{-1} (the typical decay rate of Er in Si), and an internal QE of 0.5, 5 and 50 %, plotted against the SP excitation rate. Calculations are made assuming a SP extraction efficiency of 100 %. To achieve a significant QE enhancement the SP excitation rate should be larger than the non-radiative decay rate. For a high-QE emitter ($\sim$50 %) the SP excitation rate should be around W_{rad}, for a low-QE emitter ($\sim$0.5 %) the SP excitation rate should be around $200 \cdot W_{rad}$. An additional advantage of coupling to SPs and subsequent out-coupling through a grating is that the far-field radiation is emitted at a well-defined angle (see Chapter 2), thus solving the general problem of light extraction from (high-refractive index) LEDs. Figure 5.8 shows a design for an Er-doped Si LED. A Ag film is used both as a back electrode, and to carry the SPs, that are subsequently coupled out through a grating integrated in the bottom Ag contact. By using a thin Ag film, rather than an optically thick film, for which the calculation in Fig. 5.3 was done, the SP excitation rate at the Si/Ag interface can be further enhanced (see Chapter 4).

Second, Si-nanocrystal-doped LEDs may have a high QE (the internal QE determined in Chapter 4 was 77 %), but they still suffer from a relatively low emission rate. This is the result of the indirect bandgap of Si nanocrystals that leads to a low electron hole recombination rate. If Si-nanocrystals can

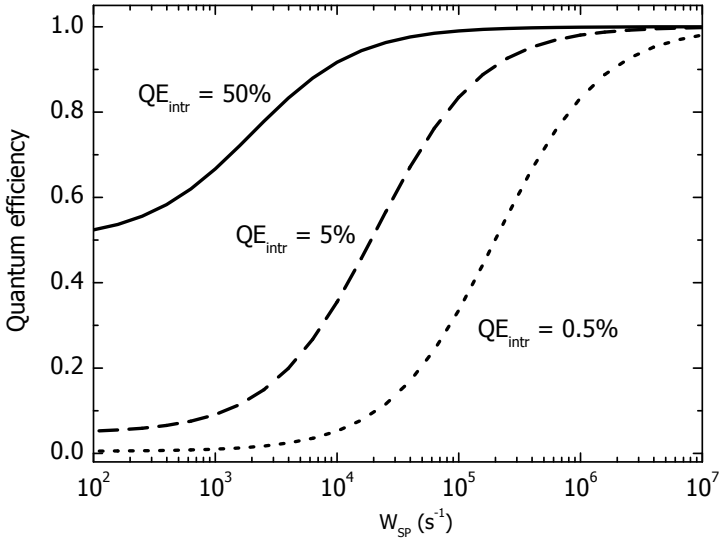

Figure 5.7: QE as a function of SP excitation rate for a radiative decay rate of 1000 s^{-1} (indicated) and 100 % SP out-coupling efficiency. For three different internal QEs, the QE, enhanced by SP coupling, is shown.

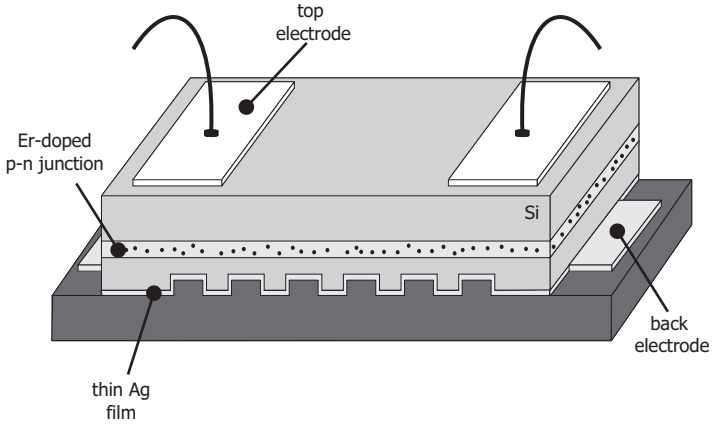

Figure 5.8: Prototype of a QE-enhanced LED.

be efficiently coupled to SPs, the emission rate can be artificially enhanced, and thus Si-nanocrystal-based LEDs with high modulation frequency become possible.

5.4.3 Surface plasmon optical switching

The dielectric/metal combination intrinsic to SPs at optical frequencies can be utilized for combining electronics and photonics by using the metal surface as an electrical contact. Electro or thermo-optic effects [59] can be utilized to affect the propagation properties of SPs in a metal waveguide. With a refractive index of 2.2 and no losses for infrared wavelengths, $LiNbO_3$ is a good candidate for the top dielectric layer of a SP waveguide. Its large linear electro-optic coefficient is ideal to induce a large refractive index change. Here we propose a SP Mach-Zehnder interferometer, a schematic is shown in Fig. 5.9. Modulating the voltage on the electrodes changes the refractive index of the top $LiNbO_3$ dielectric layer. The change in refractive index leads to an increase of the SP wavevector at a fixed frequency, especially for frequencies close to the SP resonance (see Fig. 5.2). The change of the SP wavevector in one branch of the interferometer leads to constructive or destructive interference at the output, depending on the magnitude of the change. Changing the voltage over the electro-optic modulator switches the SP fields on or off at the output.

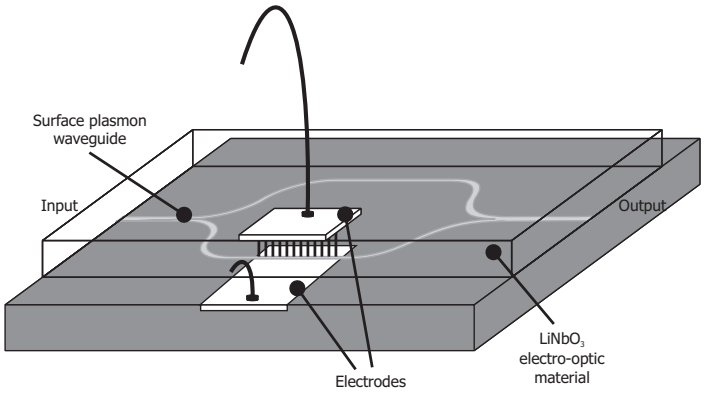

Figure 5.9: Prototype of a surface plasmon Mach-Zehnder interferometer.

Part II

Controlled emission in microcavities

Chapter 6

Erbium-implanted silica microsphere laser

Spherical silica optical microresonators were doped with erbium ions by ion implantation at energies of 925 keV and 2.05 MeV using a rotation stage. After thermal annealing at 800 ^{o}C, a tapered optical fiber was used to couple light into the microsphere. An optical quality factor as high as $1.9{\cdot}10^{7}$ was observed at λ=1450 nm, corresponding to a modal loss of only 0.01 dB/cm. When pumped at 1450 nm, multi-mode lasing around 1570 nm is observed at a threshold between 150 and 250 μW depending on the overlap between the optical mode and Er distribution. This work demonstrates the compatibility of ion implantation and microresonator technology.

6.1 Introduction

Optical microcavities are now being studied over both a wide range of applications and geometries.[67] Of all optical microcavities, silica microspheres exhibit the highest quality (Q) factors to date.[68] Q factors of more than 10^9 can be obtained,[69] corresponding to optical losses that are several orders of magnitude lower than typical losses in planar waveguide structures. Spherical microcavities are made of silica glass using melting and surface-tension induced smoothing. When doped with optically active erbium ions, these microspheres show lasing at the $^4I_{13/2} \rightarrow ^4I_{15/2}$ transition of Er^{3+} around 1.5 μm.[70] So far, lasing has been observed in microspheres that were homogeneously doped with Er. In this geometry, the low-intensity tails of the optical pump mode lead to incomplete pumping of certain erbium-doped regions that interact with the lasing mode. The resulting large absorption due to unexcited Er can increase the lasing threshold, and induce operation in a pulsed mode due to saturable absorption. To achieve lower thresholds and continuous-wave operation, it would be advantageous to fabricate structures where the Er distribution is tailored to the optical mode, with the peak Er concentration located at the peak of the mode distribution. One route to such an optimized profile involves coating the surface of a sphere with a thin layer of erbium-doped sol gel.[71] In this chapter we describe an alternative method using high-energy Er ion implantation. We demonstrate that very high Q factors ($>10^7$) can be achieved in ion implanted microspheres and demonstrate low-threshold (150 μW) lasing operation.

6.2 Experimental

Silica microspheres were made by melting the end of a stripped standard telecommunication fiber (SMF 28) with a CO_2 laser (λ=10.6 μm). After melting and solidification controlled by surface tension, a near-perfect spherical shape, with a radius of $\sim$22 μm was achieved (see inset in Fig. 6.1). The microsphere remained attached to a fiber stem, which was subsequently heated to induce a 90^o bend, enabling convenient attachment of the microresonator-stem assembly with ceramic adhesive to a planar substrate . Before further processing the optical Q factor was tested and values in excess of 10^8 were observed. The substrate was then mounted on a rotating stage, allowing homogeneous implantation of Er ions into the surface of the microsphere and preventing deformation of the sphere in the equatorial plane.[72] Erbium ions were generated using a sputter ion source in a 1 MV van de Graaff accelerator. The ion beam was electro-statically scanned through a 5×5 mm^2 aperture, while the microsphere was slowly rotated around the stem axis. In this way a homogeneous Er implant distribution was obtained in the microsphere's equatorial plane. Two samples were made: 925 keV Er^+ implanted at a fluence of $7.2 \cdot 10^{15}$ cm^{-2} and 2.05 MeV Er^{2+} implanted at a fluence of $1.1 \cdot 10^{16}$ cm^{-2}. Planar reference samples were implanted simultaneously, and then analyzed using Rutherford backscattering spectrometry. Gaussian depth profiles were

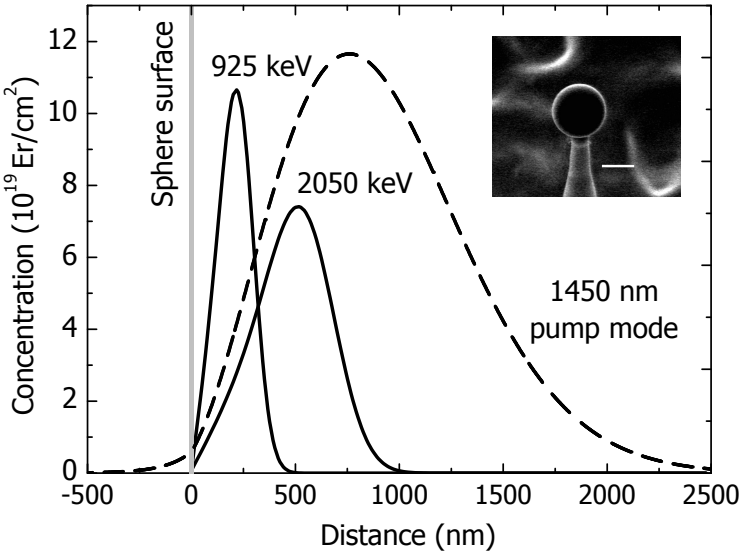

Figure 6.1: Calculated Er implantation profiles for 22 μm-radius silica microspheres implanted with 925 keV Er^+ ($7.2{\cdot}10^{15}$ cm^{-2}) and 2.05 MeV Er^{2+} ($1.1{\cdot}10^{16}$ cm^{-2}) using a rotating geometry. Measured ion ranges and straggles for planar samples were used as input. Also indicated is the 1450 nm pump mode profile (dashed line) for a 22 μm radius sphere. The inset shows an optical micrograph of a microsphere on a fiber stem (scale bar 50 μm).

observed in the planar sample, peaking at 265 (614) nm with a straggle of σ=71 (142) nm for the 925 (2050) keV implant. Due to the spherical shape and rotation of the sample, the Er depth profile in the microresonator is substantially different from that of the planar reference sample. Figure 6.1 shows the calculated Er depth profiles in the radial direction. When compared to the reference samples, both a reduced Er peak concentration and a reduced projected range were observed, with the 925 keV implant peaking at 226 nm (peak concentration $1.1{\cdot}10^{20}$ cm^{-3} (0.16 at.%)), and the 2.05 MeV implant peaking at 501 nm (peak concentration $7.4{\cdot}10^{19}$ cm^{-3} (0.12 at.%)).

Figure 6.2 also shows the calculated depth distribution of the fundamental mode in a 22 μm-radius microsphere at λ=1450 nm, a typical pump wavelength. As can be seen, the overlap between Er distribution and pump mode for the 2.05 MeV implant (Γ_{2050}=0.31) is much larger than for the 925 keV implant (Γ_{925}=0.07). Indeed, as aimed for in this experiment, negligible Er is present in the deeper tails of the mode, beyond 1 μm depth. After implantation, the microspheres where annealed for one hour at 800 ^{o}C in a vacuum oven to optically activate the Er ions.[23] The Er photoluminescence lifetime measured at λ=1535 nm was 10-12 ms for both samples, typical for Er in silica at a concentration of $\sim$0.1 at.%.[23]

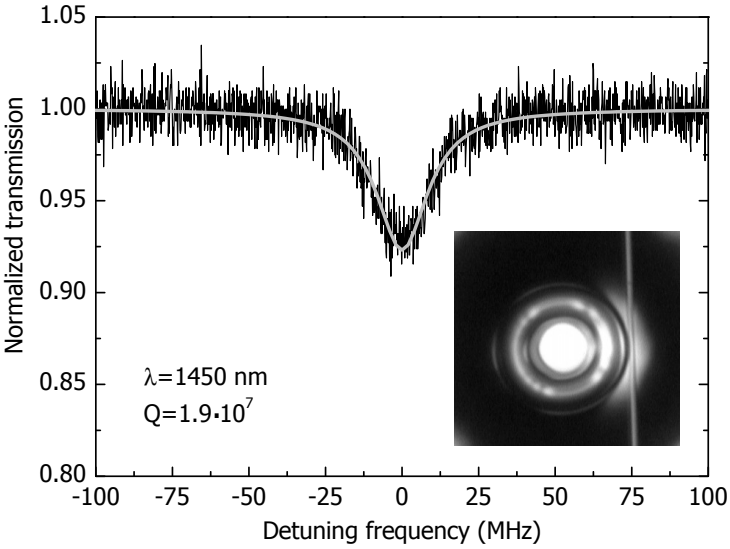

Figure 6.2: Optical transmission spectrum around λ=1450 nm measured in the under-coupled regime. Solid line shows a calculation from which the quality factor (Q = $1.9{\cdot}10^7$) was derived. The inset shows a top view of the fiber-microresonator coupling geometry.

6.3 Results and discussion

To measure the lasing characteristics of the Er-implanted microspheres, a tapered optical fiber was fabricated and coupled to the microsphere (see inset in Fig. 6.2). Details of the taper fabrication process and coupling geometry are described in Ref. [73]. The output from a tunable external-cavity diode laser operating around 1.5 μm was coupled into the fiber, and the transmitted and reflected power were monitored at output and input ends. Lasing emission was collected through the tapered fiber and analyzed with an optical spectrum analyzer. Figure 6.2 shows the transmission spectrum around λ=1450 nm for a tapered fiber positioned more than 1 μm from the 2.05 MeV implanted microsphere (i.e. in the under-coupled regime). By fitting the spectral shape of the resonance, an intrinsic Q factor of $1.9{\cdot}10^7$ was obtained. This value is similar to the Er-absorption related Q calculated using the mode overlap derived from Fig. 6.1 and the Er absorption cross section of $2{\cdot}10^{-22}$ cm^2 at 1450 nm.[74] This shows that cavity losses are dominated by Er absorption rather than intrinsic losses. Besides absorption, scattering centers can give rise to strong modal coupling and splitting of modes into doublets.[75] The absence of splitting indicates that ion implantation and subsequent thermal annealing does not create additional scattering. The obtained quality factor of $1.9{\cdot}10^7$ corresponds to a modal loss of 0.01 dB/cm, which is quite well suited for many applications.

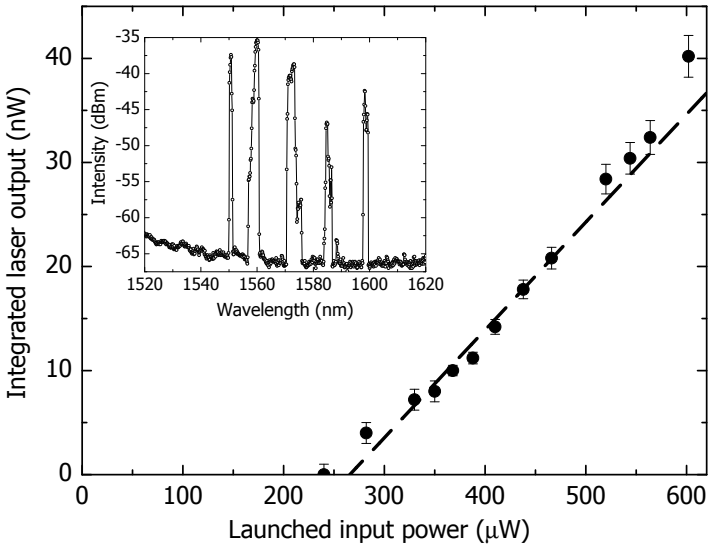

Figure 6.3: Lasing output power integrated over all lasing lines plotted as a function of pump power at λ=1450 nm for a microsphere doped with 925 keV Er. A lasing threshold of 250 μW is observed. The inset shows a typical lasing spectrum.

This clearly shows that high-energy ion implantation, when combined with the proper thermal processing, is compatible with high-Q microcavity fabrication. When pumped at sufficiently high power, the Er-implanted microsphere exhibits lasing. The inset in Fig. 6.3 shows a lasing spectrum (launched pump power >1 mW) of the 925 keV implanted microsphere taken at a relatively low optical resolution ($\Delta\lambda$=0.14 nm). Multimode lasing operation is observed at wavelengths slightly longer than the main Er transition. The latter is attributed to the lower Er absorption cross section at longer wavelengths, causing a reduced lasing threshold.[76]

From the spectral spacing in the lasing spectrum a free spectral range of 12 nm is derived, corresponding to a sphere radius of approximately 22 μm (see Eq. 7.1). Figure 6.3 shows, for the 925 keV Er implanted sample, the output power, integrated over all lasing lines, as a function of input power launched into the input fiber. A linear increase of the output power is observed above a threshold of 250 μW. The slope efficiency measured under these coupling conditions is $1{\cdot}10^{-4}$. The conversion efficiency can be significantly increased by increasing the Er concentration.[76] Consequently, this will result in an increased threshold. A similar measurement was performed for the 2.05 MeV implanted sample, and a threshold of 150 μW was observed (data not shown). This lower threshold for the deeper implant is consistent with the better overlap between Er and mode profile, as shown in Fig. 6.1. When

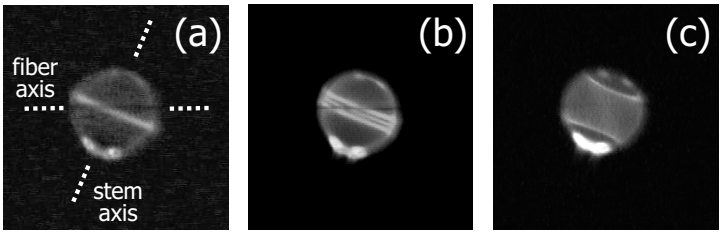

Figure 6.4: Optical micrographs of an Er-implanted microsphere (2.05 MeV) under lasing conditions. Green upconversion emission is imaged (in black and-white). Directions of fiber axis and microsphere stem are indicated. Three different coupling conditions are used in images (a), (b), and (c), leading to distinctly different optical mode spatial distributions.

operated above the 1.5 μm lasing threshold, clear green emission from the microlaser was observed by the naked eye. Optical micrographs taken with a CCD camera sensitive in the visible are shown in Fig. 6.4 for the 2.05 MeV Er implanted sample. The visible emission is attributed to transitions from the $^4F_{7/2}$ and $^2H_{11/2}$ levels to the ground state of Er^{3+}. These higher lying levels can be populated through a combination of cooperative upconversion and excited state absorption transitions.[77] By changing the coupling conditions (e.g. taper-fiber distance) different spatial modes can be excited with different spatial upconversion emission patterns, as can be seen in Figs. 6.4 (a), (b), and (c). Whispering gallery modes are described by three mode numbers: angular (l), azimuthal (m), and radial (n). Figure 6.4 shows a fundamental mode (n=1) (a); a mode with two nodes in the polar direction, i.e. l-m=2 (b); and a mode with a very high inclination, l-$m \gg 1$ (c). These data show that Er upconversion emission can be used to provide detailed information on the mode structure in optical microcavities, an effect demonstrated earlier for planar waveguides.[78] This is particularly useful in geometries where the mode profile cannot be calculated analytically. Note that by using this technique of upconversion imaging, a spatial imaging resolution for the infrared mode can be achieved that is well below the diffraction limit at the mode wavelength. Finally, we note that the above work on ion-implanted resonators provided the inspiration for a subsequent project on Er ion implantation doping of toroidal microresonators on a Si chip. More details on these measurements can be found in Chapter 7 and References [76] and [79].

6.4 Conclusions

In summary, we have shown that high energy Er ion implantation (925 keV, 2.05 MeV) can be used to dope spherical optical microcavities with optically active Er ions with a depth distribution that matches well with the fundamental optical mode. When pumped at 1450 nm, lasing is observed, with a lowest

threshold of 150 μW (launched pump power). This work also shows that high-energy ion implantation, in combination with thermal annealing, can lead to doped microcavities with very high Q ($>10^7$). These findings open up a new field of ion implantation/microresonator technology, as all ion beam materials synthesis techniques developed for planar films can now be applied to optical microresonator structures.

Chapter 7

Fabrication and characterization of erbium-implanted toroidal microcavity lasers

Er-doped toroidal microcavities are fabricated using Er ion implantation either before or after microtoroid fabrication. Confocal photoluminescence spectroscopy shows that for both types of microtoroids, Er ions are optically activated. Microprobe Rutherford backscattering spectrometry indicates that for pre-implanted microtoroids Er is located close to the outer surface of the microtoroid and is not diffused. When pumped in the proper geometry, a mode spectrum is observed superimposed on the Er spontaneous emission spectrum, indicating coupling of Er ions to cavity modes. From the measured Er doping profiles and calculated optical mode distributions the Er overlap factor is calculated: it amounts to Γ=0.05 and Γ=0.13 for post-implanted and pre-implanted microtoroids, respectively. Lasing around 1.5 μm is observed for both types of microtoroids, with the lowest threshold (4.5 μW) observed for the pre-implanted microtoroids.

7.1 Introduction

Optical microcavities are dielectric microstructures that confine light both spatially and temporally. They are ideal platforms to study cavity quantum electro-dynamical effects, enhanced or suppressed spontaneous emission, and can be applied in devices such as low-threshold lasers, optical filters and multiplexers and optical memories.[67][80] The figure of merit that describes the cavity is the quality factor Q that is proportional to the typical photon storage time τ=Q/ω, with ω the angular frequency. Planar ring resonator structures have been fabricated with Q up to $1.3 \cdot 10^5$.[81] More recently, photonic crystal microcavities with Q=$1.3 \cdot 10^4$ were demonstrated.[82] The highest cavity Qs, larger than 10^9, have been measured on whispering gallery mode optical resonators based on silica microspheres (see also Chapter 6).[83][70] While interesting because of their ultra-high Q, these microspheres are impractical for use as actual devices because they are fragile and cannot be easily integrated on a Si substrate.

Recently, a new process for the fabrication of silica microcavities on a planar substrate was developed at the California Institute of Technology (Pasadena, USA)[84] that is compatible with Si-integrated circuit manufacturing. It involves standard fabrication processes combined with a laser reflow process that results in silica toroidal ring resonators on a Si substrate with Q>10^8. Light is coupled into these cavities using a tapered optical fiber. Due to the high optical field intensities that can be achieved in these high-Q microcavities, low-threshold lasing [79] and non-linear effects have been demonstrated.[85][86]

In this chapter we describe the doping of these Si-chip based resonators with Er ions, with the aim to fabricate an on-chip Er microlaser. Ion implantation is used as the doping technique since it gives control over the doping profile and composition, and is compatible with Si integrated-circuit manufacturing. We compare two different fabrication methods, one where Er-implanted SiO_2 is used as the starting material from which the microtoroid is subsequently made, and one where the Er is implanted in a fully fabricated microtoroid. We use confocal photoluminescence (PL) spectroscopy and microprobe Rutherford backscattering spectrometry (μRBS) to determine the Er distribution for the two types of microtoroids. Er lasing is observed in both types of Er-doped microcavities and the lasing characteristics are compared.

7.2 Experimental techniques

7.2.1 Fabrication of Er-doped microtoroids

Fabrication of microtoroids was carried out as follows (see Fig. 7.1, described in Ref. [84]). Starting material is a 1-2 μm thick layer of thermally grown SiO_2 on a Si substrate (step 1). Next, a photoresist is spin-coated onto the sample (step 2). Using optical lithography, circular structures are defined in the photoresist, which, after development, leave circular patches of photoresist (step 3). The

circular patches are then transferred into the SiO_2 by wet-chemical etching in HF (step 4). The remaining photoresist is removed with aceton (step 5). Using a XeF_2 gas etch, the Si is isotropically etched, leaving a circular SiO_2 disk on a Si post (step 6). Finally, these disks are transformed into microtoroids by a CO_2 laser pulse (10 W, 1 ms) (step 7). Figure 7.2 shows a scanning electron microscopy (SEM) image of a typical fabricated microtoroid. Erbium doping of these microtoroids is performed in two ways. In the first method, a toroidal microcavity on a chip is fabricated first by the above-described steps and is then implanted with Er ions in step 8 ('post-implanted' microtoroid). In this way a known, but inhomogeneous (not cylindrically symmetric) implantation profile is obtained. In the second method, Er ions are implanted in the SiO_2 base material (step 1), which is subsequently processed into a toroidal microcavity ('pre-implanted' microtoroid). While the latter procedure is more compatible with standard fabrication processes and leads to a higher throughput, the subsequent laser reflow has a significant effect on the Er distribution as we shall show later.

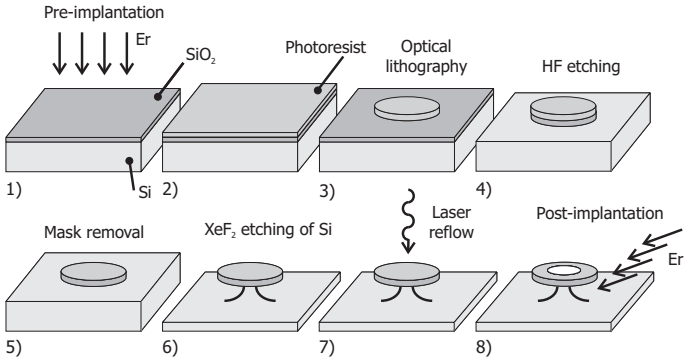

Figure 7.1: Fabrication process of Er-doped ultra-high-Q microtoroids (after [84]). Er-doping is done by ion implantation at step 1) or 8).

Post-implanted microtoroids were made in the following way. An array of 35 freshly prepared microtoroids on a single chip with diameters of around 60 μm were fabricated and their Qs were verified to be larger then 10^7. The Si-chip sample was then mounted on a 70^o wedge that is attached to a Si wafer. In this way Er ions are implanted at an angle of 70^o relative to the toroid's axis of symmetry (see Fig. 7.1). The sample is subsequently implanted with 2 MeV Er^+ at a fluence of $4.2{\cdot}10^{15}$ cm^{-2}. The Er implantation depth profile is Gaussian shaped, peaking at a depth of 596 nm with a peak concentration of 0.2 at.%. The sample is then thermally annealed for one hour at 800 ^{o}C in vacuum. To remove carbon contamination from the surface of the microtoroid (caused by the ion implantation process in some cases) we applied an oxygen plasma etch. Figure 7.2 shows a SEM image of a post-implanted microtoroid with a 'shadow' imprint of the ion beam clearly visible in the background.

Pre-implanted microtoroids were made using samples with 1 or 2 μm thick

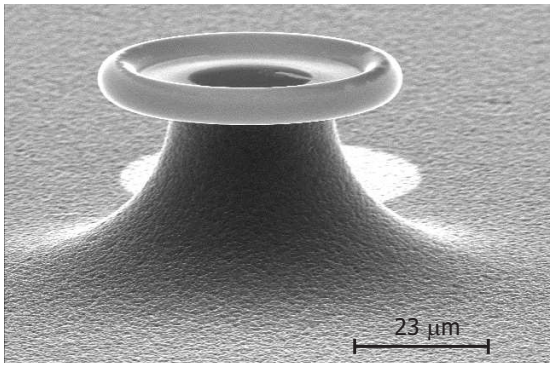

Figure 7.2: Scanning electron micrograph of a typical post-implanted microtoroid. Note the implantation 'shadow' behind the microtoroid.

thermally grown SiO_2 films on a Si substrate. The 2 μm thick SiO_2 was implanted with 2 MeV Er^+ ions at a fluence of either $4.2{\cdot}10^{15}$ cm^{-2} or $1.2{\cdot}10^{16}$ cm^{-2}. This brings the Er ions close to the center of the film (projected range R_p=596 nm) with a peak concentration of 0.2 at.% or 0.65 at.%. The 1 μm thick SiO_2 was implanted with 300 keV Er^+ at a fluence of $2.8{\cdot}10^{15}$ cm^{-2}. This leads to a shallower Er profile (R_p=110 nm), with a peak concentration of 0.7 at.%. As these sample were also used for experiments to sensitize Er ions with Si nanocrystals,[87] 73 keV Si was subsequently implanted in the Er-doped SiO_2 at a fluence of $1.7{\cdot}10^{16}$ cm^{-2}. Both samples were thermally annealed before further processing; the 2 μm Er-implanted SiO_2 for one hour at 800 ^{o}C in vacuum, the 1 μm Er and Si implanted SiO_2 for 30 minutes in Ar/O_2 flow at 1000 ^{o}C, followed by an anneal for 30 minutes in forming gas at 500 ^{o}C. Finally, from the Er-doped oxide layers, toroidal microresonators were fabricated ('pre-implanted') using the method described above.

7.2.2 Time-resolved and confocal photoluminescence spectroscopy

Time-resolved infrared PL spectroscopy was performed using lock-in amplification in combination with a time-modulated Ar-ion laser, 480-mm monochromator, and a liquid-nitrogen cooled Ge-diode detector. The laser spot diameter was $\sim$500 μm and thus covered an entire microresonator structure so that PL spectra and lifetimes averaged over the entire structure were measured. A high-magnification CCD camera was employed to position the laser spot on a particular microdisk or microtoroid structure on the Si chip sample.

Spatially resolved PL spectroscopy was done with a scanning confocal microscope (WITec GmbH, Germany). We used a frequency-doubled Nd-YAG laser operating at a wavelength of 532 nm of which the output is coupled into an optical fiber that is fed into the microscope. The laser beam is directed onto

the sample using an infrared beamsplitter and is focussed using either a 60× objective (air) or a plan apochromatic 100× (oil immersion) objective (NA=1.4). High-resolution images were obtained using index matching. The microtoroid sample was enclosed in a small chamber, covered with a 170 μm thick cover slide, filled with index matching oil. This assembly was then imaged by using oil (n=1.52) between objective and sample. While index matching does provide the highest possible spatial resolution, it makes it impossible to locate the toroidal perimeter in the images. To enable direct comparison between PL images and the toroidal volume, the immersion oil was lightly doped with Rhodamine dye (emission maximum at 545 nm). As it turned out, the dye preferentially coats the toroid's surface and its luminescence can be used to probe its outer contours. The infrared Er PL is collected via the objective and fed into an optical fiber with a 100 μm core that is located in the image plane, and acts as the confocal detection pinhole. The PL is then dispersed with a 300-mm monochromator with a resolution of 0.1 nm and imaged onto either a Si CCD detector operating in the visible (λ=350-900 nm) or a InGaAs infrared CCD detector (λ=800-1700 nm). The sample is scanned in either the x-y or the x-z plane of the toroidal structure, while at every point of the scan a PL spectrum is recorded. PL intensity distributions are obtained by integrating a spectral region of the measured spectrum. Using a reference sample with a thin dye layer film the resolution in the z-direction at λ=580 nm was measured to be 800 nm. At λ=1500 nm the expected resolution is $\sim$2 μm. The lateral resolution in x and y direction is expected to be somewhat smaller.

7.2.3 Microprobe Rutherford backscattering spectrometry

Microprobe Rutherford backscattering spectrometry was performed to determine the Er depth profile inside the microtoroids with a High-Voltage Engineering Singletron ion accelerator using a 2 MeV He^+ microprobe beam. A passivated implanted planar silicon detector mounted at 147^o relative to the incident beam was used to detect backscattered He^+ ions. Simultaneously, the particle-induced X-ray emission (PIXE) was detected using a liquid-nitrogen cooled Ge detector. The circularly shaped He^+ beam (2.5 μm diameter) was scanned over the sample area at a rate of 1 kHz. The beam current at the sample was 200 pA, as measured with a Faraday cup located at the entrance of the scattering chamber.

7.2.4 Fiber coupling to microtoroids

The quality factors of the Er-implanted microtoroids were determined by measuring the transmission spectrum of a tapered optical fiber brought in close proximity to a microresonator. We used a scanning narrow-linewidth external-cavity diode laser (1400-1500 nm) that is fed into the tapered optical fiber. The laser scanning speed was chosen sufficiently low such that at each frequency the mode intensity and the Er population reach a steady state. The tapered optical fiber is mounted on a high-precision piezo-electric stage (step

resolution 20 nm). At a fixed distance from the microtoroid a transmission spectrum is measured by scanning the laser frequency over a cavity resonance and measuring the transmitted intensity with a photodetector. A fit of the transmission spectrum with a function based on coupling-of-modes theory [88] then allows to determine the intrinsic cavity quality factor (i.e. without loading loss). More details on coupling and tapered fiber fabrication can be found in References [70][73][89].

7.3 Results

7.3.1 Confocal photoluminescence spectroscopy

Post-implanted microtoroids

Figure 7.3 shows two-dimensional cross sections of the Er PL distribution in a post-implanted microtoroid. Integrated intensity in the wavelength range of 1520-1565 nm is plotted, corresponding to the $^4I_{13/2} \rightarrow {}^4I_{15/2}$ transition of Er^{3+}. Figure 7.3(a) shows the x-y PL cross section (taken at the z-position indicated by the vertical line in Fig. 7.3(b)). With a subsequent measurement at the same position of the two-dimensional distribution of the Rhodamine PL in the visible (not shown) the outer perimeter of the microtoroid was estimated and is sketched in Fig. 7.3(c). The toroid's major diameter is 57 μm, the minor diameter is 6 μm. Also indicated is the direction of the Er ion implantation, at an angle of 70^o relative to the surface normal. As can be seen in Fig. 7.3(a), the implantation results in a very inhomogeneous Er distribution along the circumference of the microtoroid. At the side facing the ion beam Er ions

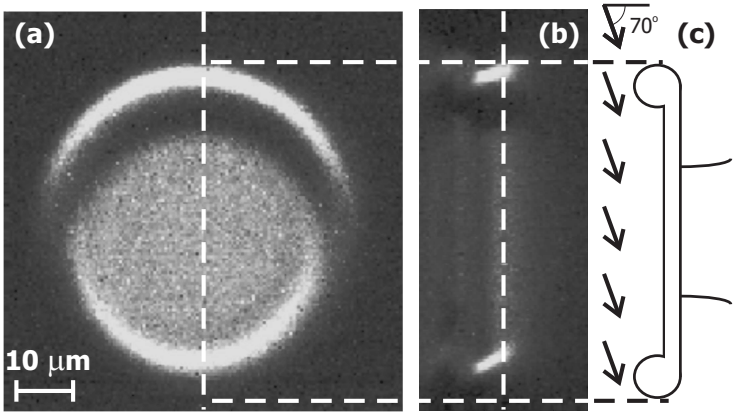

Figure 7.3: Confocal PL microscopy images (λ=1540) of a post-implanted microtoroid. (a) x-y PL cross section, with the vertical line showing the location of the x-z cross section in (b). (b) y-z PL cross section, with the vertical line showing the location of the cross section in (a). (c) x-z outer perimeter of the toroid determined from spatially imaged Rhodamine PL. Also indicated is the implantation angle of 70^o.

are located near the outer perimeter of the microtoroid. At the opposite side, where the toroidal ring protrudes upwards, the Er ions are located at the inner perimeter. Clear 'shadowing' effects can be observed at the sides of the ring that face away from the ion beam direction, which is due to the finite projected range of the Er ions. The inner region of planar SiO_2 shows Er PL, albeit at a lower intensity, due to the fact that the Er ion fluence is geometrically reduced (by $\cos(70^o)$) because of the oblique angle of incidence.

Figure 7.3(b) shows the x-z infrared Er PL cross section (image plane taken along the vertical line indicated in Fig. 7.3(a)). Again this image shows that on the side facing the ion beam, the Er ions are located at the outer perimeter of the toroidal ring in contrast to the side opposite the ion beam, where the Er ions are located at the inner perimeter of the toroidal ring. Also the inclination of the ion beam with respect to the sample can be observed from the Er PL distribution at the outer perimeter, it is approximately 70^o. A slightly different angle is observed at the inner perimeter, which is attributed to a different curvature of the toroidal surface at the inner perimeter. From these images we can conclude that the Er ions are indeed distributed as expected from the implantation energy and angle, and that optical activation of the implanted Er ions through the entire implanted section of the toroid is achieved.

Pre-implanted microtoroids

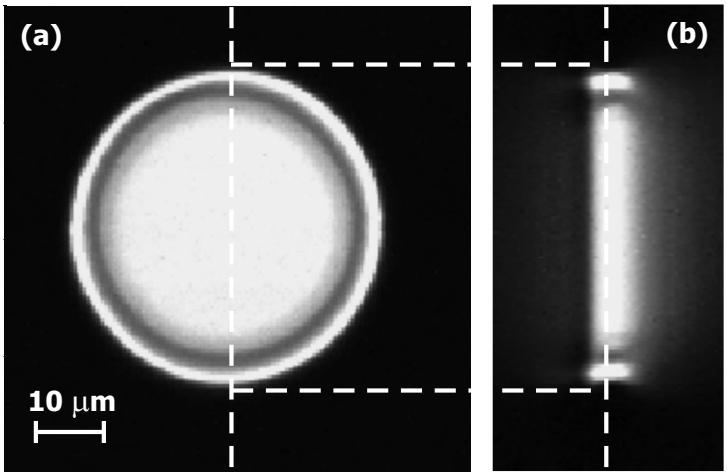

Figure 7.4: Confocal PL microscopy images (λ=1540) of a pre-implanted microtoroid. (a) x-y cross section, with vertical line showing the location of the x-z cross section in (b). (b) x-z cross section, with the vertical line showing the location of the cross section in (a).

Figure 7.4 shows two-dimensional confocal infrared PL cross sections of a pre-implanted microtoroid. Figure 7.4(a) shows the x-y PL cross section of

this microtoroid (image plane taken at the z-position indicated by the vertical line in Fig. 7.4(b)). Figure 7.4(b) shows the x-z PL cross section (image plane taken at the y-position indicated by the vertical line in Fig. 7.4(a)). The microtoroid's outer diameter is 57 μm and the minor diameter is 6 μm. It is clear that Er is optically activated throughout the entire toroidal ring. The cylindrically symmetric PL distribution is in agreement with the fabrication procedure. Given the resolution of Er PL mappings described in Section 7.2.2 it is difficult to determine the precise location of Er ions in the toroidal structure. The distribution of Er ions in the pre-implanted microtoroids is the result of a complex process where Er is first implanted in a planar film and then the laser reflow is used to form the microtoroid. In contrast to the post-implanted microtoroids, the reflow process results in a unknown roll-up/collapse process and may also cause Er diffusion in the formed structure, leading to an unknown Er doping profile. μRBS was used to investigate this further.

7.3.2 Microprobe Rutherford backscattering spectrometry

Figure 7.5 schematically shows three different Er doping models. Figure 7.5(a) shows the most simple reflow model, the structure has rolled up into a ring and, due to thermal diffusion, the microtoroid is homogeneously doped with Er. In this model it is assumed that during the laser reflow of the SiO_2, the temperature-time profile is such that Er can diffuse over large distances. Figure 7.5(b) shows an alternative model where the Er does not diffuse and is immobile relative to the SiO_2 and thus follows the plastic deformation of the SiO_2. In model (b) the SiO_2 curls in an upward direction. In this case the Er ions are relatively far away from the outer surface of the microtoroid (the SiO_2 thickness minus the Er projected range). Figure 7.5(c) shows a process similar as in Fig. 7.5(b), but with the SiO_2 layer curling downwards. In this case the Er ions are located near the outer surface of the microtoroid (distance equal to the projected range). Given the final shape as measured with scanning electron microscopy (see Fig. 7.2), formation of this geometry seems less likely as it implies that the down-rolled ring is subsequently shifted upwards.

To distinguish between the different Er distribution models we measured the Er depth profile spatially resolved. Figure 7.6 shows SEM images taken from the top (a) and side (b) of the microtoroid after the μRBS measurement. Clearly, the periodic raster of the μRBS beam can be observed on the top surface. However, no damage or large-scale deformation of the structure can be observed in either image.[90] Figure 7.6(c) shows a spatial image of the backscatter yield, integrated over all energies. The detector is located at the top of the microresonator structure, giving rise to a 'shadowing' effect at the bottom of the image (i.e. backscattered He^+ ions from that region cannot reach the detector). The top part of the scan has a higher total backscatter yield than the bottom part, a feature that we attribute to the close vicinity of the detector to this side, resulting in a larger detection solid angle.

To obtain detailed information of the Er distribution in both the toroidal

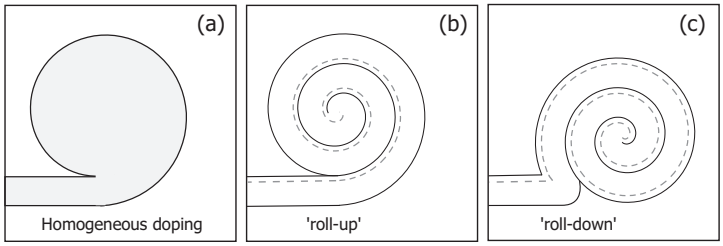

Figure 7.5: Three different models for the Er distribution in pre-implanted microtoroids. (a) Er is homogeneously diffused through the entire toroidal ring. (b) Er is not diffused, the SiO_2 rolls up in an upward direction direction. (c) Er is not diffused, the SiO_2 rolls up in a downward direction. Dotted lines indicate the position of the Er distribution.

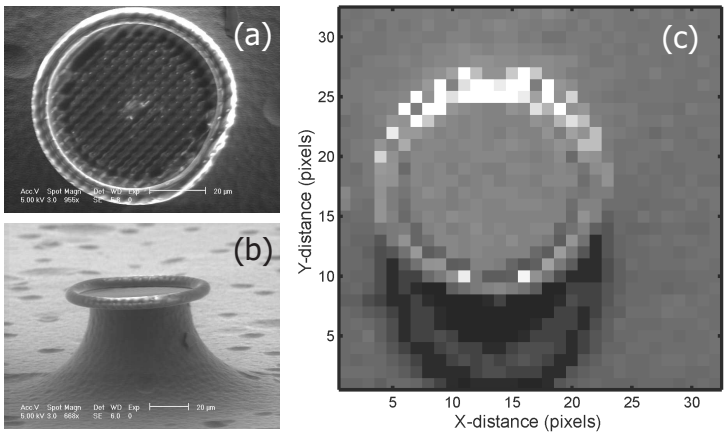

Figure 7.6: (a) Top view SEM image of the microtoroid. (b) Side view SEM image of the same microtoroid. (c) Spatial image of the integrated μRBS yield from the microtoroid presented in (a) and (b).

ring and the planar oxide inner region, μRBS spectra were integrated and summed for both areas. Identification of the pixels belonging to the toroidal ring and inner circle was based on the image in Fig. 7.6(c). Figure 7.7 shows these spatially summed μRBS spectra for both areas. The spectra are normalized to the number of pixels over which they were collected. Figure 7.7(a) shows the integrated RBS spectrum for the inner planar circle section of the microtoroid (see Fig. 7.6(a)). The peak at 1810 keV corresponds to backscattering from Er ions at a depth of 109 nm, the arrow indicates the Er surface channel. An identical depth profile (not shown) was measured on a planar reference sample (without laser reflow). This indicates that Er ions do not diffuse in the silica inner circle upon laser reflow. Note that due to thermal conduction to the Si substrate during the laser pulse, the peak temperature in

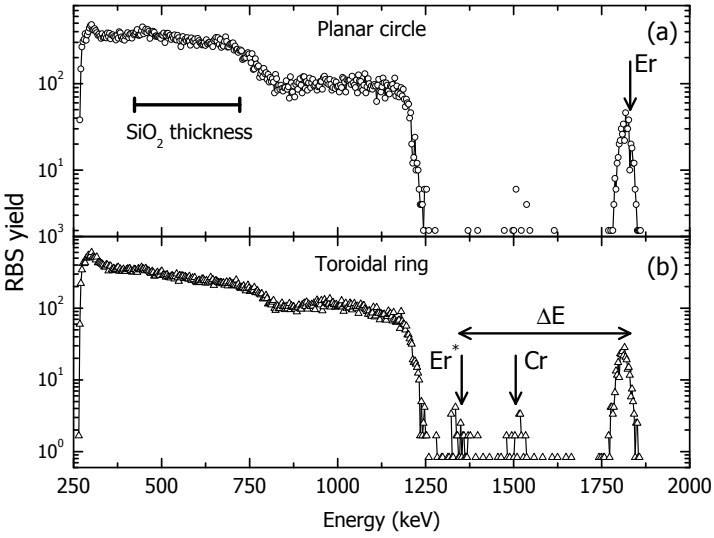

Figure 7.7: (a) RBS spectrum with counts integrated from the planar inner circle of the microtoroid. Indicated is the thickness of the SiO_2 layer. (b) RBS spectrum with counts integrated from the outer circle. The horizontal arrow indicates the energy difference that corresponds to 833 μm SiO_2.

the inner circle is lower than in the outer ring. PIXE measurements showed the presence of Cr and Er on the inner circle, the former is reflected by the peak at 1510 keV, occuring at the surface channel of Cr (indicated). We attribute the presence of Cr to contamination of the initial wafer by the use of the optical lithography mask in the fabrication process.[84] The spectrum also shows the Si and O surface channels at 1225 and 720 keV, respectively. For this sample and RBS geometry the O surface edge overlaps with the surface channel from the Si substrate under the SiO_2, and is therefore difficult to discern. The reduction in O signal below 420 keV is due to the finite width of the SiO_2 layer, indicated by the horizontal bar. A simulation of the multilayer structure gave an estimate for the SiO_2 areal density of $5.5{\cdot}10^{18}$ at./cm^2, corresponding to 833 nm, somewhat smaller than the 1 μm oxide thickness of the starting material.

Figure 7.7(b) shows the summed RBS spectrum for the toroidal ring section of the microtoroid. The Er distribution is identical to the Er distribution of the planar circle section in Fig. 7.7(a). Consequently, we can immediately conclude that the Er ions do not diffuse through the SiO_2 toroidal ring during laser reflow, thus excluding model (a) in Fig. 7.5. Interestingly, a small peak can be observed in the spectrum at 1340 keV (indicated by Er*) that is not observed for the inner circle region in Fig. 7.7(a). The energy separation of this peak and the major Er peak near the surface matches the energy loss

corresponding to the stopping in the SiO_2 layer with a thickness of 833 nm determined from Fig. 7.7(a). This peak thus reflects a second Er layer buried one layer deep in the rolled-up spiral. The shallow Er peak (depth 109 nm) seems in agreement with model (c). However, it should be noted that the laser anneal leads to a significant amount of SiO_2 evaporation. Thus, even a deep Er profile (as in model (b)) can become closer to the surface due to evaporation. The occurrence of evaporation is also consistent with the smaller oxide thickness of 833 nm found for the inner circle, compared to the starting oxide thickness of 1 μm.

The absence of Er diffusion upon laser reflow is in agreement with an extrapolation of RBS measurements of thermally annealed Er implanted SiO_2 reported in Ref. [23]. It was found that Er depth profiles before and after annealing for one hour at 1200 ^{o}C showed no substantial diffusion. The Er diffusion length is then estimated to be smaller than 10 nm. Using an activation energy of 3.5 eV, a high value even for diffusion in amorphous materials, the diffusion length, calculated for a laser anneal of 1 ms (typical laser pulse duration) at an estimated temperature of 2000 K, is smaller than 10 nm, in agreement with our μRBS depth profiling measurements.

For both types of Er-implanted microtoroids we now have determined the distribution of optically active Er ions, information that is crucial in analyzing the optical measurements that follow.

7.3.3 Time-resolved photoluminescence spectroscopy

We measured the Er PL emission in a pre-implanted microtoroid as well as in a microdisk (after step (6) in Fig. 7.1, no laser reflow) both located on the same Si chip, and implanted with $1.2{\cdot}10^{16}$ Er/cm^2. The structures are excited from the top with 488 nm laser light and the PL is collected from the top. Figure 7.8 shows the Er PL emission spectra. Both samples show characteristic Er PL emission peaking at 1536 nm. No additional structure in the PL emission spectrum (due to coupling of Er ions to cavity modes) is visible. Indeed, PL emitted perpendicular to the sample is mainly due to spontaneous emission into the far-field, and is not affected by coupling to cavity modes. Er emission coupled to cavity modes emanates preferentially in the plane of the microdisk/toroid and is not probed in this experiment. PL lifetimes were measured at the peak Er emission wavelength. Both microtoroid and microdisk show a similar lifetime of 10.5 ms. This lifetime is substantially shorter than the radiative lifetime of 18 ms for Er ions in thermal SiO_2.[5] We attribute this to concentration quenching processes that, through resonant energy transfer between Er ions, causes quenching of excited Er ions to OH impurities in the SiO_2. Using a linear concentration quenching model (see Eq. 3.1) with $C_{Er,Er} = 2.9{\cdot}10^{-39}$ cm^6/s (see Section 3.3) we obtain an OH concentration of $7.5{\cdot}10^{18}$ cm^{-3}, indeed a lower concentration than the peak Er concentration, thereby validating the linear concentration quenching model. Assuming an OH absorption cross section of $3.5{\cdot}10^{-24}$ cm^2 (estimated from

absorption measurements in glass fibers [91]), we obtain an OH absorption-related Q of $5.2{\cdot}10^8$. This would then be an upper limit of the Q that can be attained in these microcavities fabricated from thermal SiO_2. The fact that similar Er PL lifetimes were observed before and after laser reflow further supports the fact that no significant Er diffusion has taken place. If it had, the Er concentration would have lowered, resulting in less concentration quenching, and thus a longer Er lifetime for the microtoroid, contrary to what is observed.

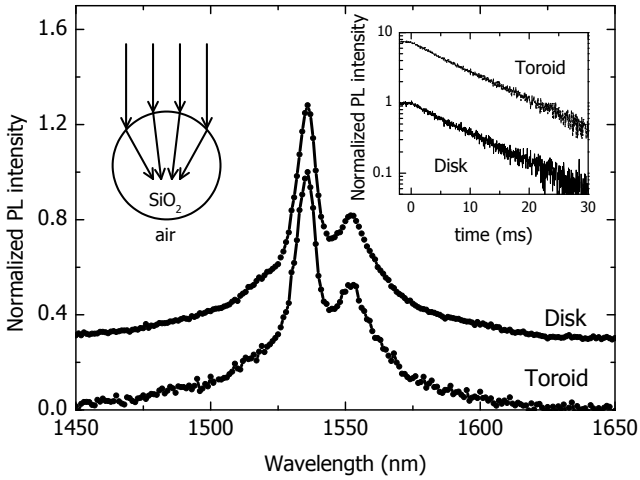

Figure 7.8: Measured Er PL emission spectra of a pre-implanted microtoroid and a microdisk. Inset on the right shows the PL decay measured at the Er peak emission wavelength. Both samples have the same decay rate. Schematic on the left shows refraction of excitation light on the toroidal ring. Er ions close to the outer sides of the ring are inefficiently excited.

Note that in this analysis we disregarded any influence of the cavity on the lifetime of the Er ions. This is justified by the fact that using far-field excitation only a very small fraction of the probed Er ions have substantial overlap with high-Q modes. Due to refraction at the SiO_2/air interface, as sketched in the inset on the left in Fig. 7.8, we expect that Er ions close to the outer perimeter of the microcavity (that can couple efficiently to high-Q modes) are not efficiently excited. Mainly Er ions are excited in the center of the toroidal ring and in the planar SiO_2 where coupling to cavity modes is inefficient.

By using the confocal microscope PL set-up, described in Section 7.2, we can selectively excite Er ions in the microtoroid that couple to cavity modes. The microtoroid (see Fig. 7.9(b)), was mounted sideways under the microscope objective (60×). Focussing on the near-surface region of the microtoroid, tangentially to the perimeter (see inset on the left in Fig. 7.9(c), showing a side view schematic), Er ions were locally excited and their PL emission spectrum was measured (black line in Fig. 7.9(c)). Clearly, periodic peaks, superimposed on the slowly varying Er emission, can be observed. As a reference, an Er PL

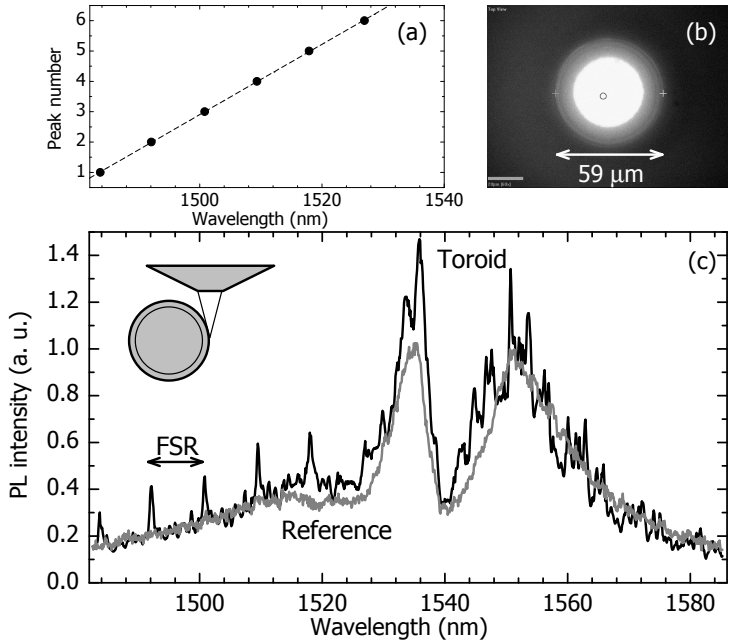

Figure 7.9: (a) Peak number of the PL enhancement observed in (c) versus peak wavelength. (b) Optical microscopy image of the top of the microtoroid, its diameter is indicated. (c) Er PL emission spectra collected from the side of the microtoroid (black line) and from the top of a planar section of the microtoroid (gray line). The inset shows a side view of the experimental geometry.

emission spectrum was measured from the top of a planar section of the same sample (gray line); it does not show the sharply peaked periodic modulation. The sharp peaks are attributed to Er emission that is preferentially coupled into cavity resonances. The resonance linewidths in the Er PL measurement are not limited by detector resolution and correspond to Q factors in the order of 3000, significantly lower than the Q factors obtained from tapered fiber transmission measurements (typically 10^7). Note that the overall shape of the Er emission spectra in Fig. 7.9 is different from that generally observed for Er in SiO_2.[23] Since both measurements have a pronounced dip at λ=1540 nm this is attributed to an interference effect in the confocal microscopy set-up.

After normalizing the Er emission spectrum with the superimposed peaks with the reference spectrum, the periodic oscillation is more easily identifiable. Figure 7.9(a) shows the peak number versus peak wavelength, which is fitted with a linear equation showing that the peaks have an equidistant spacing. The slope results in a free spectra range (FSR) of 8.6 nm. The angular FSR (in

wavelength) is approximated by

$$FSR_\lambda = \frac{\lambda^2}{2\pi R n_{eff}} \quad , \tag{7.1}$$

with R the major radius of the toroid and n_{eff} the refractive index of SiO_2. Using Eq. 7.1 we obtain a radius of 29.4 μm, close to the radius of 29.5 μm obtained from optical microscopy imaging (see Fig. 7.9(b)), further proving that the observed peaks are related to cavity modes. In this analysis we assumed a dispersionless refractive index (which is a good approximation for infrared wavelengths) and the optical mode fully confined to the microtoroid (i.e. n_{eff}=n_{SiO_2}).

We attribute the enhancements in Er PL at the cavity resonances to an enhanced DOS at these resonances, thereby resulting in increased Er spontaneous emission at these wavelengths into these cavity modes. Due to the finite Q, the fields associated with these modes will leak out of the cavity, and can be detected by the microscope objective, located in the plane of the microtoroid. As can be seen in Fig. 7.9(c) a large fraction of the detected Er emission is not influenced by the microcavity.

The enhancement of spontaneous emission has been described by the Purcell [7] (see Chapter 1) for closed cavities. The magnitude of the observed enhancements observed here is much smaller than the value given by the Purcell factor for these cavities (Eq. 1.3). Because microtoroids are open cavities, spontaneous emission can take place in the far field as well as to cavity modes, where only the latter are enhanced by the Purcell effect, reducing the observed effect. Also a large fraction of probed Er ions does not couple to cavity modes and therefore contributes to the background, thereby reducing the relative PL enhancements.

To investigate the relation between cavity modes and Er emission into these modes in more detail, we directly compared tapered fiber transmission measurements on the same microtoroid with the Er PL measurements in Fig. 7.9(c). Figure 7.10(b) shows a section of the mode spectrum obtained from the measurement presented in Fig. 7.9(c). The Er PL was normalized with the reference PL measurement. Figure 7.10(a) shows the transmission spectrum of the same microtoroid measured using a tapered optical fiber in the under-coupled regime. Note that with this method we preferentially excite high-Q modes with the optical mode located close to the perimeter of the microtoroid. It can be observed that the modes, now seen as dips in the fiber transmission spectra, occur at different wavelengths than the modes obtained from the Er PL measurements. Also it is clear that the modes measured in transmission have a much smaller linewidth. However, both measurements show the same angular free spectral range of 8.6 nm. These data confirm that the probed Er ions preferentially couple to lower-Q modes.

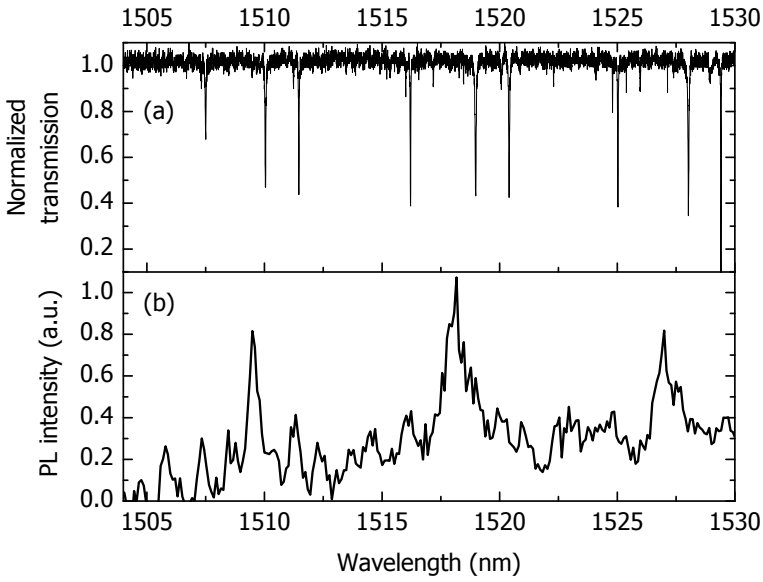

Figure 7.10: (a) Normalized transmission spectra measured through a tapered optical fiber measured in close proximity to the microtoroid. (b) Relative Er PL intensity obtained from Fig. 7.9(c).

7.3.4 Microtoroid quality factors

Both for the post-implanted and the pre-implanted microtoroids we measured the intrinsic Q factors (i.e. not affected by the coupling). Figure 7.11 shows the transmission spectrum taken through the tapered optical fiber around λ=1442 nm measured on a post-implanted microtoroid. The transmission spectrum was fitted with a function derived from mode coupling theory,[88] and from this fit an intrinsic Q factor of $1.6{\cdot}10^7$ was determined. A similar measurement on a pre-implanted toroid yielded $3.9{\cdot}10^7$. To compare the different Qs for pre-implanted and post-implanted microtoroids, the Er concentration, probe wavelength, and mode profiles have to be taken into account.

Using the known implantation profile, the mode overlap Γ was calculated using

$$\Gamma = \frac{\frac{1}{Er_{max}} \int_A Er(x,y) I(x,y) dA}{\int_A I(x,y) dA} \quad , \tag{7.2}$$

with A being a large surface cutting perpendicular through the toroidal ring, Er_{max} the peak Er concentration, $Er(x,y)$ the position dependent Er distribution, and $I(x,y)$ the optical mode intensity distribution. The spatial optical mode distribution was calculated with a finite element method [92] for a microtoroid with a major diameter of 23 μm and a minor diameter of 2.5 μm,

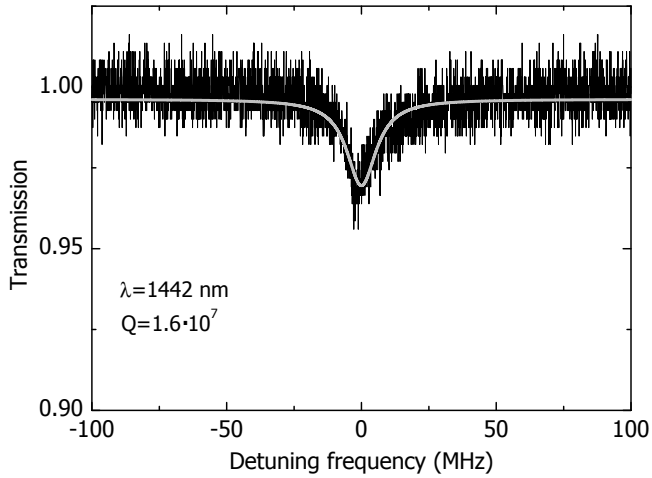

Figure 7.11: Fiber taper transmission spectrum of a post-implanted microtoroid (black). From the fit (gray) an intrinsic Q of $1.6{\cdot}10^7$ was derived.

estimated from the SEM image of the pre-implanted microtoroid. These mode profiles were then fitted with a double-Gaussian function, which was used as an input for the overlap calculation using Eq. 7.2. The Er doping profiles were calculated with the projected range and straggle of the Er ions as inputs. The doping profile for the pre-implanted microtoroid was calculated assuming a Gaussian Er distribution located below the perimeter of the toroidal ring according to the μRBS spectrum in Fig. 7.7(b). Due to the cylindrical symmetry, the overlap Γ was calculated only over the toroidal ring's cross section A. The calculated mode overlap was Γ=0.13.

Due to the absence of cylindrical symmetry for the post-implanted microtoroid the mode overlap of Eq. 7.2 was calculated for a series of toroidal cross sections at different angles. These where then integrated over all angles and appropriately averaged to obtain the average overlap. The mode profile was calculated for a microtoroid with a major diameter of 57 μm and a minor diameter of 6 μm, according to SEM images for this toroid. The resulting mode overlap was Γ=0.05. The much lower overlap factor in post-implanted toroids is the result of the fact that only a small section of the microtoroid is doped with Er ions (no cylindrically symmetric Er distribution).

The Er absorption-related Qs can be calculated for the weak pump regime (i.e. no significant excited state population) with [76]

$$Q_{Er} = \frac{2\pi n}{\mathrm{N}_0 \Gamma \sigma_a \lambda} \qquad , \tag{7.3}$$

with n the refractive index, Γ the mode overlap, N_0 the peak Er concentration and σ_a the Er absorption coefficient at the probe wavelength. For pre-implanted

microtoroids that were probed at λ=1411 nm,[76] we use an Er absorption cross section of $1{\cdot}10^{-22}$ cm^2 at 1411 nm,[93] the Er fluence of $4.2{\cdot}10^{15}$ cm^{-2} and the calculated overlap Γ=0.13 and obtain an Er absorption-related Q=$3.2{\cdot}10^7$, quite close to the experimentally determined Q=$3.9{\cdot}10^7$.

In our previously published analysis of the Er lasing characteristics of these pre-implanted microtoroids [76] we assumed that the Er distribution was homogeneous through the toroid. As the data in Section 7.3.2 shows, this assumption is incorrect. However, the above calculated absorption-related Q is quite similar to that used in Ref. [76], which is due to the fact that the increase in Er peak concentration is counterbalanced by a decreased overlap of the Er distribution with the optical mode.

From the transmission spectrum for a post-implanted microtoroid measured around λ=1442 nm shown in Fig. 7.11 an intrinsic Q factor of $1.6{\cdot}10^7$ is derived. Given the mode overlap Γ=0.05, the implanted Er fluence of $4.2{\cdot}10^{15}$ cm^{-2}, and an Er absorption cross section of $4{\cdot}10^{-22}$ cm^2 at 1442 nm [93] we obtain an Er absorption-related Q=$2{\cdot}10^7$, close to the Q obtained from the transmission experiments. We therefore conclude that the measured Q is predominantly determined by Er absorption.

7.3.5 Erbium microtoroid lasing

Both types of Er-doped microtoroids showed lasing at 1.5 μm when pumped at a power above their lasing threshold. Post-implanted microtoroids were pumped at 1440 nm and showed single or multimode mode lasing around 1552 nm. The lowest obtained lasing threshold in these microtoroids was 125 μW (power launched into the fiber). Figure 7.12 shows the Er lasing spectrum obtained by pumping at 800 μW. When pumped at such high powers intense green emission was observed (see inset in Fig. 7.12). This is related to population of higher Er^{3+} energy levels by a combination of cooperative upconversion processes [94] and excited state absorption.[74] Whether the observed green emission is due to spontaneous emission from the excited higher energy levels of Er or in fact due to lasing, must be further investigated.

The pre-implanted microtoroids showed much lower Er lasing thresholds. Figure 7.13 shows the lasing output power versus power launched into the fiber (λ_{pump}=1465 nm, compensated for tapered fiber losses). Lasing was obtained both in single mode (see inset on the right bottom in Fig. 7.13) and multimode (depending on the pump power). The output power was determined by integrating over all laser lines. The lowest lasing threshold was 4.5 μW of launched pump power for a microtoroid with a Q of $3.9{\cdot}10^7$, pumped at λ=1411 nm, and with a major diameter of 23 μm (see inset on the far left). The pre-implanted microtoroids also showed green upconversion luminescence when pumped at powers far above their lasing threshold. The second inset on the left in Fig. 7.13 shows an image taken with a CCD camera at an oblique angle of the upconversion around the perimeter of the microtoroid.

Given the fact that the calculated Er-absorption related Q agrees well with the measured Q, the lasing threshold is largely determined by the power re-

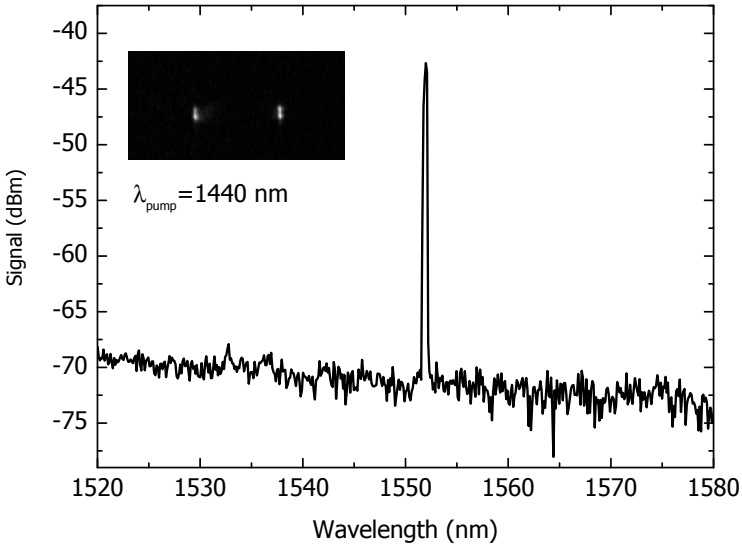

Figure 7.12: Er lasing spectrum for a post-implanted microtoroid pumped at λ=1440 nm. The inset shows a side-view image of the microtoroid, showing green Er upconversion luminescence when pumped at high pump powers (printed in black and white).

quired to invert the Er ions. It thus depends only on the Er concentration, the absorption and emission cross sections, the modal volumes and the overlap of the signal and pump wavelengths with the Er distribution. We attribute the much lower lasing threshold for pre-implanted microtoroids to the much smaller mode volume (the major diameter is 23 μm vs 57 μm) and the higher overlap (Γ is 0.13 vs 0.05) for this microcavity. A detailed description and model of the lasing characteristics is presented in Ref. [76].

7.4 Conclusions

Silica microtoroids were doped with Er ions by ion implantation in the SiO_2 base material or by implanting Er ions in a fully fabricated microtoroid. Confocal PL spectroscopy imaging shows optical activation of Er in the microtoroids. Microprobe RBS showed that for pre-implanted microtoroids Er ions are located close to the microtoroid surface and that no Er diffusion has taken place. Confocal PL spectroscopy imaging shows for post-implanted microtoroids the expected asymmetric Er distribution according to the implantation depth and angle. The Er distribution and calculated mode profiles were used to calculate the mode overlap and Er absorption related Qs. It was found that both post-implanted microtoroids and pre-implanted microtoroids have Er absorption-related Qs that were close to the measured Q values, showing that cavity losses

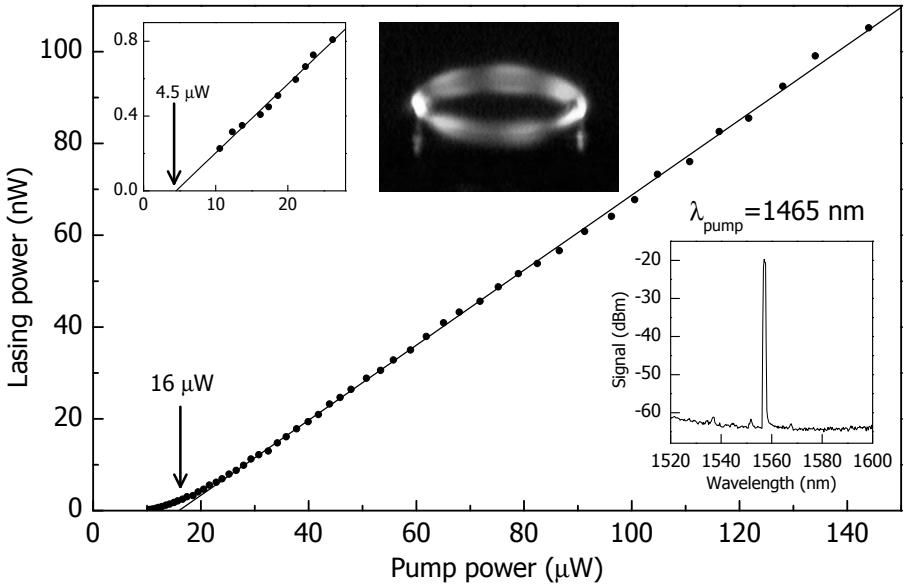

Figure 7.13: Lasing power versus launched pump power measured for a pre-implanted microtoroid. The lasing threshold is 16 μW. The inset on the right bottom shows a single mode lasing spectrum measured under 1465 nm pumping. The inset on the far left shows the lasing power versus the launched power for a microtoroid with a threshold of 4.5 μW. The second inset on the left shows a green Er upconversion luminescence image (printed in black and white) taken under an oblique angle when pumped at high power.

are dominated by Er absorption for both types of microtoroids. Enhanced Er PL peaks are observed superimposed on the Er emission spectrum. They are attributed to coupling to cavity modes. Er lasing at 1.5 μm was observed for post-implanted and pre-implanted microtoroids. Due to a larger overlap and a smaller mode volume the lowest lasing thresholds were observed for pre-implanted microtoroids (4.5 μW). Lower lasing thresholds are expected for microtoroids with reduced diameter and lower Er concentration.

Part III

Controlled spontaneous emission in Si-infiltrated silica colloidal photonic crystals

Chapter 8

Selective excitation of erbium in silicon-infiltrated silica colloidal photonic crystals

Optically active erbium ions in the silica and silicon sections of a Si-infiltrated silica colloidal photonic crystal can be separately addressed. A face-centered cubic colloidal crystal composed of 860 nm diameter silica colloids was made by self-assembly under controlled drying conditions. It was then infiltrated with Si using chemical vapor deposition at 550 ^{o}C. Next, the photonic crystal was doped with erbium ions by 2 MeV ion implantation. The erbium ions were activated by thermal anneals at 400 and 750 ^{o}C and showed clear photoluminescence at 1.5 μm in both the Si and silica parts of the photonic crystal. By varying measurement temperature and excitation wavelength, the erbium ions were selectively excited in Si and/or silica. In this way the local photonic density of states in these photonic crystals can be selectively probed. The emission linewidth for Er^{3+} in crystalline Si is relatively narrow and fits well within the calculated photonic bandgap of a Si-inverse opal photonic crystal. The long luminescence lifetime of Er in Si makes these photonic crystals an ideal geometry to measure effects of the optical density of states on spontaneous emission.

8.1 Introduction

The spontaneous emission rate of an atom is not only a property of the atom, but also depends on the density of states (DOS), a property determined by the atom's dielectric environment.[95][7] Recently, with the introduction of the concept of photonic crystals (PCs),[96][97][98] it has been predicted that it will be possible to make materials with a photonic band gap (PBG). Photonic crystals are materials that consist of a regular arrangement of dielectric material that interact strongly with light. When properly designed, a PC can exhibit a frequency range where, for all wave vectors, the DOS vanishes and no electromagnetic modes are allowed (see Fig. 1.4). If the emission frequency of an atom falls within such a forbidden frequency range (the photonic band gap) the spontaneous emission is completely inhibited. It is a great challenge to fabricate these PCs with a PBG at optical and near-infrared frequencies, and to show a significant effect on the spontaneous emission rate. So far, no large effect on the spontaneous emission rate has been demonstrated in PCs. In several studies on spontaneous emission the PCs do not possess high-enough refractive-index contrast to have a PBG.[39][41] In another study,[40] for a Si PC, which does posses high-enough index contrast, a large change in the spontaneous emission spectrum was achieved, but the crystal was too thin to observe a large effect on the emission rate.

In this chapter we present the fabrication of an erbium-doped face-centered cubic (fcc) Si-inverted opal PC that has high-enough index contrast and sufficient thickness so that the effect of the PBG on the spontaneous emission may be observed. To fabricate this structure, a crystal is grown from silica colloids by self-assembly. The colloidal crystal is then infiltrated, after which the colloids are removed, so that an air-sphere crystal remains. This concept was demonstrated for infiltration with TiO_2,[99][100] and recently, infiltration with Si was demonstrated.[101][102] An air-sphere opal, with fcc symmetry, fully infiltrated with Si has a PBG between the eighth and ninth band of 4.25 % of the center frequency (see Fig. 1.4), the latter being determined by the crystal's lattice parameter. Structures that are not fully infiltrated can posses band gaps that are even larger, up to 8 %.[10] Recently, a technique was developed in which large-area colloidal crystals were grown on a Si substrate.[102] The planar geometry of these crystals makes it possible to use thin-film techniques such as ion implantation to incorporate optical dopants into the PC.

We use Er ions as optical probes in a Si-infiltrated silica colloidal crystal. Erbium is a rare-earth atom that takes on a trivalent state in a solid, and shows intra-4f transitions at 1.53 μm. The use of Er as an optical probe has several advantages over dyes; Er shows a narrow emission linewidth and it does not photobleach, a problem frequently encountered with dyes. When incorporated in either Si or silica, Er can be made optically active by thermal annealing. The 1.53 μm Er emission energy is smaller than the Si band-edge energy, and therefore, the Si host does not absorb the Er emission. After etching out the silica colloids, the index contrast increases [at 1.53 μm, n=3.5 (crystalline Si) and n=3.59 (amorphous Si)] and a PC is made that, according

to calculations,[10] has a PBG. The goal of this chapter is to demonstrate the fabrication of an Er-doped fcc Si-inverted opal PC and to investigate the intrinsic optical properties of such a crystal. We do so by fabricating a PC with a PBG that does not overlap with the Er emission spectrum and dope only the near-surface region of the PC, so that photonic effects on the Er emission are small. These data serve as a reference for future experiments where Er is placed inside a PC with a PBG at 1.5 μm. In our experiments Er is optically activated in both Si and silica host materials, and, by changing the experimental conditions, Er ions can be selectively excited in Si and/or silica. We find that the Er emission linewidth matches well with the PBG calculated for an fcc Si-inverted opal with the proper lattice constant.

8.2 Fabrication, structural and optical characterization

We used the Stöber method [103] to grow silica colloids from tetra-ethoxy-silane (TEOS). Small-size nuclei were grown first, and subsequently their diameter was increased to 860 nm by adding, under well-controlled conditions, additional TEOS to the solution.[104] The amount of dumbbells in the solution was below 1 %, and the resulting size polydispersity was 2.5 %. By controlled drying,[105] a colloidal crystal was grown on a Si substrate that was mounted at an angle of 80^o in a vial, filled with a 1 vol.% colloidal suspension. The solvent evaporated by keeping the vial at 70 ^{o}C in a hot-air oven. The capillary forces at the retreating meniscus causes the self-assembly of an fcc colloidal crystal on the Si substrate. We investigated the colloidal crystal quality with scanning electron microscopy (SEM) and observed a maximum domain size of $\sim$100 μm and a crystal thickness of $\sim$15 layers of colloids. Figure 8.1(a) shows the fcc (111) surface plane of the colloidal crystal after self-assembly by controlled drying. The inset shows the Fourier transform of an image covering an area of 100 μm $\times$ 60 μm, demonstrating the long-range order we achieved for these samples.

The colloidal crystals were infiltrated with Si by means of low-pressure chemical-vapor deposition (CVD) with silane.[102] The samples were heated to 550 ^{o}C and, over the course of 3 hours, infiltrated with Si while the silane pressure, and gas-flow rate, were kept at 743 mTorr and 90 sccm, respectively. The infiltration resulted in an almost complete filling of the interstices of the colloidal crystal with amorphous-Si (a-Si) and the deposition of an a-Si layer on top of the crystal. The a-Si top layer was removed using an SF_6 reactive-ion etch. Since SF_6 etches Si selectively, the silica colloids act as an etch stop for the Si etch. Etching was stopped when the silica colloids were exposed on the surface (see Fig. 8.1(b)).

Next, the samples were implanted with 2.05 MeV Er^{2+} ions, resulting in a Gaussian depth distribution. The implanted fluence was measured on a Si reference sample by Rutherford backscattering spectrometry and amounted to $2.5{\cdot}10^{14}$ Er/cm^2. Note that the erbium ions are distributed in both the Si

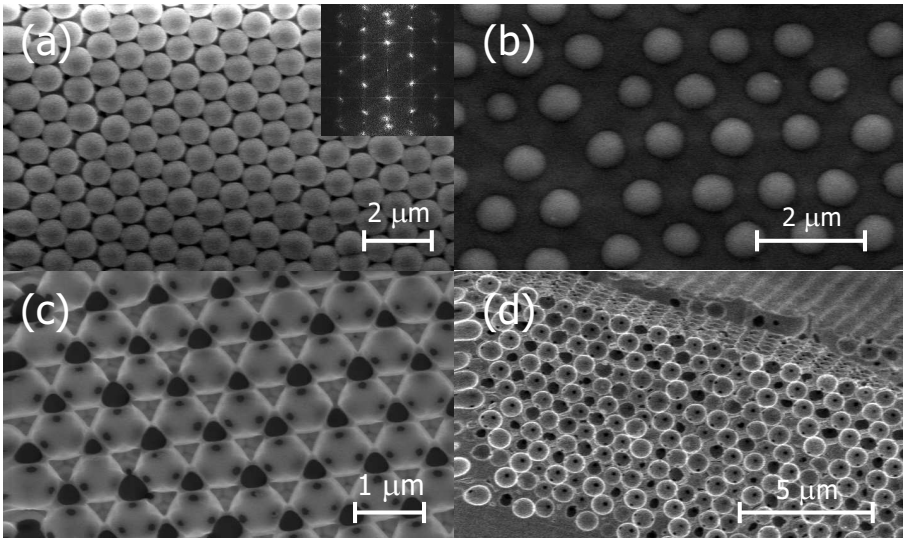

Figure 8.1: SEM micrographs of the various stages in the fabrication process of the Si-inverted opal PC; (a) fcc (111) plane at the top of the colloidal crystal, which was grown by controlled drying. The inset shows the Fourier transform of a large-area image, indicating long-range crystal order, (b) Si infiltration and dry etching results in a well-defined crystal plane on top of the crystal, (c) same top view, but after HF etching, which creates the inverted-opal structure by etching out the silica all the way to the substrate. (d) fcc $(1\bar{1}0)$ plane of the same sample, showing the cross-section of the crystal. Note the almost complete filling of the interstices of the original colloidal crystal.

and the silica part of the PC. The ion range and straggle for this implantation energy are μ=640 nm, σ=128 nm for Si, and μ=533 nm, σ=106 nm for colloidal silica, respectively. To increase the index contrast, and thus create a PC with a PBG, the silica was etched out by immersing the sample in a 5.5 wt.% buffered HF solution for 8 min (solution buffered with NH_4F). Figure 8.1(c) shows a top view of the etched sample. The small holes in the air spheres are the points where the silica colloids originally touched. This connectedness of the air network is first of all essential in order for the reaction products to be able to leave the sample. Moreover, it leads to a larger bandgap.[106] On a larger scale than shown in Fig. 8.1(c) cracks are visible that are the result of shrinkage of the colloids during Si infiltration. These cracks are filled with Si. The typical domain size after infiltration is $\sim$20 μm. Figure 8.1(d) shows a view of the $(1\bar{1}0)$ lattice plane after cleaving. It shows that the crystallinity is maintained through the full cross section of the crystal. Also, it can be seen that the silica colloids were etched out all the way through to the bottom of the sample.

The experiments described next were done with the following equipment. Raman spectroscopy was done with a confocal microscope equipped with a su-

per notch filter, in combination with a fiber-coupled 532 nm frequency-doubled Nd-YAG laser. Optical transmission measurements were done using a Woollam variable-angle spectroscopic ellipsometer. Temperature-dependent infrared photoluminescence (PL) spectroscopy measurements were done by mounting the samples in a closed-cycle He cryostat. The Er^{3+} ions were excited with an acousto-optically time-modulated Ar-ion laser, operated at a power of 10 mW. PL was collected with an f=15 cm lens, dispersed with a 480 mm focal-length monochromator, and detected with a liquid-nitrogen-cooled Ge detector in combination with a lock-in amplifier. Decay and excitation rates were obtained by averaging the time-dependent PL signal, after switching the laser beam off and on, respectively.

8.3 Results and discussion

We made spectrally resolved far-field optical reflectivity measurements (not shown), with the incident beam under an angle of 17^o with respect to the surface normal, to investigate the optical properties of the Si-inverted opal PC with the silica etched out. The as-deposited sample showed peaks at 1600 and 1200 nm, attributed to stopgaps between the fourth and the fifth band, and the eighth and ninth band respectively. The reflectivity spectra showed peak reflectivities on the order of 6-8 %, well below the values close to 100 % observed earlier on a similar crystal.[107] This is attributed to the fact that in these par-

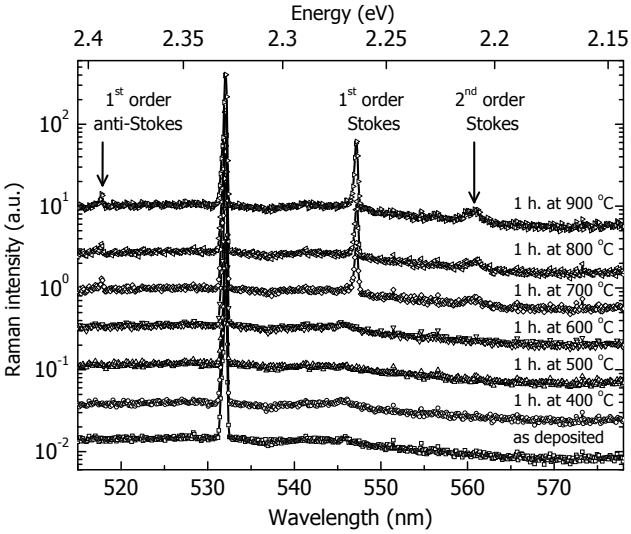

Figure 8.2: Raman spectra for the CVD-deposited reference sample annealed at various temperatures (indicated on the right). The laser line is at 532 nm. At anneal temperatures above 600 ^{o}C Stokes and anti-Stokes Raman lines can be observed indicating the crystallization of the Si.

ticular samples the presence of multiple domains and grain boundaries reduces the specular reflectivity. Note that effects on spontaneous emission, in these photonic crystals with relatively high index contrast, are mostly determined by medium- and short-range order in the crystal and thus large-scale disorder should not be considered a major problem in studies on modified spontaneous emission. Upon annealing at 750 ^{o}C the peaks shifted to smaller wavelengths. This is attributed to the crystallization of the Si that was initially deposited in its amorphous state, as follows from Raman scattering measurements on a Si reference sample.

Figure 8.2 shows Raman spectra of the CVD deposited Si sample after annealing at various temperatures, vertically shifted for comparison. Clearly, when the anneal temperature exceeds 600 ^{o}C, Stokes and anti-Stokes Raman lines appear. The magnitude of the Stokes shift corresponds to the k=0 phonon energy of crystalline Si,[108] and thus shows crystallization of the a-Si. The amorphous → crystalline transition also leads to a change of refractive index as was determined from optical transmission measurements on the same Si reference sample.

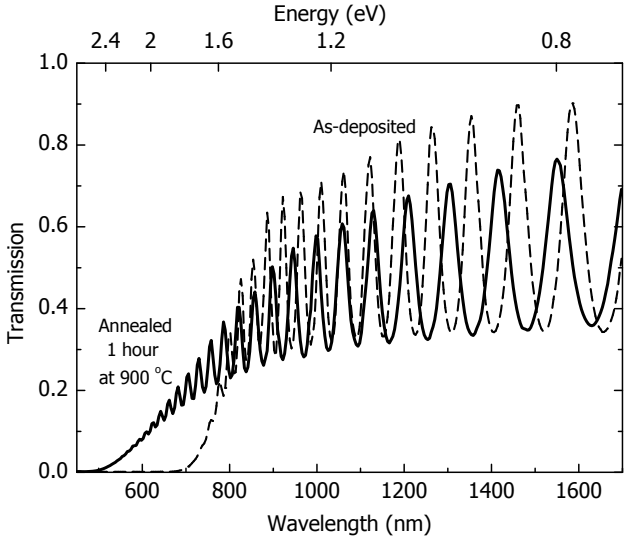

Figure 8.3: Optical transmission measurements on the CVD-deposited Si reference sample, as deposited (dashed line) and after an anneal for one hour at 900 ^{o}C (solid line).

Figure 8.3 shows a transmission measurement of the as-deposited sample (dashed line) and the sample after a one-hour anneal at 900 ^{o}C (solid line). Two features can be observed. First, the transmission edge of the annealed sample shifts from ∼700 nm for the amorphous sample to ∼500 nm after crystallization. This reflects the smaller electronic bandgap of crystalline Si with respect to a-Si, and the absence of absorbing tail states usually observed in a-Si.

Second, the interference fringes, which are caused by Fabry-Perot oscillations in the transmitted intensity of the Si layer, become less closely spaced. This shows that the refractive index decreases upon annealing.[109][110] The fringe amplitude was used to determine the refractive index of the Si layer at λ=1530 nm.[111] The refractive index was 3.66 for as-deposited a-Si and decreased to 3.59 after annealing for one hour at 500 ^{o}C. This reduction is attributed to structural relaxation of the amorphous Si network. An anneal at 900 ^{o}C for one hour resulted in a refractive index of 3.5. Note that by carefully tuning the refractive index using anneal temperatures in the range of 700-900 ^{o}C, we can to some extent shift the PBG of the Si-inverted opal to exactly match the Er emission spectrum.

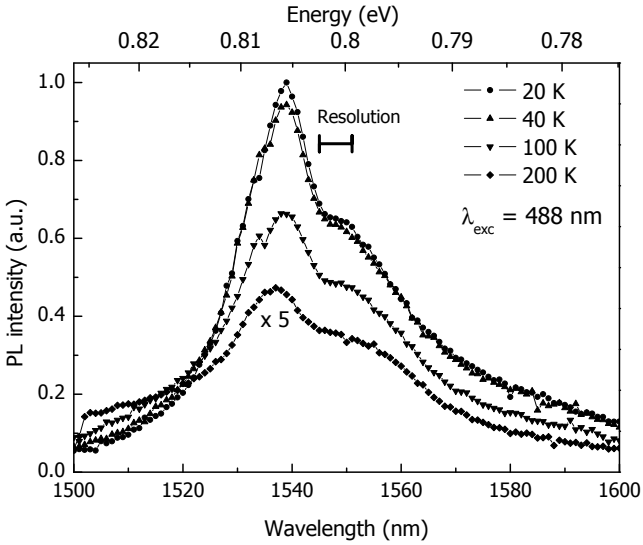

Figure 8.4: PL spectra of an Er-implanted Si-infiltrated colloidal crystal after annealing at 400 ^{o}C. Spectra are taken at different temperatures. The broad spectrum and the PL quenching with increasing temperature are characteristic features for Er in a-Si. Excitation wavelength is 488 nm.

To characterize optically active Er^{3+} ions in a-Si we annealed an Er-implanted Si-infiltrated colloidal crystal (silica not etched out) for one hour at 400 ^{o}C in vacuum. Figure 8.4 shows the PL spectra, taken at temperatures in the range of 20-200 K under excitation at λ=488 nm. A broad emission spectrum, with a full width at half-maximum (FWHM) of 29 nm, can be observed, a feature that is mainly caused by inhomogeneous broadening due to the varying nearest-neighbor surrounding of the Er^{3+} ions in the amorphous Si matrix. The PL peak intensity quenched by a factor of 10 when the temperature increased from 20 to 200 K. Time-dependent PL measurements of the decay rate were performed, and showed a 1/e decay time of 300 μs, independent of PL temperature.

PL decay measurements did not show any contribution from Er^{3+} in sil-

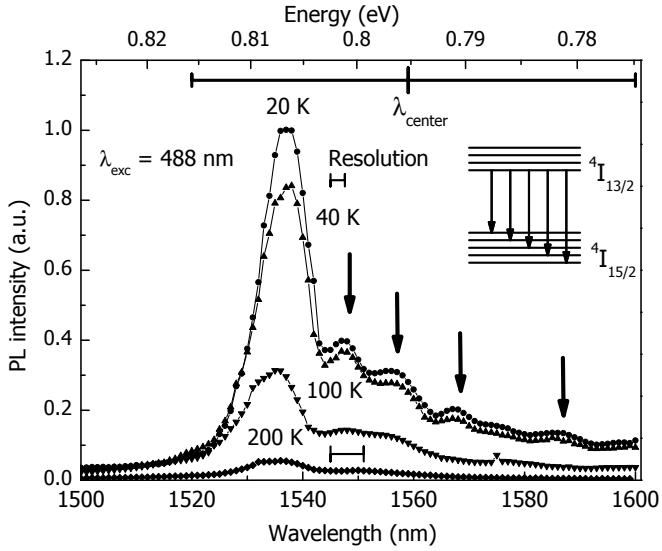

Figure 8.5: PL spectra of an Er-implanted Si-infiltrated colloidal crystal after annealing at 750 ^{o}C (resolution for 20 and 40 K, 2.6 nm, other temperatures 6 nm, see resolution bars). The excitation wavelength was 488 nm. The PL spectra at 20 and 40 K show Stark splitting due to the crystal field of c-Si, as indicated by the arrows. The inset shows a schematic of the Stark splitting of the energy levels and transitions that result in the observed spectral shape. The PL intensity decreases for increasing temperature. This is ascribed to a de-trapping process that reduces the excitation efficiency. The scale bar on top shows the calculated wavelength range of the PBG for an fcc Si-inverted opal PC with a lattice parameter of 1237 nm.

ica (for which a lifetime in the millisecond range is expected [112]), which is consistent with earlier work that showed that activation of Er^{3+} in silica colloids occurs only for anneal temperatures above 700 ^{o}C.[112] As has been seen before,[113] Er^{3+} in a-Si can be optically excited at energies larger than the electronic a-Si band edge energy. The photogenerated carriers can become trapped at an erbium-related trapping site, where they recombine and induce excitation of the Er^{3+} ions through an impurity-Auger process. Quenching of the PL intensity with temperature can occur as a result of a reduced excitation efficiency, or due to backtransfer, which is the transfer of energy from an excited Er^{3+} ion back to the trapping site.[66][22] The fact that the PL lifetime is temperature independent indicates that the decrease in PL with increasing temperature is not due to backtransfer. We note that earlier work [114] has shown that Er^{3+} shows no PL in pure a-Si. Later work [113] has shown that passivation of defects by hydrogen, and the presence of small amounts of oxygen, are essential to activate Er^{3+}. We can therefore conclude that the CVD infiltration process includes these impurities in the a-Si matrix.

Next, we investigate the quenching and excitation mechanisms of Er^{3+} in

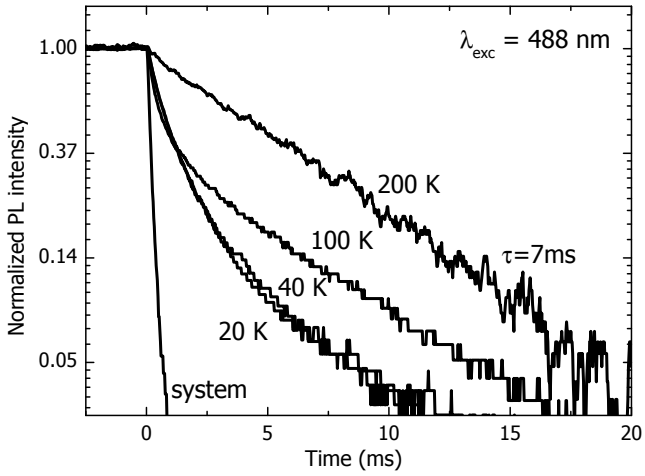

Figure 8.6: Normalized PL decay measurements, taken at 1536 nm at different temperatures (see for spectra Fig. 8.5). After excitation at 488 nm the laser is switched of at t=0. The PL decay measurements at 20 and 40 K are composed of PL from Er^{3+} in Si (fast decay) and Er^{3+} in silica (slow decay). For higher temperatures the PL of Er^{3+} in Si quenches and the PL contribution from Er^{3+} in silica remains.

a Si-infiltrated colloidal crystal annealed for 1 hour at 750 ^{o}C, which leads to the crystallization of a-Si and optical activation of Er^{3+} in silica. Figure 8.5 shows the PL spectra of this sample, measured at temperatures in the range of 20-200 K, and excited at a wavelength of 488 nm. Again, strong PL quenching with increasing temperature is observed, a known effect for Er^{3+} in crystalline Si (c-Si).[65] For the measurements at 20 and 40 K, a narrow main emission peak is observed (FWHM=11 nm). Moreover, several pronounced peaks, indicated by arrows, can be seen in the PL spectra. This structure is caused by Stark splitting of degenerate 4f-energy levels of Er^{3+}, due to the crystal field around the atom.[115] The asymmetry in the spectrum is caused by the fact that at these measurement temperatures only the lowest level in the first excited state manifold ($^4I_{13/2}$) is populated. Therefore, only emission lines at the long-wavelength side of the main emission peak are observed. From the observation of the Stark levels, we can assume that the Er^{3+} ions are in a crystalline environment, in agreement with the Raman data in Fig. 8.2.

In these experiments an excitation wavelength of 488 nm was chosen, which causes excitation of Er^{3+} in silica by direct optical excitation into the $^4F_{7/2}$ manifold, and in c-Si by a photocarriers mediated process. To determine the relative PL contribution of Er^{3+} from either one of the host materials, we measured the time-dependent PL decay at 1536 nm for temperatures in the

Origin of PL	PL temperature	Excitation wavelength
Er^{3+} in c-Si	low (20 K)	indirect, below electronic band gap wavelength (e.g. 457 nm)
Er^{3+} in silica	high (>200 K)	direct (e.g. 488 nm)
Er^{3+} in c-Si and silica	intermediate (100 K)	direct (e.g. 488 nm)

Table 8.1: Conditions for the selective excitation of Er^{3+} in a Si-infiltrated silica colloidal crystal annealed at 750 ^{o}C. Selective excitation can be accomplished by varying the PL temperature and the excitation wavelength.

range of 20-200 K. Figure 8.6 shows normalized PL decay traces. At 200 K the PL decay shows a long lifetime (7 ms), characteristic for Er^{3+} in silica.[5] At this temperature the PL from Er^{3+} in c-Si is fully quenched. The spectrum in Fig. 8.5 measured at 200 K, therefore only originates from Er^{3+} in silica. At lower temperatures a fast PL decay component appears with a lifetime of 0.9 ms, characteristic for Er^{3+} in c-Si.[116] Since this lifetime is similar to the longest lifetime observed for Er-implanted c-Si, it is most likely close to the radiative lifetime. The assumed high quantum efficiency makes this Er-doped Si-inverted opal PC an ideal geometry to measure the effects of the optical DOS on the spontaneous emission lifetime. A biexponential fit to the PL decay at 20 K yields the relative contributions of Er^{3+} in c-Si and silica to the PL: 78 % and 22 %, respectively. As the volume fractions of Si and silica are 26 % and 74 %, respectively, this indicates that for a given pump power PL from Er^{3+} is more efficiently excited in Si than in silica. This is attributed to the large cross section for the generation of photocarriers in c-Si that subsequently couple to Er^{3+}, compared to the relatively small cross section for direct excitation of Er^{3+} in silica.

In order to selectively excite Er^{3+} in either c-Si or silica we can make use of their different excitation and quenching mechanisms. To selectively excite Er^{3+} in c-Si the excitation wavelength can be tuned off resonance from an Er^{3+} absorption line (e.g. 501 nm). In this case Er^{3+} in silica is not excited, while in c-Si photocarriers do excite Er^{3+}. Fig. 8.7 shows normalized time-dependent PL decay measurements at a temperature of 100 K for either direct (488 nm) or indirect excitation (501 nm). At an excitation wavelength of 501 nm we observe only the fast decay of Er^{3+} in c-Si. However, at an excitation wavelength of 488 nm we observe a two-component decay with a fast contribution from Er^{3+} in c-Si and a slow contribution from Er^{3+} in silica. Consequently, by choosing the appropriate excitation wavelength, we can observe PL from Er^{3+} in c-Si only or from Er^{3+} in both c-Si and silica. To measure PL from Er^{3+} in silica only, we can increase the temperature to quench the PL from Er^{3+} in c-Si (see Fig. 8.5). Table 8.1 summarizes the various ways Er^{3+} can be excited selectively in c-Si and/or silica. Eventually, selective excitation will enable us to probe the DOS selectively in either one of these materials.

Variations in the DOS can be measured by comparing Er^{3+} decay rates in fcc Si-inverted opal PCs with different lattice constants. The Er^{3+} spontaneous

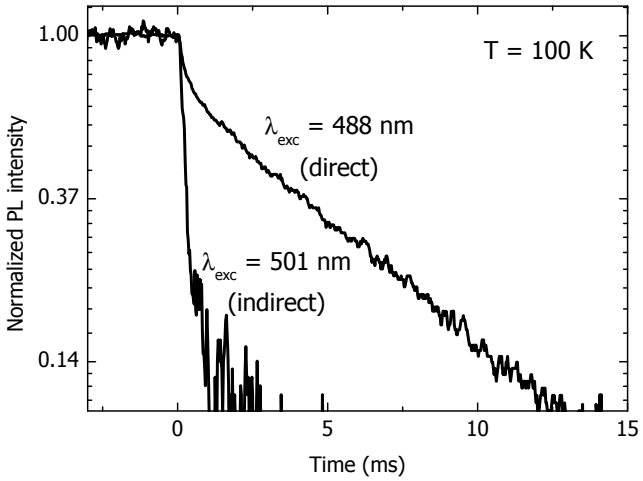

Figure 8.7: Normalized PL decay measurements, taken at 1536 nm and 100 K (see Fig. 8.5) for two different excitation wavelengths. After excitation at 488 nm the laser is switched of at t=0 and the decay curve shows a slow decay contribution from Er^{3+} in silica, together with a fast decay from Er^{3+} in Si. Using indirect excitation (501 nm) only Er^{3+} in Si is excited and the corresponding fast decay component is observed.

emission rate is expected to be fully inhibited in PCs in which the silica is etched out, provided the lattice constant is chosen such that the PBG overlaps with the Er^{3+} emission spectrum, and the Er ions are implanted deep enough into the photonic crystal. From Fig. 8.5 we can now determine design criteria for an fcc Si-inverted opal PC to obtain a large effect on the spontaneous emission rate. If we assume full infiltration and a refractive index of 3.5 at a wavelength of 1.53 μm, the calculated PBG bandwidth is 5 % [10] (80 nm at 1559 nm). Overlap of the PBG with the Er^{3+} emission spectrum is optimal for a center gap frequency at 1559 nm, which is slightly larger than the Er^{3+} peak emission wavelength. The horizontal bar in Fig. 8.5 indicates the overlap of the calculated PBG with the Er^{3+} emission spectrum for the case of Er^{3+} in c-Si for a center wavelength of 1559 nm. The corresponding lattice parameter for an fcc Si inverted opal is a=1237 nm (cubic unit cell), which corresponds to a colloid diameter of 875 nm. It should be noted that the infiltration process often does not lead to a complete Si filling of the interstices within the silica colloidal crystal and, as near-field reflection measurements have shown,[102] this results in an increase of the PBG center frequency. To compensate for this effect, the colloid diameter has to be taken slightly larger, in order to match the PBG with the Er^{3+} emission spectrum. Consequently, precise control over the colloid diameter and refractive index has to be achieved to obtain a PBG that overlaps with the Er^{3+} emission spectrum. However, we note that theoretical work [10] has shown that band gaps for incompletely infiltrated crystals can be

as large as 8 %, which is well beyond the spectral width observed in Fig. 8.5.

8.4 Conclusions

We have shown the successful fabrication of an Er-doped fcc Si-inverted opal PC. By annealing the crystal at 400 ^{o}C, Er^{3+} ions are activated in the a-Si host, but not in silica. An inhomogenously broadened emission spectrum is observed for Er^{3+} in a-Si, with a PL lifetime of 300 μs. After annealing at 750 ^{o}C, Er^{3+} is activated in both Si and silica. The high anneal temperature caused the Si to crystallize and Stark peaks, reflecting the Si crystallization, were observed in the Er^{3+} PL spectrum. Raman spectroscopy also confirmed the crystallization. The PL lifetime of Er^{3+} in c-Si was 0.9 ms, close to the expected radiative lifetime of Er^{3+} in Si. At an anneal temperature of 750 ^{o}C Er^{3+} in silica is also activated, and shows a lifetime of 7 ms. Both in a-Si and c-Si the Er luminescence quenches with increasing temperature. By varying the PL temperature and the excitation wavelength we can selectively excite Er in Si and/or silica. In future experiments this makes it possible to probe the DOS selectively in either one of these materials. For Er^{3+} in crystalline Si the emission linewidth fits well within the calculated PBG bandwidth. These characteristics make these PCs ideally suited for experiments demonstrating the effect of the PBG on the spontaneous emission.

Bibliography

[1] D. A. B. Miller, *Physical reasons for optical interconnection*, Int. J. Optoelectronics **11**, 155 (1997).

[2] E. Knill, R. Laflamme, and G. J. Milburn, *A scheme for efficient quantum computation with linear optics*, Nature **409**, 46 (2001).

[3] R. Loudon, *The quantum theory of light*, Oxford University Press, New York, 2000.

[4] E. Snoeks, A. Lagendijk, and A. Polman, *Measuring and modifying the spontaneous emission rate of erbium near an interface*, Phys. Rev. Lett. **74**, 2459 (1995).

[5] M. J. A. de Dood, L. H. Slooff, A. Moroz, A. van Blaaderen, and A. Polman, *Local optical density of states in SiO_2 spherical microcavities: Theory and experiment*, Phys. Rev. A **64**, 033807 (2001).

[6] G. W. Ford and W. H. Weber, *Electromagnetic interactions of molecules with metal surfaces*, Phys. Rep. **113**, 195 (1984).

[7] E. Purcell, *Spontaneous emission probabilities at radio frequencies*, Phys. Rev. **69**, 681 (1946).

[8] E. V. Goldstein and P. Meystre, *Spontaneous emission in optical cavities: a tutorial review*, in *Spontaneous emission and laser oscillation in microcavities*, ed. by H. Yokoyama and K. Ujihara , 1 (1995).

[9] J. M. Gérard, B. Sernage, B. Gayral, B. Legrand, E. Costard, and V. Thierry-Mieg, *Enhanced spontaneous emission by quantum boxes in a monolithic optical microcavity*, Phys. Rev. Lett. **81**, 1110 (1998).

[10] K. Busch and S. John, *Photonic band gap formation in certain self-organizing systems*, Phys. Rev. E **58**, 3896 (1998).

[11] S. G. Johnson and J. D. Joannopoulos, *Block-iterative frequency-domain methods for Maxwell's equations in a planewave basis*, Opt. Lett. **8**, 173 (2001).

[12] H. Raether, *Surface plasmons*, Springer-Verlag, Berlin Heidelberg, 1988.

[13] A. Polman, D. C. Jacobson, D. J. Eaglesham, R. C. Kistler, and J. M. Poate, *Optical doping of waveguide materials by MeV Er implantation*, J. Appl. Phys. **70**, 3778 (1991).

[14] L. Li, *A modal analysis of lamellar diffraction gratings in conical mountings*, J. Mod. Opt. **40**, 553 (1993).

[15] I. Pockrand, *Reflection of light from periodically corrugated silver films near the plasma frequency*, Phys. Lett. **49A**, 259 (1974).

[16] S. C. Kitson, W. L. Barnes, and J. R. Sambles, *Photoluminescence from dye molecules on silver gratings*, Opt. Commun. **122**, 147 (1996).

[17] T. Inagaki, J. P. Goudonnet, and E. T. Arakawa, *Plasma resonance absorption in conical diffraction: effects of groove depth*, J. Opt. Soc. Am. B **3**, 992 (1986).

[18] H. Ditlbacher, J. R. Krenn, G. Schider, A. Leitner, and F. R. Aussenegg, *Two-dimensional optics with surface plasmon polaritons*, Appl. Phys. Lett. **81**, 1762 (2002).

[19] P. Andrew and W. L. Barnes, *Molecular fluorescence above metallic gratings*, Phys. Rev. B **64**, 125405 (2001).

[20] J. Moreland, A. Adams, and P. K. Hansma, *Efficiency of light emission from surface plasmons*, Phys. Rev. B **25**, 2297 (1982).

[21] F. Priolo, G. Franzò, S. Coffa, and A. Carnera, *Excitation and nonradiative deexcitation processes of Er^{3+} in crystalline Si*, Phys. Rev. B **57**, 4443 (1998).

[22] N. Hamelin, P. G. Kik, J. F. Suyver, K. Kikoin, A. Polman, A. Schönecker, and F. W. Saris, *Energy backtransfer and infrared photoresponse in erbium-doped silicon p-n diodes*, J. Appl. Phys. **88**, 5381 (2000).

[23] A. Polman, *Erbium implanted thin film photonic materials*, J. Appl. Phys. **82**, 1 (1997).

[24] J. Kalkman, C. Strohhöfer, B. Gralak, and A. Polman, *Surface plasmon polariton modified emission of erbium in a metallodielectric grating*, Appl. Phys. Lett. **83**, 30 (2003).

[25] P. G. de Gennes, *Sur la relaxation nucleaire dans les cristaux ioniques*, J. Phys. Chem. Solids **7**, 345 (1958).

[26] M. J. Weber, *Luminescence decay by energy migration and transfer: Observation of diffusion-limited relaxation*, Phys. Rev. B **4**, 2932 (1971).

[27] W. L. Barnes, *Fluorescence near interfaces: the role of photonic mode density*, J. Mod. Opt. **45**, 661 (1998).

[28] W. H. Weber and C. F. Eagen, *Energy transfer from an excited dye molecule to the surface plasmons of an adjacent metal*, Opt. Lett. **4**, 236 (1979).

[29] K. H. Drexhage, *Influence of a dielectric interface on fluorescence decay time*, J. Lumin. **1,2**, 693 (1970).

[30] R. M. Amos and W. L. Barnes, *Modification of the spontaneous emission rate of Eu^{3+} ions close to a thin metal mirror*, Phys. Rev. B **55**, 7249 (1997).

[31] H. Morawitz and M. R. Philpott, *Coupling of an excited molecule to surface plasmons*, Phys. Rev. B **10**, 4863 (1974).

[32] K. S. Min, K. V. Shcheglov, C. M. Yang, H. A. Atwater, M. L. Brongersma, and A. Polman, *Defect-related versus excitonic visible light emission from ion beam synthesized Si nanocrystals in SiO_2*, Appl. Phys. Lett. **69**, 2033 (1996).

[33] A. Irrera, D. Pacifici, M. Miritello, G. Franzò, F. Priolo, F. Iacona, D. Sanfilippo, G. D. Stefano, and P. G. Fallica, *Excitation and de-excitation properties of silicon quantum dots under electrical pumping*, Appl. Phys. Lett. **81**, 1866 (2002).

[34] J. Valenta, N. Lalic, and J. Linnros, *Electroluminescence of single silicon nanocrystals*, Appl. Phys. Lett. **84**, 1459 (2004).

[35] R. J. Walters, P. G. Kik, J. D. Casperson, H. A. Atwater, R. Lindstedt, M. Giorgi, and G. Bourianoff, *Silicon optical nanocrystal memory*, Appl. Phys. Lett. **85**, 2622 (2004).

[36] L. Pavesi, L. D. Negro, C. Mazzoleni, G. Franzò, and F. Priolo, *Optical gain in silicon nanocrystals*, Nature **408**, 440 (2000).

[37] R. Sprik, B. A. van Tiggelen, and A. Lagendijk, *Optical emission in periodic dielectrics*, Europhys. Lett. **35**, 265 (1996).

[38] T. M. Hensen, M. J. A. de Dood, and A. Polman, *Luminescence quantum efficiency and local optical density of states in thin film ruby made by ion implantation*, J. Appl. Phys. **88**, 5142 (2000).

[39] A. F. Koenderink, L. Bechger, H. P. Schriemer, A. Lagendijk, and W. L. Vos, *Broadband fivefold reduction of vacuum fluctuations probed by dyes in photonic crystals*, Phys. Rev. Lett. **88**, 143903 (2002).

[40] M. J. A. de Dood, A. Polman, and J. G. Fleming, *Modified spontaneous emission from erbium-doped photonic layer-by-layer crystals*, Phys. Rev. B **67**, 115106 (2003).

[41] P. Lodahl, A. F. van Driel, I. S. Nikolaev, A. Irman, K. Overgaag, D. Vanmaekelbergh, and W. L. Vos, *Controling the dynamics of spontaneous emission from quantum dots by photonic crystals*, Nature **430**, 654 (2004).

[42] J. F. Ziegler, J. P. Biersack, and U. Littmark, *The stopping and range of ions in solids*, Pergamon Press, New York, 1985.

[43] M. L. Brongersma, A. Polman, K. S. Min, E. Boer, T. Tambo, and H. A. Atwater, *Tuning the emission wavelength of Si nanocrystals in SiO_2 by oxidation*, Appl. Phys. Lett. **72**, 2577 (1998).

[44] J. Linnros, N. Lalic, A. Galeckas, and V. Grivickas, *Analysis of the stretched exponential photoluminescence decay from nanometer-sized silicon crystals in SiO_2*, J. Appl. Phys. **86**, 6128 (1999).

[45] F. Priolo, G. Franzò, D. Pacifici, V. Vinciguerra, F. Iacona, and A. Irrera, *Role of the energy transfer in the optical properties of undoped and Er-doped interacting Si nanocrystals*, J. Appl. Phys. **89**, 264 (2001).

[46] J. Valenta, R. Juhasz, and J. Linnros, *Photoluminescence spectroscopy of single silicon quantum dots*, Appl. Phys. Lett. **80**, 1070 (2002).

[47] E. Helfand, *On inversion of the Williams-Watts function for large relaxation times*, J. Chem. Phys. **78**, 1931 (1983).

[48] G. Mauckner, K. Thonke, T. Baier, T. Walter, and R. Sauer, *Temperature-dependent lifetime distribution of the photoluminescence S-band in porous silicon*, J. Appl. Phys. **75**, 4167 (1994).

[49] C. P. Lindsey and G. D. Patterson, *Detailed comparison of the Williams-Watts and Cole-Davidson functions*, J. Chem. Phys. **73**, 3348 (1980).

[50] H. Pollard, *The representation of e^{-x^λ} as a Laplace integral*, Bull. Am. Math. Soc. **52**, 908 (1946).

[51] D. Kovalev, H. Heckler, G. Polisski, J. Diener, and F. Koch, *Optical properties of silicon nanocrystals*, Opt. Mat. **17**, 35 (2001).

[52] C. Garcia, B. Garrido, P. Pellegrino, R. Ferre, J. A. Moreno, J. R. Morante, L. Pavesi, and M. Cazzanelli, *Size dependence of lifetime and absorption cross section of Si nanocrystals embedded in SiO_2*, Appl. Phys. Lett. **82**, 1595 (2003).

[53] M. V. Wolkin, J. Jorne, P. M. Fauchet, G. Allan, and C. Delerue, *Electronic states and luminescence in porous silicon quantum dots: the role of oxygen*, Phys. Rev. Lett. **82**, 197 (1999).

[54] M. L. Brongersma, A. Polman, K. S. Min, and H. A. Atwater, *Depth distribution of luminescent Si nanocrystals in Si implanted SiO_2 films on Si*, J. Appl. Phys. **86**, 759 (1999).

[55] J. A. Dionne, L. A. Sweatlock, H. A. Atwater, and A. Polman, *Planar metal plasmon waveguides: frequency-dependent dispersion, propagation, localization, and loss beyond the free electron-model*, submitted to Phys. Rev. B .

[56] I. Gontijo, M. Boroditsky, E. Yablonovitch, S. Keller, U. K. Mishra, and S. P. DenBaars, *Coupling of InGaN quantum-well photoluminescence to silver surface plasmons*, Phys. Rev. B **60**, 11564 (1999).

[57] J. Woolam, *Optical constants of Si, various data sets.*

[58] R. C. Weast, D. R. Lide, M. J. Astle, and W. H. Beyer, *CRC Handbook of physics and chemistry, 70^{th} edition*, CRC press Inc., Boca Raton, Florida, 1989.

[59] T. Nikolajsen, K. Leosson, and S. Bozhevolnyi, *Surface plasmon polariton based modulators and switches operating at telecom wavelengths*, Appl. Phys. Lett. **85**, 5833 (2004).

[60] S. Coffa, G. Franzó, and F. Priolo, *High efficiency and fast modulation of Er-dpoed light emitting Si diodes*, Appl. Phys. Lett. **69**, 2077 (1996).

[61] M. Markman, A. Sticht, F. Bobe, G. Zandler, K. Brunner, G. Abstreiter, and E. Müller, *Efficient light emission at 1.54 μm from Er in Si excited by hot electron injection through thin suboxide layers*, J. Appl. Phys. **91**, 9764 (2002).

[62] M. E. Castagna, S. Coffa, M. Monaco, A. Muscara, L. Caristia, S. Lorenti, and A. Messina, *High efficiency light emitting devices in silicon*, Mat. Sci. Eng. B **105**, 83 (2003).

[63] P. Berini, *Plasmon-polariton modes guided by a metal film of finite width*, Opt. Lett. **24**, 1011 (1999).

[64] M. I. Stockman, *Nanofocussing of optical energy in tapered plasmonic waveguides*, Phys. Rev. Lett. **93**, 137404 (2004).

[65] S. Coffa, G. Franzó, F. Priolo, A. Polman, and R. Serna, *Temperature dependence and quenching processes of the intra-4f luminescence of Er in crystalline Si*, Phys. Rev. B **49**, 16313 (1994).

[66] P. G. Kik, M. J. A. de Dood, K. Kikoin, and A. Polman, *Excitation and deexcitation of Er^{3+} in crystalline silicon*, Appl. Phys. Lett. **70**, 1721 (1997).

[67] K. J. Vahala, *Optical microcavities*, Nature **424**, 839 (2003).

[68] V. B. Braginsky, M. L. Gorodetsky, and V. S. Ilchenko, *Quality-factor and nonlinear properties of optical whispering-gallery modes*, Phys. Lett. A **137**, 393 (1989).

[69] D. W. Vernooy, V. S. Ilchenko, H. Mabuchi, E. W. Streed, and H. J. Kimble, *High-Q measurements of fused-silica microspheres in the near infrared*, Opt. Lett. **23**, 247 (1998).

[70] M. Cai, O. Painter, K. J. Vahala, and P. C. Sercel, *Fiber-coupled microsphere laser*, Opt. Lett. **25**, 1430 (2000).

[71] L. Yang and K. J. Vahala, *Gain functionalization of silica microresonators*, Opt. Lett. **28**, 592 (2003).

[72] E. Snoeks, A. van Blaaderen, C. M. van Kats, M. L. Brongersma, T. van Dillen, and A. Polman, *Colloidal ellipsoids with continuously variable whape*, Adv. Mater. **12**, 1511 (2000).

[73] S. M. Spillane, T. J. Kippenberg, O. J. Painter, and K. J. Vahala, *Ideality in a fiber-taper-coupled microresonator system for application to cavity quantum electrodynamics*, Phys. Rev. Lett. **91**, 043902 (2003).

[74] W. J. Miniscalco, *Erbium-doped glasses for fiber amplifiers at 1500 nm*, J. Lightwave Technol. **9**, 234 (1991).

[75] T. J. Kippenberg, S. M. Spillane, and K. J. Vahala, *Modal coupling in traveling-wave resonators*, Opt. Lett. **27**, 1669 (2002).

[76] B. Min, T. J. Kippenberg, L. Yang, K. J. Vahala, J. Kalkman, and A. Polman, *Erbium-implanted high-Q silica toroidal microcavity laser on a silicon chip*, Phys. Rev. A **70**, 033803 (2004).

[77] G. N. van den Hoven, E. Snoeks, A. Polman, C. van Dam, J. W. M. van Uffelen, and M. K. Smit, *Upconversion in Er-implanted Al_2O_3 waveguides*, J. Appl. Phys. **79**, 1258 (1996).

[78] G. N. van den Hoven, E. Snoeks, A. Polman, C. van Dam, J. W. M. van Uffelen, and M. K. Smit, *Direct imaging of optical interference in erbium-doped Al_2O_3 waveguides*, Opt. Lett. **21**, 576 (1996).

[79] A. Polman, B. Min, J. Kalkman, T. J. Kippenberg, and K. J. Vahala, *Ultralow-threshold erbium-implanted toroidal microlaser on silicon*, Appl. Phys. Lett. **84**, 1037 (2004).

[80] M. T. Hill, H. J. S. Dorren, T. de Vries, X. J. M. Leijtens, J. H. den Besten, B. Smalbrugge, Y. Oei, H. Binsma, G. Khoe, and M. K. Smit, *A fast low-power optical memory based on coupled micro-ring lasers*, Nature **432**, 206 (2004).

[81] P. Rabiei, W. H. Steier, C. Zhang, and L. R. Dalton, *Polymer micro-ring filters and modulators*, J. Lightwave Technol. **20**, 1968 (2002).

[82] K. Srinivasan, P. E. Barclay, O. Painter, J. Chen, A. Y. Cho, and C. Gmachl, *Experimental demonstration of a high quality factor photonic crystal microcavity*, Appl. Phys. Lett. **83**, 1915 (2003).

[83] V. Sandoghdar, F. Treussart, J. Hare, V. Lefèvre-Seguin, J. M. Raimond, and S. Haroche, *Very low threshold whispering-gallery-mode microsphere laser*, Phys. Rev. A **54**, R1777 (1996).

[84] D. K. Armani, T. J. Kippenberg, S. M. Spillane, and K. J. Vahala, *Ultra-high-Q toroid microcavity on a chip*, Nature **421**, 925 (2003).

[85] T. J. Kippenberg, S. M. Spillane, D. K. Armani, and K. J. Vahala, *Ultralow-threshold microcavity Raman laser on a microelectronic chip*, Opt. Lett. **29**, 1224 (2004).

[86] T. J. Kippenberg, S. M. Spillane, and K. J. Vahala, *Kerr-nonlinearity optical parametric oscillation in an ultrahigh-Q toroid microcavity*, Phys. Rev. Lett. **93**, 083904 (2004).

[87] M. Fujii, M. Yoshida, Y. Kanzawa, S. Hayashi, and K. Yamamoto, *1.54 μm photoluminescence of Er^{3+} doped into SiO_2 films containing Si nanocrystals: Evidence for energy transfer from Si nanocrystals to Er^{3+}*, Appl. Phys. Lett. **71**, 1198 (1997).

[88] H. A. Haus, *Waves and fields in optoelectronics*, Prentice-Hall, Englewood Cliffs, 1984.

[89] J. C. Knight, G. Cheung, F. Jacques, and T. A. Birks, *Phase-matched excitation of whispering-gallery-mode resonances by a fiber taper*, Opt. Lett. **22**, 1129 (1997).

[90] T. van Dillen, A. Polman, C. M. van Kats, and A. van Blaaderen, *Ion beam-induced anisotropic plastic deformation at 300 keV*, Appl. Phys. Lett. **83**, 4315 (2003).

[91] S. R. Bickham and M. B. Cain, *Submarine fiber*, in *Undersea fiber communications systems*, ed. by J. Chesnoy , 435 (2002).

[92] S. M. Spillane, T. J. Kippenberg, K. J. Vahala, K. W. Goh, E. Wilcut, and H. J. Kimble, *Ultra-high-Q toroidal microresonators for cavity quantum electrodynamics*, Phys. Rev. A **71**, 013817 (2005).

[93] P. C. Becker, N. A. Olsson, and J. R. Simpson, *Erbium-Doped Fiber Amplifiers: Fundamentals and Technology*, Academic Press, San Diego, 1997.

[94] E. Snoeks, G. N. van den Hoven, A. Polman, B. Hendriksen, M. B. J. Diemeer, and F. Priolo, *Cooperative upconversion in erbium-implanted soda-lime silicate glass optical waveguides*, J. Opt. Soc. Am. B **12**, 1468 (1995).

[95] E. Fermi, *Quantum theory of radiation*, Rev. Mod. Phys. **4**, 87 (1932).

[96] V. P. Bykov, *Spontaneous emission from a medium with a band spectrum*, Sov. J. Quantum Electron. **4**, 861 (1975).

[97] E. Yablonovitch, *Inhibited spontaneous emission in solid-state physics and electronics*, Phys. Rev. Lett. **58**, 2059 (1987).

[98] S. John, *Strong localization of photons in certain disordered dielectric superlattices*, Phys. Rev. Lett. **58**, 2486 (1987).

[99] A. Imhof and D. J. Pine, *Ordered macroporous materials by emulsion templating*, Nature **389**, 948 (1997).

[100] J. E. G. J. Wijnhoven and W. L. Vos, *Preparation of photonic crystals made of air spheres in titania*, Science **281**, 802 (1998).

[101] A. Blanco, E. Chomski, S. Grabtchak, M. Ibisate, S. John, S. W. Leonard, C. Lopez, F. Meseguer, H. Miguez, J. P. Mondia, G. A. Ozin, O. Toader, and H. M. van Driel, *Large-scale synthesis of a silicon photonic crystal with a complete three-dimensional bandgap near 1.5 micrometres*, Nature **405**, 437 (2000).

[102] Y. A. Vlasov, X. Bo, J. C. Sturm, and D. J. Norris, *On-chip natural assembly of silicon photonic bandgap crystals*, Nature **414**, 289 (2001).

[103] W. Stöber, A. Fink, and E. Bohn, *Controlled growth of monodisperse silica spheres in the micron size range*, J. Colloid Interface Sci. **26**, 62 (1968).

[104] H. Giesche, *Synthesis of monodispersed silica powders II. Controlled growth reaction and continuous production process*, J. Eur. Ceram. Soc. **14**, 205 (1994).

[105] P. Jiang, J. F. Bertone, K. S. Hwang, and V. L. Colvin, *Single-crystal colloidal multilayers of controlled thickness*, Chem. Mater. **11**, 2132 (1999).

[106] M. Doosje, B. J. Hoenders, and J. Knoester, *Photonic bandgap optimization in inverted fcc photonic crystals*, J. Opt. Soc. Am. B **17**, 600 (2000).

[107] Y. A. Vlasov, M. Deutsch, and D. J. Norris, *Single-domain spectroscopy of self-assembled photonic crystals*, Appl. Phys. Lett. **76**, 1627 (2000).

[108] G. Dolling, *Inelastic Scattering of Neutrons in Solids and Liquids, Vol II*, Intern. Atomic Energy Agency, Vienna, 1963.

[109] D. E. Aspnes and A. A. Studna, *Dielectric functions and optical parameters of Si, Ge, GaP, GaAs, GaSb, InP, InAs and InSb from 1.5 to 6 eV*, Phys. Rev. B **27**, 985 (1983).

[110] D. E. Aspnes, A. A. Studna, and E. Kinsbron, *Dielectric properties of heavily doped crystalline and amorphous Si from 1.5 to 6 eV*, Phys. Rev. B **29**, 768 (1984).

[111] J. C. Manificier, J. Gasiot, and J. P. Fillard, *A simple method for the determination of the optical constants n, k and the thickness of a weakly absorbing thin film*, J. Phys. E **9**, 1002 (1976).

[112] L. H. Slooff, M. J. A. de Dood, A. van Blaaderen, and A. Polman, *Erbium-implanted silica colloids with 80 % luminescence quantum efficiency*, Appl. Phys. Lett. **76**, 3682 (2000).

[113] J. H. Shin, R. Serna, G. N. van den Hoven, A. Polman, W. G. J. H. M. van Sark, and A. M. Vredenberg, *Luminescence quenching in erbium-doped hydrogenated amorphous silicon*, Appl. Phys. Lett. **68**, 997 (1996).

[114] J. S. Custer, E. Snoeks, and A. Polman, *Photoluminescence of erbium in amorphous silicon: structural relaxation and optical doping*, Mat. Res. Soc. Symp. Proc. **235**, 51 (1992).

[115] M. J. A. de Dood, P. G. Kik, J. H. Shin, and A. Polman, *Incorporation, excitation and de-excitation of erbium in crystal silicon*, Mater. Res. Soc. Symp. Proc. **422**, 219 (1996).

[116] A. Polman, G. N. van den Hoven, J. S. Custer, J. H. Shin, R. Serna, and P. F. A. Alkemade, *Erbium in crystal silicon: Optical activation, excitation, and concentration limits*, J. Appl. Phys. **77**, 1256 (1995).

About the author

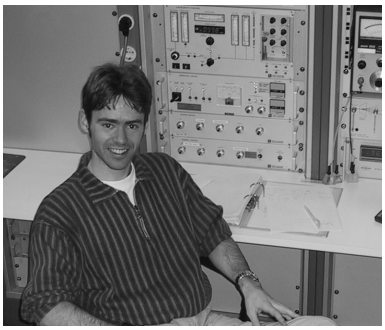

Jeroen Kalkman was born on May the 26^{th} 1975 in Velsen, The Netherlands. He received a VWO degree (pre-university education) in 1993 at the 'oecomenische scholengemeenschap het Baken' in Almere. From 1994 he studied experimental physics at the 'Vrije Universiteit Amsterdam'. The study was completed with a final experimental research project that was done at the Solid State Physics department. The scope of this work was 'Hydrogen diffusion in YMg alloys' and was performed under the supervision of Prof. dr. R. Griessen. In 1999 he received his 'doctoraal' degree in experimental physics. In 2000 he worked as a Ph.D. student at the Academic Medical Center in Amsterdam on diffusion-tensor magnetic resonance imaging. In 2001 he started as a Ph.D. student at the FOM Institute for Atomic and Molecular Physics (AMOLF) in the Photonic Materials group under supervision of Prof. Dr. A. Polman. The research performed in this group is the subject of this thesis.

This thesis is based on the following publications

- *Surface plasmon polariton modified emission of erbium in a metallodielectric grating*, J. Kalkman, C. Strohhöfer, B. Gralak, and A. Polman, Appl. Phys. Lett. **80**, 30 (2003). (Chapter 2)

- *Coupling of Er ions to surface plasmons on Ag*, J. Kalkman, L. Kuipers, A. Polman, and H. Gersen, Appl. Phys. Lett. **86**, 041113 (2005). (Chapter 3)

- *Excitation of surface plasmons at a SiO_2/Ag interface by silicon nanocrystals*, J. Kalkman, L. Kuipers, A. Polman, and H. Gersen, submitted to Phys. Rev. B. (Chapter 4)

- *Erbium-implanted silica microsphere laser*, J. Kalkman, A. Polman, T. J. Kippenberg, K. J. Vahala, and M. L. Brongersma, Nucl. Instr. Meth. B. in press (2005). (Chapter 6)

- *Ultra-low-threshold erbium-implanted toroidal microlaser on silicon*, A. Polman, B. Min, J. Kalkman, T. J. Kippenberg, and K. J. Vahala, Appl. Phys. Lett. **84**, 1037 (2004). (Chapter 7)

- *Erbium-implanted high-Q silica toroidal microcavity laser on a Si chip*, B. Min, T. J. Kippenberg, L. Yang, K. J. Vahala, J. Kalkman, and A. Polman, Phys. Rev. A **70**, 033803 (2004). (Chapter 7)

- *Fabrication and characterization of erbium-doped toroidal microcavity lasers*, J. Kalkman, A. L. Tchebotareva, T. J. Kippenberg, B. Min, K. J. Vahala, and A. Polman, submitted to J. Appl. Phys. (Chapter 7)

- *Selective excitation of erbium in silicon-infiltrated silica colloidal photonic crystals*, J. Kalkman, E. de Bres, A. Polman, Y. Jun, D. J. Norris, D. C. 't Hart, J. P. Hoogenboom, and A. van Blaaderen, J. Appl. Phys. **95**, 2297 (2004). (Chapter 8)

Other publications, not related to this thesis

- *Purcell factor suppressed scattering losses in optical microcavities*, T. J. Kippenberg, A. L. Tchebotareva, J. Kalkman, A. Polman, and K. J. Vahala, submitted to Phys. Rev. Lett.

- *Hidden transition in the "unfreezable water" region of the PVP-water system*, M. J. A. de Dood, J. Kalkman, C. Strohhöfer, J. Michielsen, and J. van der Elsken, J. Phys. Chem. B **107**, 5906 (2003)

- *Insulating fcc YH_3 stabilized by MgH_2*, S. J. van der Molen, D. G. Nagengast, A. T. M. van Gogh, J. Kalkman, E. S. Kooij, J. H. Rector, and R. Griessen, Phys. Rev. B **63**, 235116 (2001)

Summary

From the laser in the CD player, to the incandescent light bulb, many of today's applications of light depend on the precise control of the spontaneous emission of light by optical emitters. By using advanced lithographic tools we can control the microstructure around an optical emitter with a length scale on the order of the wavelength of light. In this way the photonic density of states (DOS) at the emission frequency of the emitter can be modified. By increasing the DOS, the spontaneous emission rate can be enhanced, thus enabling larger modulation rates, important for various photonic device applications. By decreasing the DOS, the spontaneous emission rate can be reduced, thus enabling more efficient stimulated emission or increasing the probability of upconversion, features that could be important for applications in efficient lasers and solar cells, respectively.

Alternatively, the spontaneous emission can be modified by creating additional non-radiative decay mechanisms. An optical emitter in the proximity of a metal can excite a surface plasmon (SP). A SP is a bound electromagnetic wave that propagates at a metallo-dielectric interface. By creating a grating on the interface on which SPs can scatter, they can be coupled out and contribute to the far-field emission of the optical emitter, instead of being lost to Joule heating. In this way large changes in the spontaneous emission can be achieved.

In this thesis we focus on the control of spontaneous emission in three different microstructured photonic materials doped with Er ions. Erbium is a rare-earth metal that, when incorporated in a solid, takes on a trivalent charge state and can emit light at a wavelength of 1.5 μm. It plays a key role in current day telecommunication technology as the principle ingredient of optical fiber amplifiers. The control over the spontaneous emission of Er is therefore of great importance, both from a fundamental point of view, and for its use in new photonic applications based on the 1.5 μm telecommunications wavelength.

Part I of this thesis focusses on the effect of a metallo-dielectric interface on the spontaneous emission of optical emitters in silica glass. In Chapter 2 we show that Er ions can couple to SPs via a near-field interaction. By coupling SPs out into the far field, large changes in the Er photoluminescence emission distribution, spectra, and polarization can be observed. In Chapter 3 we probe the coupling of Er ions to SPs by measuring the effect on the Er decay rate. By

accounting for non-radiative decay due to concentration quenching, the decay rate for Er in SiO_2 is determined both for a sample in air and for a sample covered with Ag. The proximity of the Ag layer increases the Er decay rate by 70 %. This result is in good agreement with calculations based on a classical dipole oscillator model. Chapter 4 describes the coupling of luminescent Si nanocrystals to SPs. We derive a decay rate distribution from the stretched-exponential photoluminescence decay of Si nanocrystals. For Si nanocrystals placed at ∼50 nm from the SiO_2/Ag interface, the average decay rate is enhanced by a factor 1.8. The enhancement is in agreement with calculations with the classical dipole oscillator model and mainly due to the excitation of SPs. From the observed change in decay rate the internal emission quantum efficiency of Si nanocrystals is derived: 77 %. We calculate that by using a thin Ag film instead of a semi-infinite Ag layer the SP excitation rate can be further increased. This allows for larger increases in radiative decay rate and/or quantum efficiency of Si-nanocrystal-based devices. In the final chapter of this part the SP dispersion characteristics and propagation losses are calculated for SPs on Ag with different dielectrics. Several concepts for SP-based photonic devices are presented that make use of the special SP dispersion, propagation and material characteristics.

In Part II we focus on the effect of a microcavity on the spontaneous emission of Er and describe how ion implantation can be used to dope dielectric microresonators with optically active Er ions. Chapter 6 shows the fabrication and characterization of an Er ion-implanted silica microsphere resonator. After ion implantation and thermal annealing, a cavity quality factor (Q) as high as $1.9{\cdot}10^7$ is obtained at a wavelength of 1450 nm . Er lasing is observed around 1570 nm under optical pumping, with a threshold as low as 150 μW for an optimized Er distribution. In Chapter 7 we describe the doping with Er of toroidal microcavities on a Si chip, either by pre-implanting the SiO_2 base material, or by post-implantation in a fully fabricated microtoroid. The optical activation of Er ions through the microtoroid is investigated with three-dimensional confocal photoluminescence spectroscopy and microprobe Rutherford backscattering spectrometry. Based on these findings, the overlap between the Er distribution and optical mode is calculated and the Er absorption-related cavity Q is determined. Both cavities have Q values close to the Er absorption-related values. When excited in the proper geometry, periodically spaced enhancements of the Er photoluminescence are observed superimposed on the Er spontaneous emission spectrum. This is attributed to coupling of Er to cavity modes. Erbium lasing at 1.5 μm is observed with the lowest threshold (4.5 μW) for the pre-implanted microtoroids.

In Part III we describe the fabrication of an Er-doped Si-inverse opal photonic crystal. These photonic crystals can potentially have a photonic bandgap that can fully inhibit the spontaneous emission of on optical emitter. We derive fabrication criteria for such a photonic crystal, based on the lattice parameter, filling fraction, and Si refractive index. In the opal photonic crystal composed of both Si and SiO_2 we show that Er ions can be selectively excited in both the Si and SiO_2 part of the photonic crystal by changing the excitation wavelength

and/or the measurement temperature. This can be used to probe the local DOS in both constituents of these photonic crystals. We observe Er lifetimes of 0.9 ms in the Si part and 7 ms in the SiO_2 part of the photonic crystal, reflecting the different emission probabilities due to variations in the local atomic environment of the luminescing Er ion.

Samenvatting

Van de laser in de CD speler tot de gloeilamp, veel van de toepassingen van licht zijn mogelijk gemaakt door de controle over de spontane emissie van lichtuitstralers. Door gebruik te maken van geavanceerde lithografische technieken kunnen we de microstructuur rondom een lichtuitstraler controleren op een lengteschaal gelijk aan die van de golflengte van het uitgezonden licht. Op deze manier kunnen we de fotonische toestandsdichtheid bij de emissiefrequentie van de lichtuitstraler modificeren. Als we de toestandsdichtheid laten toenemen, dan kan de vervalsnelheid van de lichtbron toenemen. Dientengevolge neemt de maximale modulatie frequentie van de lichtbron toe, wat belangrijk kan zijn voor toepassingen in optische apparatuur. Bij een afname van de toestandsdichtheid kan de vervalsnelheid van de lichtbron afnemen. Als gevolg hiervan kunnen gestimuleerde emissie en coöperatieve opconversie makkelijker optreden. Dit zou belangrijk kunnen zijn voor toepassingen in efficiënte lasers en zonnecellen.

Een andere manier om de spontane emissie te veranderen is door het niet-stralende verval van de lichtuitstraler te veranderen. Dit kan door de lichtuitstraler dicht bij een metaal te plaatsen waarbij het oppervlakteplasmonen kan aanslaan. Een oppervlakteplasmon is een gebonden electromagnetische golf die zich op het grensvlak van een dielektricum en een metaal voortplant. Door een tralie op dit grensvlak te maken kunnen de oppervlakteplasmonen worden uitgekoppeld en bijdragen aan de verre-veld emissie van de lichtuitstraler in plaats van te worden geabsorbeerd door het metaal. Door efficiënt oppervlakteplasmonen aan te slaan kunnen grote veranderingen in de spontane emissie worden bewerkstelligd.

In dit proefschrift concentreren we ons op het modificeren van de spontane emissie in drie verschillende microgestructureerde fotonische materialen gedoteerd met erbium. Erbium is een zeldzaam-aard metaal dat een driewaardige ladingstoestand aanneemt als het wordt geïncorporeerd in een vaste stof. Het zendt licht uit met een golflengte van 1.5 μm en speelt daarmee een belangrijke rol in de hedendaagse glasvezeltechnologie als belangrijkste component van optische glasvezel lichtversterkers. Het controleren van de spontane emissie van Er is dan ook van groot belang, zowel vanuit fundamenteel oogpunt als uit het oogpunt van toepassing bij de 1.5 μm telecommunicatiegolflengte.

In deel I van dit proefschrift concentreren we ons op het effect van een metaal-dielektricum grensvlak in de nabijheid van lichtuitstralers in silica glas.

In hoofdstuk 2 laten we zien dat Er ionen naar oppervlakteplasmonen kunnen koppelen door een nabije-veld interactie. Door de oppervlakteplasmonen uit te koppelen naar het verre veld kunnen grote veranderingen in de emissieverdeling, -polarisatie en -spectra worden bewerkstelligd. In hoofdstuk 3 meten we de invloed van een metaal-dielektricum grensvlak op de vervalsnelheid van Er ionen. Door het niet-stralende verval ten gevolge van de interactie tussen Er ionen in rekening te nemen kunnen we de intrinsieke vervalsnelheid voor Er ionen nabij een glas/Ag en een glas/lucht grenslaag bepalen. De nabijheid van het Ag vergroot de vervalsnelheid met 70 %. Dit resultaat is in goede overeenkomst met berekeningen met een klassiek dipool oscillator model. Hoofdstuk 4 laat de koppeling van Si nanokristallen naar oppervlakteplasmonen zien. De fotoluminescentie vervalscurve is niet enkelvoudig exponentieel en wordt omgezet naar een vervalsnelheidverdeling. Op deze manier kan een gemiddelde vervalsnelheid worden bepaald. Voor Si nanokristallen op ongeveer 50 nm van het SiO_2/Ag grensvlak is de gemiddelde vervalsnelheid verhoogd met een factor 1.8 ten opzichte van de SiO_2/lucht grenslaag. Deze verhoging is in overeenstemming met berekeningen met het eerder genoemde klassieke dipooloscillator model en is voor het grootste deel het gevolg van de excitatie van oppervlakteplasmonen. Uit de gemeten verhoging van de vervalsnelheid kan het interne quantumrendement van Si nanokristallen worden bepaald: 77 %. Door in plaats van een half-oneindige Ag film een dunne Ag film te gebruiken kan de snelheid waarmee oppervlakteplasmonen worden aangeslagen verder worden vergroot. Dit vergroot de mogelijkheden om de stralende vervalsnelheid en het quantum rendement te kunnen verhogen in op Si nanokristallen gebaseerde optische apparatuur. In het laatste hoofdstuk van dit deel worden de dispersie eigenschappen en propagatie verliezen voor oppervlakteplasmonen op Ag met verschillende dielektrica uitgerekend. Een aantal concepten van op oppervlakte-plasmonen gebaseerde toepassingen wordt gepresenteerd. Deze maken gebruik van de unieke dispersie-, propagatie- en materiaal- eigenschappen van oppervlakteplasmonen.

In deel II focusseren we op de effecten van microresonatoren op de emissie van Er en beschrijven we hoe ionenimplantatie gebruikt kan worden om dielektrische microresonatoren te doteren met optisch actieve Er ionen. In hoofdstuk 6 laten we de fabricage en karakterisatie van een met Er ionen-geïmplanteerde sferische microresonator zien. Na ionenimplantatie en temperen vinden we een kwaliteitsfactor van $1.9{\cdot}10^7$ bij een golflengte van 1450 nm. We meten Er laser werking bij 1.5 μm onder optisch pompen, met een drempelpompvermogen van 150 μW voor de meest optimale Er verdeling. In hoofdstuk 7 beschrijven we de dotering met Er van toroïdale microresonatoren op een Si chip door óf post-implantatie in een volledig gefabriceerde microtoroïde, óf door het preimplanteren van het SiO_2 startmateriaal. De optische activering van Er ionen in de microtoroïde is onderzocht met drie-dimensionale fotoluminescentie spectroscopie en microbundel-Rutherford terugstrooiings spectroscopie. Met de hierbij gevonden Er verdeling en berekende optische modes wordt de modeoverlap berekend. De daarmee berekende Er absorptie-gerelateerde kwaliteitsfactoren komen goed overeen met de gemeten kwaliteitsfactoren. Als de microtoroïde

in de juiste geometrie wordt geëxciteerd zijn er periodiek geplaatste toenames in het Er fotoluminescentie spectrum zichtbaar die het gevolg zijn van de gemodificeerde toestandsdichtheid in de microtoroïde. We meten Er laser werking bij 1.5 μm voor zowel de post- als de pre-geimplanteerde microresonator. Het laagste drempelvermogen dat we hebben gemeten was 4.5 μW voor pregeëplanteerde microtoroïden.

Deel III beschrijft de fabricage van een Er-gedoteerd Si geïnverteerd opaal fotonisch kristal. Deze fotonisch kristallen kunnen een volledige fotonische bandkloof hebben die de spontane emissie helemaal kan stopzetten. We leiden ontwerpcriteria af voor zo'n fotonisch kristal gebaseerd op de rooster parameter, vulfractie en Si brekingsindex. We laten zien dat in het fotonische kristal opgebouwd uit Si en SiO_2 de Er ionen selectief geëxciteerd kunnen worden in beide delen van het fotonisch kristal door de excitatie golflengte en/of de meettemperatuur te veranderen. Op deze manier kan de lokale toestandsdichtheid in beide bestandsdelen van zo'n fotonisch kristal worden bepaald. We meten Er levensduren van 0.9 ms in het Si deel en 7 ms in het SiO_2 deel van het fotonisch kristal. Dit verschil weerspiegelt de verschillende atomaire structuur om de Er ionen in deze materialen.

Dankwoord/Acknowledgments

Voor u ligt een boek met de resultaten van vier jaar promotieonderzoek. Dit werk is tot stand gekomen met de steun en hulp van een groot aantal mensen.

Een zeer belangrijke bijdrage is geleverd door de, zowel wetenschappelijk als sociaal, zeer goede sfeer binnen AMOLF en in het bijzonder de fotonische materialen groep. Ik dank iedereen die daaraan heeft bijgedragen.

Ik wil mijn promotor en begeleider Albert Polman bedanken. Jouw steun en enthousiasme hebben inspirerend gewerkt bij de totstandkoming van de resultaten beschreven in dit proefschrift. Daarnaast heeft je opbouwende kritiek bij het schrijven van de vele manuscripten geleid tot goed leesbare artikelen die daardoor ook nog eens snel werden geaccepteerd.

Verder wil ik de fotonische materialen groep bedanken voor hun steun. Ik heb met veel plezier deelgenomen aan de discussies tijdens de lunchpauzes, congressen, werkbesprekingen en de 'niet te missen' koffiepauzes. Dank aan Basjan Berkhout, Teun van Dillen, Michiel de Dood, Jan van der Elsken, Martien den Hertog, Hans Mertens, Joan Penninkhof, Sjoerd Roorda, Max Siem, Christof Strohhöfer, Anna Tchebotareva, Ewold Verhagen, Rene de Waele en Timon van Wijngaarden.

Onze technici, Jan ter Beek en Johan Derks, bedankt voor het onderhouden van de vele apparatuur in onze groep, het heeft allemaal optimaal gefunctioneerd. Zo hebben we in een laatste eindspurt nog zonder problemen een groot aantal implantaties kunnen doen op de 1 MV versneller voordat die met pensioen ging. De mensen van de nanofotonica groep wil ik bedanken voor hun interesse en hulp bij het doen van mijn onderzoek. Ook wil ik de mensen van de werkplaats, E&I en de tekenkamer bedanken voor hun bekwame en slagvaardige hulp vele praktische problemen waar ik tegenaan liep bij mijn onderzoek.

Mijn kamergenoten wil ik in het bijzonder bedanken voor hun steun. Hans, je kritische kijk in de vele discussies zorgden dat ik nog eens goed naar sommige data en uitwerkingen moest kijken. Dat heeft zeker bijgedragen tot de inhoud van dit boekje. Michiel, jouw steun was zeer belangrijk voor me. Je leerde me de fijne kneepjes van fotoluminescentie spectrometrie, RBS, nanofabricage en ionenimplantatie. Je grondige kennis van de natuurkunde en de bereidheid die kennis met iedereen te delen was een grote hulp. Jan, je brede ervaring en 'thermodynamische kijk' op de zaken brachten vaak nieuwe inzichten en zorgden ervoor dat ik mijn hypothesen grondig moest onderbouwen. Ik herinner

me ook onze bezoeken, samen met Michiel en later Hans, aan Grenoble. Veel gezelligheid en tot diep in de nacht meten aan poly(vinylpyrrolidone) water oplossingen. Ewold, je enthousiasme en doortastendheid zullen je helpen om het afbeelden van oppervlakte plasmonen met erbium tot een succes te maken. Ik ben er van overtuigd dat het je gaat lukken.

In hoofdstuk 8 staan de resultaten van een goed verlopende samenwerking met twee groepen. Ik heb veel steun gehad aan discussies met mensen uit de Soft Condensed Matter groep, Universiteit Utrecht/AMOLF. Mijn dank gaat uit naar Alfons van Blaaderen, Erik de Bres, Dannis 't Hart en Jacob Hoogenboom. Also I would like to thank the people from the Chemical Engineering & Materials Science department of the University of Minnesota for their help and support. Many thanks to Yoonho Jun, David Norris and Hong Wei.

Mark Brongersma bedankt, jouw idee om sferische microresonatoren te implanteren heeft uiteindelijk geresulteerd in een belangrijk deel van dit proefschrift. Tobias Kippenberg, je steun aan het microresonator project was van doorslaggevend belang. Na de uitvoering van de implantatie in sferische microresonatoren stelde je voor om ionenimplantatie te gebruiken voor jullie net ontwikkelde microtoroïden. Een uitstekende zet, waarbij onze beiden expertises optimaal konden worden benut. Je grote ervaring met microresonatoren heeft tot zeer goede resultaten geleid. I would like to thank Bumki Min for his fine theoretical and experimental work on the erbium-doped microtoroids. Many thanks to Kerry Vahala for his support on the erbium-doped microresonator projects and for the hospitality during my stay in your group.

Henk Jan Gersen, je spontane aanbieding om je programma te gebruiken voor berekeningen aan dipolen boven grensvlakken was een schot in de roos. De berekeningen sloten precies aan bij de experimenten die ik deed en ik wil je dan ook hartelijk bedanken voor het beschikbaar stellen van je programma.

Dank aan Leo IJzendoorn en Peter Mutsaers van de TUe voor hun hulp bij de μRBS metingen beschreven in hoofdstuk 7. Ook wil ik alle mensen bij DIMES bedanken voor hun hulp bij de fabricage van de structuren beschreven in dit proefschrift.

Als laatste wil ik familie, kennissen en vrienden bedanken voor de interesse die ze getoond hebben in mijn werk. Jullie medeleven was een belangrijke steun bij het tot stand komen van dit proefschrift.

Jeroen Kalkman Amsterdam, februari 2005